WARSAW UNIVERSITY OF TECHNOLOGY

DISCIPLINE OF SCIENCE ENVIRONMENTAL ENGINEERING, MINING AND POWER ENGINEERING / FIELD OF SCIENCE ENGINEERING AND TECHNOLOGY

# Ph.D. Thesis

Stanisław Siatkowski, M.Sc.

**Predicting the Detonation Cell Size of Biogas – Oxygen Mixtures**

Supervisor

Jan Kindracki, D.Sc.

WARSAW 2023

# Acknowledgments

At the beginning of this dissertation I would like to express my sincere gratitude to my supervisor, Prof. Jan Kindracki for all the guidance and help provided to me during my Ph.D. study. His support and mentoring helped me to achieve the academic goals that I have set for myself and overcome all the obstacles that showed up along the way.

My sincere thanks go also to my beloved wife for her support, patience and indulgence through all those years. Last but not least, I would like to thank my colleague Krzysztof Wacko for all the countless hours spent in the laboratory together while doing the experiments presented in this thesis.

# Streszczenie

Wielkość komórki detonacji jest jednym z podstawowych parametrów opisujących proces detonacji. Jest on bardzo ważny zarówno z teoretycznego, jak i praktycznego punktu widzenia. W zastosowaniach teoretycznych, ponieważ koreluje z innymi skalami długości, natomiast w praktycznych, ponieważ jest wykorzystywany w analizach bezpieczeństwa i procesie projektowania silników detonacyjnych. Z tego powodu, temat ten jest intensywnie badany od prawie 100 lat. Jednocześnie, ze względu na rosnącą świadomość zmian klimatycznych, ludzkość poszukuje nowych, alternatywnych źródeł energii. Jednym z rozwiązań jest biogaz, ponieważ charakteryzuje się on bardzo niskim bilansem emisji netto uwalnianych do atmosfery podczas spalania. Biogaz ma jednak swoje wady, z których największą jest niska wartość opałowa. Problem ten można jednak przezwyciężyć stosując spalanie detonacyjne.

Prezentowana praca koncentruje się na stworzeniu modelu uczenia maszynowego, pozwalającego przewidywać rozmiar komórki detonacyjnej biogaz-tlen z zadowalającą dokładnością. W tym celu, w pierwszej kolejności przeprowadzono szeroko zakrojoną kampanię eksperymentalną, podczas której zebrano ponad 35 000 pomiarów wielkości komórek. Podczas eksperymentów zmieniano trzy parametry: ciśnienie początkowe mieszaniny $p_0$, współczynnik ekwiwalencji $\phi$ i skład biogazu wyrażony jako procent metanu. Łącznie przetestowano ponad 200 unikalnych kombinacji tych parametrów. W pracy przedstawiono zależności między wielkością komórek a każdym z trzech parametrów: p0, $\phi$ i %CH4, które były następujące: logarytmiczne, kwadratowe i liniowe. Dodatkowo zbadano i przedstawiono zależność między długością strefy indukcji ZND i parametrem stabilności $\chi$ a tymi parametrami. Część eksperymentalną zakończono przedstawiają dokładną analizę rozkładu wielkości komórek detonacyjnych.

W drugiej części pracy dane zebrane z eksperymentów zostały wykorzystane do trenowania i testowania trzech różnych typów modeli uczenia maszynowego. Testowane modele były następujące: regresja liniowa, regresja wektorów nośnych i sieć neuronowa. Dodatkowo, modele były trenowane i testowane przy użyciu dwóch typów danych: surowych danych oraz danych zagregowanych. Agregacja danych polegała na obliczeniu średniej wielkości komórki detonacji dla każdej unikalnej kombinacji $p_0$, $\phi$ i $\%CH_4$ przed treningiem modelu. Parametrami używanymi do trenowania modelu były te same trzy, które były zmieniane w eksperymentach. Wyboru tego dokonano w celu uniknięcia uzależnienia modelu

od dodatkowych założeń. Te mogłyby zostać wprowadzone w wyniku użycia innych parametrów pochodzących na przykład z wybranego mechanizmu kinetyki reakcji czego chciano uniknąć. Finalnie, okazało się, że wszystkie trzy typy modeli dały bardzo podobne wyniki bez znaczących różnic. Wszystkie z były bardzo dobre o wysokiej dokładności i niskim błędzie. Spośród trzech typów modeli, SVR dał najlepsze wyniki, ale jak wspomniano, różnice te nie były duże.

Podsumowując, w toku pracy udowodniono, że możliwe jest stworzenie modelu uczenia maszynowego zdolnego do przewidywania wielkości komórki detonacyjnej mieszanin biogazowo-tlenowych z zadowalającą dokładnością. Stanowi to kolejny krok w kierunku utworzenia ogólnego modelu przewidywania wielkości komórki detonacji będącego w stanie przewidzieć ją dla szerokiego zakresu różnego rodzaju paliw, utleniaczy i gazów rozcieńczających. Taki model, gdy już powstanie będzie stanowił ogromną pomoc dla społeczeństwa naukowców zajmujących się zagadnieniem spalania detonacyjnego.

**Słowa kluczowe:** detonacja, komórka detonacji, uczenie maszynowe, biogaz

# Abstract

The detonation cell size is one of the basic parameters describing the detonation process. It is very important both from the theoretical and practical point of view. In theoretical applications because it correlates with other length scales while in practical, because it is used in safety analyses and design process of detonation engines. This is why this topic has been extensively researched for almost 100 years now. At the same time, due to the growing awareness of the climate change, the humanity looks for new, alternative sources of energy. One such solution is a biogas due to the fact that has a very low net balance of emissions when burned. However, biogas has its own drawbacks out of which the biggest one is the low Lower Heating Value. This problem can be overcome by utilizing a detonative combustion.

The presented work focuses on creating a machine learning model that allows for predicting a biogas-oxygen detonation cell size with satisfying accuracy. In order to achieve that, first an extensive experimental campaign was conducted during which over 35 000 cell size measurements were collected. During the experiments three parameters were varied: mixture initial pressure $p_0$, equivalence ratio $\phi$ and biogas composition expressed as methane percentage. This resulted in over 200 unique combinations of those parameters that were tested. In the thesis, the relationships between the cell size and each of the three parameters: $p_0$, $\phi$ and $\%CH_4$, were presented and were as follows: logarithmic, quadratic and linear. Additionally, the relationship between ZND induction length and stability parameter $\chi$ and the three parameters was also studied and presented. Finally, at the end of the first part, the analysis of the detonation cell size distribution was also provided.

In the second part of the work, the data gathered from the experiments was used to train and test three different types machine learning models. The tested models were as follows: linear regression, support vector regression and neural network. Additionally, the models were trained and tested using either raw data or aggregated data, using average cell size. The parameters used to trained the model were the same three that were varied in the experiments and their derivatives. This choice was done in order to avoid the model being dependent on some kind of additional assumptions. Those could be introduced by using other parameters coming for example from a chosen reaction kinetics mechanism. It turned out that all three types of models gave very similar results without significant differences. All of them proved to give very good results with high accuracy and low error. Out of the three types of models, the SVR gave the best results but, as mentioned, the differences were not big.

To sum up, the work has demonstrated that it is possible to create a machine learning model capable of predicting the detonation cell size of biogas-oxygen mixtures with satisfying accuracy. This represents another step towards the creation of a general detonation cell size prediction model capable of predicting detonation cell size for a wide range of different fuels, oxidizers and diluent gases. Such a model, once established, will be of great importance to the community of researchers working in the field of detonative combustion.

**Keywords:** detonation, detonation cell, machine learning, biogas

# Contest

# List of Figures

# List of Tables

# Nomenclature

$A_r$ – pre-exponential factor [-]

$E_a$ – activation energy [J]

h – enthalpy per unit mass (thermal plus chemical) [J]

n – temperature exponent in the Arrhenius law [-]

p – pressure [bar]

q – heat release per unit mass [J/kg]

R – specific gas constant [J/mol*K]

$R^2$ – coefficient of determination

s – sample's standard deviation

u – velocity [m/s]

V – velocity [m/s]

T – temperature [K]

**Greek letters:**

$\gamma$ – specific heat ratio [-]

$\Delta_i$ – induction length [mm]

$\Delta_R$ – reaction length [mm]

$\varepsilon_I$ – activation energy for the induction process

$\lambda$ – detonation cell size [mm]

$\rho$ – density [$kg/m^3$]

$\sigma$ – distribution's standard deviation

$\dot{\sigma}$ – thermicity [1/s]

$\phi$ – equivalence ratio [-]

$\chi$ – detonation structure stability parameter [-]

**Subscripts:**

0 – initial conditions

1 – conditions of the unburned mixture

2 – conditions of the burned  mixture

ps – post shock

vn – von Neumann state

**Abbreviations:**

ANN – Artificial Neural Network

CJ – Chapman – Jouguet

CNN – Convolutional Neural Network

CV – Coefficient of Variation

DDT – Deflagration-to-Detonation Transition

Eq - equation

GHG – Greenhouse Gases

IQR – Interquartile Range

LHV – Lower Heating Value

LMDE – Linearized Model Detonation Engine

LR – Linear Regression

MAE – Mean Absolute Error

MAPE – Mean Absolute Percentage Error

ML – Machine Learning

MLP – Multi-Layer Perceptron

MSE – Mean Squared Error

NN – Neural Network

PDE – Pulsed Detonation Engine

PLIF – Planar Laser Induced Fluorescence

POD – Proper Orthogonal Decomposition

RDE – Rotating Detonation Engine

ResNet – Residual Network

R-H – Rankine – Hugoniot

RSS – Residual Sum of Squares

SGD – Stochastic Gradient Descent

SEM – Standard Error of the Mean

SVM – Support Vector Machine

SVR – Support Vector Regression

TSS – Total Sum of Squares

T/W – Thrust to Weight ratio

UN FCCC - United Nations Framework Convention on Climate Change

YOLO – You Only Look Once (name of an object detection algorithm)

ZND – Zel'dovich – von Neumann - Döring

# 1. Introduction

## 1.1. Motivation

As human-induced climate change progresses humanity tries to stop it by reducing the greenhouse gases (GHG) emissions [1]. In order to do that countries across the globe struggle to fulfill the goal of achieving carbon neutrality by 2050 set up by the United Nations Framework Convention on Climate Change (UN FCCC) [2]. For many years now a lot of research efforts in the field of alternative and renewable fuels and energy production that does not impact the environment, can be observed. It is additionally strongly driven by governments and international climate policies. Example of those are the Kyoto Protocol (1997) [3], the Paris Agreement (2015) [4] and the following Katowice Climate Package (2018) [5]. At the same time, it cannot be overlooked that energy is crucial for functioning and growth of humanity. It is well known fact that living standards are high in countries with high industrial output and intense energy use. Most of this energy is obtained from fossil fuels like coal, oil and natural gas [6], and those are no longer perceived as viable, long-term sources due to the aforementioned climate change. It is therefore evident that if governments want to be able to fulfill international agreements, reduce the global emissions of greenhouse gas and achieve the carbon neutrality in 2050 a new alternative and renewable energy source must be secured.

In order to do that, countries throughout the world invests more and more money into renewable power and fuels. Annual investments in those grew from 296 billion USD in 2018, through 301.7 billion USD in 2019 [7] up to 366 billion USD in 2020. The global share of modern renewable energy is also growing annually and went from 8.7% in 2009 up to 12.6% in 2020. However, if one looked at the power generation those numbers are even higher, in 2011 the share of renewable electricity was 20.4% globally while in 2021 it was 28.3%. This means that the renewable share of electricity generation increased by almost 8 percentage points in the past decade. What is more, the renewable energy sources share in net annual addition in power generating capacity is also continuously growing and reached 84% in 2021 [8]. All this goes to show, that there is an ever growing effort across the globe to move away from fossil to renewable fuels. In order to achieve that and to make existing processes even more efficient a lot of research effort is still required.

### 1.1.1. Biogas

There is a number of alternative, renewable energy sources actively being researched and harnessed across the globe. The most heavily sources used in electricity generation are

hydropower, solar and wind [8]. Additionally, an intensive research work is done on introducing hydrogen as an alternative fuel to replace hydrocarbons [9] and still in distant future – nuclear fusion [10]. However, it is important to note, that electricity generation accounted only for 17% of energy demand in 2021 [8]. If one was to look at the overall world's demand for energy, then it turns out that the most renewable energy was generated as a renewable heat from biomass, geothermal and solar sources [8]. This means, that biomass as an energy source accounts for a significant portion of energy generation, and among different types of biomass used, there is also a biogas. It is seen as a good, renewable fuel and its use and research is widely supported by various international organizations, such as:

- European Commission in form of grants in programs like HORIZON 2020 [11];
- European Technology and Innovation Platform [12];
- European Biogas Association [13];
- International Energy Agency [14];
- American Biogas Council [15];

and many more. What is more, also researchers across the globe study the feasibility and possibilities for using biogas as an energy source in their countries, examples include, but are not limited to: Bangladesh [16], Indonesia [17], Turkey [18, 19], Italy [20], Malaysia [21], Australia [22] and Poland [23]. It is also worth to notice, that in 2018 Mao et al. [24] published an extensive literature study on the biomass energy and environment relevant articles from 1998 to 2017. They showed that over past 20 years the research in those topics has been becoming increasingly more extensive.

Biogas is mixture consisting mainly of methane ($CH_4$) and carbon dioxide ($CO_2$), additionally it may contain small quantities of other gases and contaminants such as water, hydrogen sulfide ($H_2S$), nitrogen ($N_2$), ammonia ($NH_3$), oxygen ($O_2$), siloxanes and solid matter [25]. It is the product of anaerobic digestion of the organic matter by the bacteria in an oxygen-free environment. The exact composition of the biogas depends on the type of the feedstock and the production pathway [26]. The feedstock used in biogas production might be different kinds of organic matter, such as: food, plant debris, animal manure, sewage sludge, biodegradable portions of municipal solid waste, etc. [27]. Typical volume percentages in biogas range from, 40% up to 85% for $CH_4$ and 20% to 65% for $CO_2$ [13, 15, 25–28], those value ranges differ between the literature sources and the values provided here presents the widest ranges from the literature.

Biogas has a number of advantages that make it such an attractive alternative, renewable energy source. The benefits of biogas are as follows:

- reducing the GHG emissions produced in the combustion process [13, 26];
- moving manure from open lagoons to an airtight biogas system reduces GHG emissions due to a biomass decomposition as well as spread of pathogens and burdensome odor[15];
- recycling manure creates an opportunity to separate nutrients and keep them out of waterways [15];
- the use of digestate (the residue that is left after processing the biomass) can replace costly synthetic fertilizers [13, 15]
- biogas is easy to store and transport and as an energy source it is more stable than weather dependent – solar and wind [20];

Although the advantages of a biogas are evident it has also some drawbacks. One is the aforementioned impurities in the biogas that might have a negative impacts on the utilization system, such as corrosion or even pose a health hazard [28]. However, this is usually mitigated during the biogas production process when the impurities are chemically removed. The most important issue with biogas is its low Lower Heating Value (LHV) that ranges from 16 MJ/$m^3$ to 28 MJ/$m^3$ [20, 26, 28]. It is approximately 40-60% less than the natural gas LHV (33.5 – 39 MJ/$m^3$ [20, 28]) and the pure methane (35.8 MJ/$m^3$ [20]). Low LHV results in some additional problems when a gas turbine is fueled by biogas. In order to maintain efficiency at an acceptable level a higher fuel flow is required [29]. This in turn leads to a decreased surge margin of the compressor and overheating of the turbine blades, shortening their useful life. Those problems however, can be mitigated by switching from a deflagrative to detonative combustion mode.

### 1.1.2. Detonation

There are two combustion modes in which a flame front exists – deflagration and detonation. In the deflagration the combustion front and the pressure wave are propagating separately with the pressure wave preceding the reaction zone. The combustion wave propagates at a subsonic speed relative to the unburnt mixture. The pressure and density behind the flame front drops. In case of the detonation the combustion front is attached to the shock wave and propagates at a supersonic speed relative to the unburnt mixture (equal to the local sound speed in the burnt mixture). In the contrary to the deflagration, the pressure and density of the burnt mixture after the flame front increase. In the following subsections the two most

popular detonation models will be discussed together with the cellular structure of the detonation.

### *1.1.2.1. Chapamn – Jouguet Detonation Model*

At the turn of the 19th and 20th centuries, Chapman (1899) [30] and Jouguet (1905) [31] published, independently of each other, the one-dimensional theory of a gaseous detonation. In it, the detonation wave is infinitely thin and propagates with a constant velocity, that is now called a *Chapman – Jouguet detonation velocity* – $V_{CJ}$. They treat it as a flow discontinuity in which a sudden, instantaneous change of the flow parameters occurs. This means that the combustion process is assumed to be infinitely fast. Figure 1 shows a schematic diagram of a one-dimensional detonation wave moving in the combustible mixture in a tube. The reference frame is following the wave motion which allows to treat the combustion wave as stationary and unburned mixture as moving towards it with a velocity $u_1$ and the burned mixture as moving away with a velocity $u_2$. The typical differences between a detonation and deflagration are presented in the Table 1.

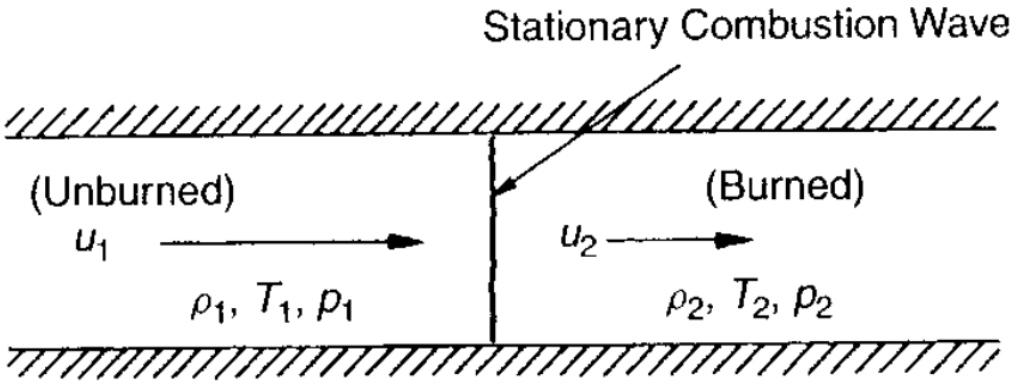


**Figure 1** Schematic diagram of a one-dimensional, stationary combustion wave. The reference frame is fixed to the wave. [32].

**Table 1** Typical differences in parameters between a detonative and deflagrative combustion in gases [32].

| | **Detonation** | **Deflagration** |
|---|---|---|
| $u_1/c_1$ | 5 – 10 | 0.0001 – 0.03 |
| $u_2/u_1$ | 0.4 – 0.7 (deceleration) | 4 – 6 (acceleration) |
| $p_2/p_1$ | 13 – 55 (compression) | ≈ 0.98 (slight expansion) |
| $T_2/T_1$ | 8 – 21 (heat addition) | 4 – 16 (heat addition) |
| $\rho_2/\rho_1$ | 1.7 – 2.6 | 0.06 – 0.25 |

If a one-dimensional flow with combustion (as in Figure 1) is considered, three conservation rules for the areas upstream and downstream from the combustion wave apply. Those are the conservation of mass (equation 1), momentum (eq. 2) and energy (eq. 3). The indexes 1 and 2 relate to the state of unburned and burned mixture, respectively.

$$\dot{m} = \rho_1 u_1 = \rho_2 u_2 \tag{1}$$

$$p_1 + \rho_1 u_1^2 = p_2 + \rho_2 u_2^2 \tag{2}$$

$$h_1 + \frac{1}{2}u_1^2 = h_2 + \frac{1}{2}u_2^2 \tag{3}$$

The enthalpies $h_1$ and $h_2$ are defined using the following relation:

$$h = \frac{\gamma}{y-1}\frac{p}{\rho} \tag{4}$$

Assuming that the ideal-gas law is applicable we can additionally introduce the equation of state of the burned mixture:

$$p_2 = \rho_2 R_2 T_2 \tag{5}$$

Taking the state of the unburned mixture as known ($p_1$, $\rho_1$ and $h_1$) there are therefore four equations (1, 2, 3 and 5) relating the five unknowns: $u_1$, $u_2$, $p_2$, $T_2$ and $\rho_2$. Through algebraic manipulations and substitutions, those equations can be reduced to a single one with only two unknows: $p_2$ and $\rho_2$. It is known as Rankine – Hugoniot relation (sometimes called in literature Hugoniot relation, e.g. in [32]) and is defined as follows:

$$\frac{\gamma}{\gamma-1}\left(\frac{p_2}{\rho_2} - \frac{p_1}{\rho_1}\right) - \frac{1}{2}(p_2 - p_1)\left(\frac{1}{\rho_1} + \frac{1}{\rho_2}\right) = q \tag{6}$$

Additionally by combining the equations (1) and (2) the Rayleigh – line relation (eq. 8) can be constructed:

$$p_2 - p_1 = \rho_1 u_1^2 - \rho_2 u_2^2 = \frac{(\rho_1 u_1^2)}{\rho_1} - \frac{(\rho_2 u_2^2)}{\rho_2} = \left(\frac{1}{\rho_1} - \frac{1}{\rho_2}\right)\dot{m}^2 \tag{7}$$

$$\rho_1^2 u_1^2 = \rho_2^2 u_2^2 = \frac{p_2 - p_1}{\frac{1}{\rho_1} - \frac{1}{\rho_2}} = \dot{m}^2 \tag{8}$$

From this relation it is clear that the density and pressure behind the combustion zone can either increase or decrease.

The Rankine – Hugoniot relation is usually presented in the form of a plot showing all the possible values of ($1/\rho_2$, $p_2$) for a given values of ($1/\rho_2$, $p_1$) and q, an example of the Ranking

– Hugoniot curve is shown in the Figure 2. The point marked by the conditions of the unburned mixture ($1/\rho_2$, $p_1$) is called 'the origin of the Rankine – Hugoniot plot' and is marked by the symbol A in the Figure 2. The regions of possible solutions are arrived at by, starting from point A, drawing vertical ($1/\rho_2$ = const.) and horizontal lines ($p_1$ = const.) to the point of intersection with the R-H curve as well as lines tangent to it. The curve is then divided into five solution regions (I, II, III, IV and V) as shown in the Figure 2. The last region, namely V, does not make

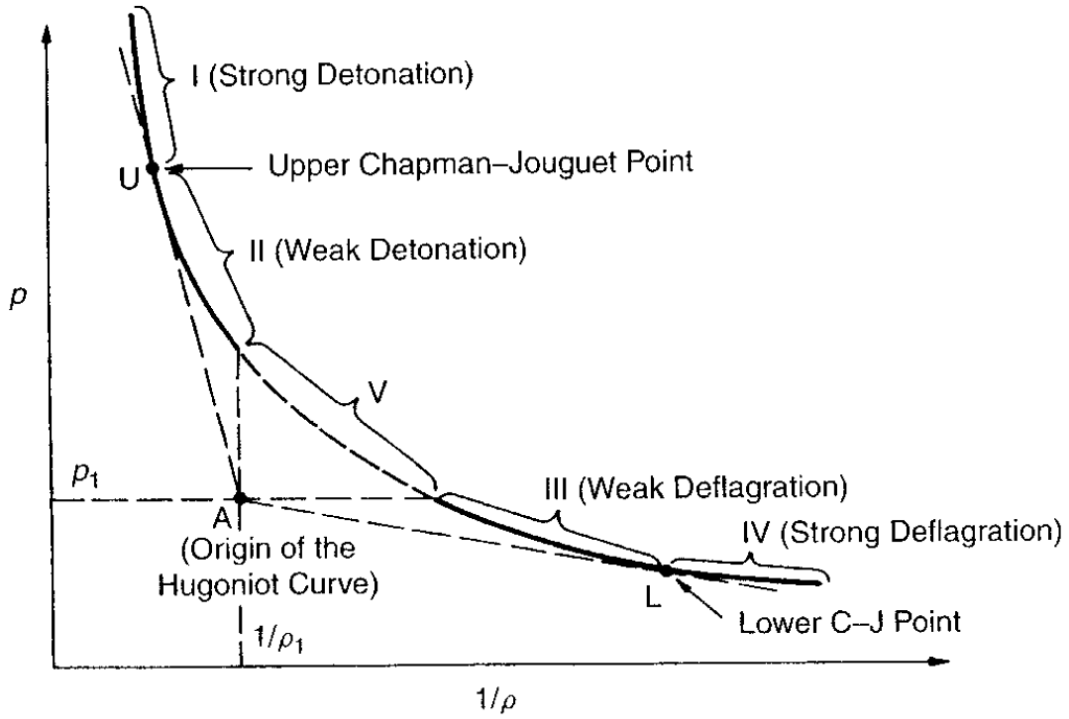


**Figure 2** Rankine - Hugoniot curve showing all the possible solution zones of different combustion conditions [32] .

any physical sense. In this region $p_2 > p_1$ and $1/\rho_2 > 1/\rho_1$ and from the Rayleigh-line relation it can be shown that $u_1$ would be imaginary, The points where the tangent lines touch the curve are called Upper and Lower Chapman – Jouguet points, for the detonation and deflagration solutions, respectively. The show the solutions with the minimum detonation velocity (point U) and maximum deflagration velocity (point L). Interesting fact is that the Chapman – Jouguet detonation velocity has a very high level of agreement with experiments. The regions I and II presents the solutions for strong and weak detonation, respectively, while regions III and IV for weak and strong deflagration, respectively.

### *1.1.2.2. Zel'dovich – von Neumann – Döring Detonation Model*

In years 1940 – 1942, independently of each other Zel'dovich (1940) [33], von Neumann (1942) [34] and Döring [35] proposed the extension of the classical Chapman – Jouguet theory described above. They assumed that the flow is strictly one-dimensional and steady relative to the detonation front. In the ZND theory the detonation is postulated to consist of a shock wave propagating at the detonation velocity and a chemical reaction zone following closely behind it but occupying a region much thicker that of a typical shock wave. The shock wave heats the mixture to a temperature at which the reactants start to react with high enough rate so that the deflagration following the shock wave propagates with the same velocity. Figure 3 presents the course of the mixture parameters (p, T, ρ) while passing through the detonation wave in a ZND model. The deflagration behind the leading shockwave (points 1 – 1' in the Figure 3) is divided into two regions: induction (1' – 1") and reaction zone (1" – 2). In the induction zone the rate of reaction increases slowly following the Arrhenius law, the temperature, pressure and density profiles are relatively flat in this zone. In the next zone, after the induction period, the parameters change rapidly due to the drastic increase of the reaction rate. The temperature rises significantly while the pressure and density decrease. Finally, after the reaction is completed the thermodynamic properties of the flow reach their equilibrium C-J values. Using the ZND model the thermodynamic parameters and the mixture composition along the width of the combustion zone (induction zone and reaction zone) can be determined.

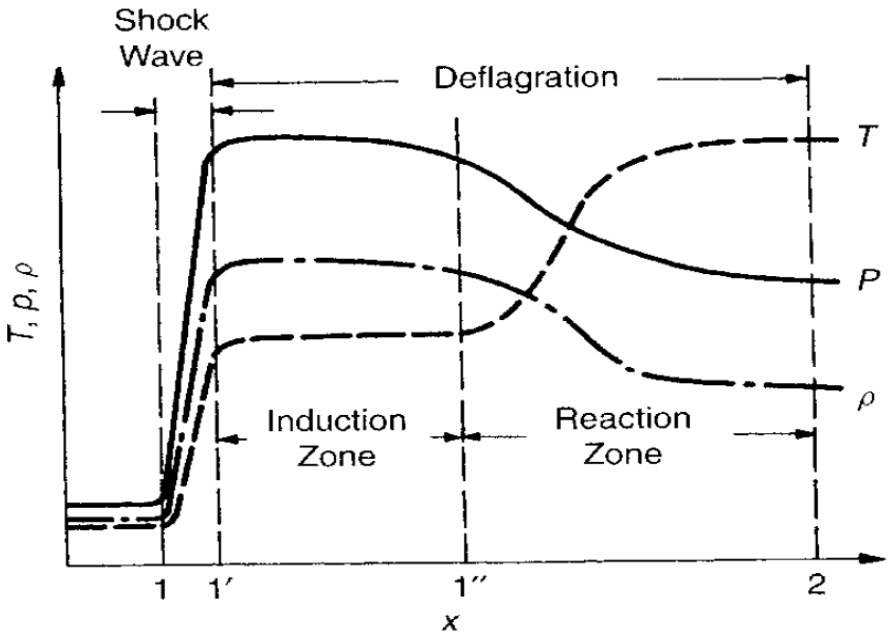


**Figure 3** Variation of the mixture parameters through the ZND detonation wave [32].

For this the conservation equations of mass, momentum and energy as well as the balance of combustion gas components must be used. Finally the equations are as follow:

$$\frac{D\rho}{Dt} = -\rho \frac{du}{dx} \tag{9}$$

$$\frac{Du}{Dt} = -\frac{1}{\rho}\frac{dp}{dx} \tag{10}$$

$$\frac{D\left(h + \frac{u^2}{2}\right)}{Dt} = \frac{1}{\rho}\frac{\partial p}{\partial t} \tag{11}$$

$$\frac{DY_i}{Dt} = \Omega_i \quad i = 1 \dots N \tag{12}$$

The symbol D means a substantial derivative and the equations are derived in the reference frame fixed to the detonation wave.

#### *1.1.2.3 The cellular structure of the detonation*

There are three main parameters used to describe the detonation process, those are: detonation propagation velocity, peak pressure and the detonation cell size – λ. The cells are a product of the three-dimensional, unstable structure of the detonation wave. They are formed by the intersection of the incident shock, Mach stem and transverse shock. The point where all three waves collide is called a 'triple-point' and its movement outlines the well-known diamond-shaped pattern called the detonation cellular structure [36]. Behind the leading shock waves the transverse waves and shear layers extend into the reaction zone. The transverse shocks propagates perpendicularly to detonation direction of propagation and collide with each other. This in turn causes the leading shock front to pulsate and alternate between strong Mach stems and weaker incident waves. Additionally, between the collisions of the those transverse shocks the velocity of the leading wave pulsates between 0.7 and 1.6 times the average detonation velocity. However, the overall average propagation velocity stays close to the $V_{CJ}$ for mixtures that are well withing the detonability limits [37]. The transverse waves play an important role in sustaining a detonation. It was shown by experimentally by Teodorczyk and Lee [38], and later by Radulescu and Lee [39] that the detonation might be reliably attenuated by attenuating the transverse waves.

The detonation cell size, also called width, is the distance between the points where two triple-pints crossed paths. The described cellular structure of the detonation and the detonation

cell size are presented in the Figure 4a while in the Figure 4b an example of the cellular structure recorded on the smoked foil during the experimental campaign is presented.

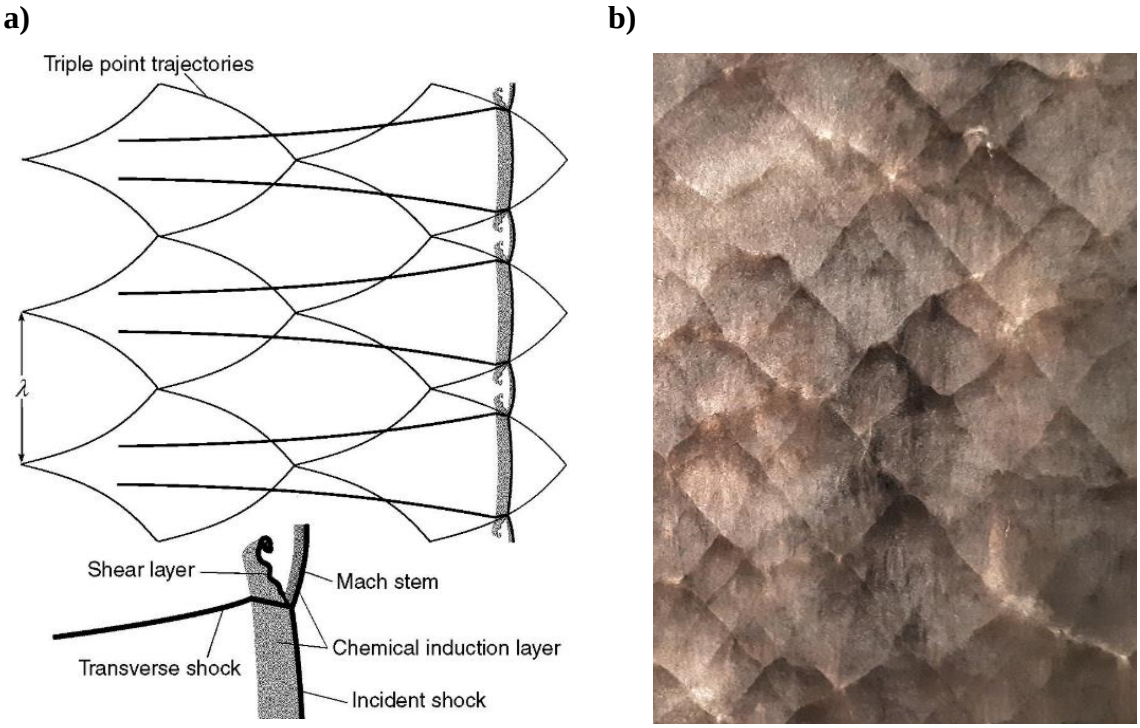


**Figure 4** a) The cellular structure of the detonation [37]. b) an example of the cellular structure of the detonation recorded during the experiments. The biogas was 50-50, $\phi$ = 0.5 [-] and $p_0$ = 1.2 [bar].

The detonation cell size is used both in theoretical, fundamental description of the dynamics of the detonation process [36] as well as in practical applications like safety analysis and designing combustion chambers utilizing detonative combustion mode [40, 41]. For the former it is because it correlates with other length scales [42, 43] that can be defined for the deflagration-to-detonation transition (DDT) [44], initiation [45] and detonation diffraction [46]. Those length scales as well as the cell size are in turn highly correlated with the ideal reaction zone length of the detonation wave [47]. As mentioned at the beginning of this paragraph the cell size is a very important parameter in practical applications as well. It is widely used in safety analysis in places where there is a probability of a gas leak that would form a combustible mixture with the air, such as power plants or chemical plants. In case of ignition a flame could propagate, accelerate and finally a DDT could occur leading to potential huge loss of property and human life. The cell size is used in such analysis because if in a given set of condition a cellar structure of the detonation cannot be sustained, the detonation cannot propagate marking the detonability limit of the mixture [40]. The other application of the detonation cell size is in the process of designing the combustion chamber of the Rotating Detonation Engine

(RDE) [41, 48, 49]. Xie et al. [50] showed that detonation wave tends to be stable when the λ is smaller than the width of the chamber. Bykovskii et al. [51–53] also studied the connection between flow conditions, λ, chamber geometry and the detonation wave's stability in the RDE.

### 1.1.3. Detonative propulsion

As mentioned in the previous subsection, detonation can be a very dangerous phenomenon if it appears spontaneously and in uncontrolled manner. On the other hand, detonative combustion has a number of advantages over the deflagration. The main one is that it has higher thermal efficiency compared to the isobaric or isochoric cycle [41, 49]. Table 1 presents the comparison of the calculated efficiency of different thermodynamic cycles for different fuels for an initial compression ratio in RDE equal to 5 [49]. It is evident that the thermodynamic cycle corresponding to the detonation process results in the highest thermal efficiency among all of the fuels shown. The detonative combustion can also occur in a wide variety of equivalence ratios, from lean [41] through stoichiometric [50] up to reach mixtures [48, 54]. Burning a lean mixture results in a lower flame temperature [55] which could solve the problem of turbine blades overheating when using biogas. What is more, but very important in the context of global warming, it was shown that, especially for lean mixtures, engines utilizing detonative combustion mode, will have significantly lower NOx emissions [56]. Due to this reasons, a lot of effort has been put into harnessing the power of the detonation in the propulsion systems. Many different kinds of engines using the detonative combustion has been proposed. However, as it is not the focus of this work, only the two most popular ones (Pulsed Detonation Engine – PDE and Rotating Detonation Engine – RDE) are described below. An interested reader is referred to the comprehensive overview of the detonative propulsion systems written by Wolański [41].

**Table 2** Comparison of calculated efficiency of different thermodynamic cycles for different fuels [49].

| **Fuel** | **Brayton (%)** | **Humphrey (%)** | **Fickett-Jacobs (%)** |
|---|---|---|---|
| Hydrogen ($H_2$) | 36.9 | 54.3 | 59.3 |
| Methane ($CH_4$) | 31.4 | 50.5 | 53.2 |
| Acetylene ($C_2H_2$) | 36.9 | 54.1 | 61.4 |

***Pulsed Detonation Engine (PDE)***

On of the most researched type of engine using the detonation process is the Pulsed Detonation Engine (PDE). This is because of the simplicity of its design that, in the most basic

version, does not require any moving parts. It is studied both numerically [57–59] as well as experimentally [60–62]. In 2008 the first ever PDE-powered aircraft took off on the Mojave desert in the USA, it is presented in the Figure 5 [63]. As the name suggests, a pulsed detonation engine operates in an intermittent, cyclical manner. In the first stage the tube is filled with combustible fuel – oxidizer mixture. Next, the mixture is ignited and the flame transitions from a deflagration to detonation mode with the detonation wave propagating towards the nozzle. In the subsequent steps the detonation exits through the nozzle and the blowdown of the exhaust gases starts. The final step is the purge of the tube and then the cycle starts again. A basic PDE cycle is shown in the Figure 6 [64]. Pulsed Detonation engines have a number of advantages such as scalability, high Thrust to Weight ratio (T/W), no moving part, higher thermal efficiency. However, they also have some drawbacks. The cyclic operation mode that usually is at the order of 10 to 100Hz is one of the well-known problems. Another is a high level of noise and vibrations produced by this type of engine. Additionally, the extremely high temperatures and pressure shocks results in a short life of an engine parts. What is more the intermittent operation mode is also problematic when the engine is coupled with a turbine because of unsteady interactions of the turbine with the incoming detonation or shock wave [64]. Some of the described problems, such as noise or high pressure and temperature shocks, are inherent to a detonation engine but some of them can be avoided. A Rotating Detonation Engine (RDE), another type of engine utilizing detonative combustion, solves the problem of the periodic operation mode of PDE by introducing a continuous detonation operation.

**Figure 5** The first PDE-powered aircraft flies over a Mojave desert in 2008 [63].

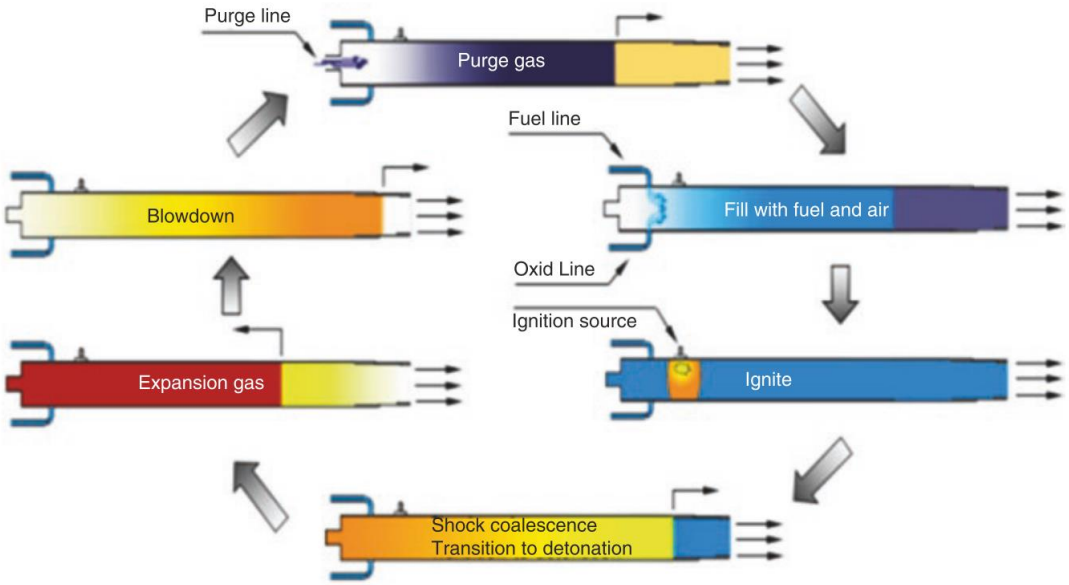


**Figure 6** A depiction of a basic PDE cycle [64].

### *Rotating Detonation Engine (RDE)*

In contrast to a PDE, a RDE does not work in cyclic but in a continuous mode. Once the detonation is initiated in a combustor it keeps propagating circumferentially in the combustion chamber with the exhaust gases being discarded axially. This process continues as long as the mixture of fuel and oxidizer are fed into the chamber and the right conditions are met. Figure 7 presents a schematic diagram of such a chamber. Thanks to the fact that a RDE works in a continuous mode, its operation frequency is a the level of several kHz, which in turn generates vibration level of the same order of magnitude that a typical gas turbine [64]. From the perspective of a combustion efficiency, all engines utilizing detonative combustion offer similar advantages: high rate of energy release, higher thermodynamic efficiency [41]. However, a Rotating Detonation Engine has some additional advantages over a Pulsed Detonation Engine. The first two were already mentioned – a RDE has higher operation frequency and vibration levels comparable to a conventional gas turbine. The latter is even more important when considering a potential integration a rotating detonation combustion chamber with a turbine. Due to the fact, that the geometries of a combustion chamber of a typical turbine engine utilizing deflagrative combustion and a rotating detonation chamber are very similar it is potentially easier to integrate the latter with a typical turbine. What is more, such a chamber will be shorter and more compact compared to a conventional one. This in turn will result in lower engine weight. Because of all those advantages, a concept of RDE gains more and more popularity and interests around the world. It is researched both numerically [65–67] as well as

experimentally [68–72]. What is more, in 2021 the first RDE powered rocket fueled by liquid propellants took off [73]. Nevertheless, as everything, a RDE has also some drawbacks and design challenges. Probably, the most severe one is the typical problem with detonation engine – extremely high temperatures and pressure shocks resulting in a very short life of engine parts (combustion chamber, first stages of a turbine, injectors etc.). Another challenge is that the direction of the flow of burnt gas is not ideally axial but has a tangent component. This poses a problem from the turbine efficiency perspective. However, there was a study conducted by Kindracki et. al. [72] that shown that the direction of the flow on the hot side of the combustor could be potentially controlled by a set of guide vanes placed ahead of the chamber on the cold flow side. Finally, a topic of an injector – detonation wave interaction is equally important and is also being studied by some researchers [74, 75]. This list is by no means comprehensive but serves a purpose to show that although a RDE is a very promising concept, there is still a number of challenges that must be addressed before it becomes a reality.

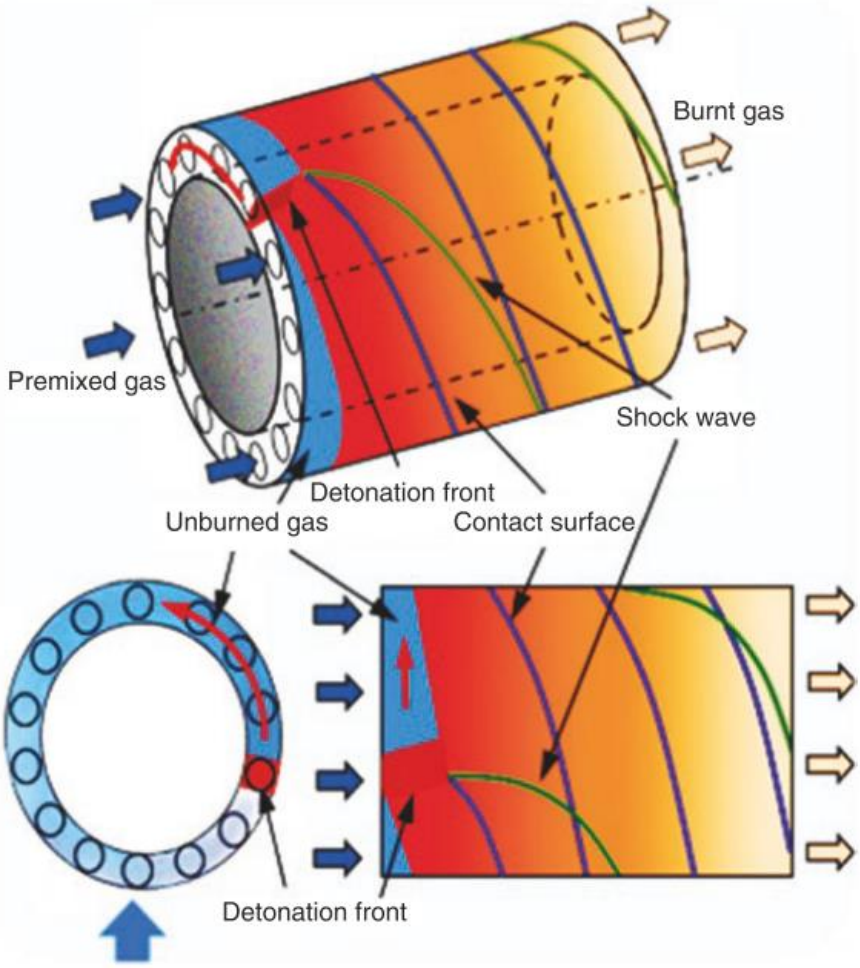


**Figure 7** A schematic of a RDE combustion chamber [64].

### 1.1.4. Machine Learning

Performing experimental research is both expensive and time consuming. A research party needs to first invest a lot funds to build a test stand and then a lot of time to perform the experiments. The more cases one wants to examine the more time it will consume. As an example, an average turnaround time of one experiment that will be presented later in this document was around 40 minutes. It is not possible to resign from doing experimental research at all, but there is a way to lessen the amount of it by using machine learning (ML) techniques. Those techniques can allow predicting the detonation cell size for a new, unresearched mixtures and sets of parameters using the data gathered beforehand during the experiments done on different sets of parameters and thus reducing the overall number of experiments.

There are two main types of learning methods in ML: supervised and unsupervised [76]. In the former the data that is available is used to create (train) a model that lets the user predict some value(s), called 'dependent variable(s)', using a set of parameters called 'independent variables'. Both dependent and independent variables can be either continuous or discrete in nature. Depending on the type of the dependent variable a model is called a regressor – predicting the continuous values, or a classifier – predicting a discrete values, so called 'classes'. In essence, the supervised learning establishes the relationship between the independent and dependent variables, which is similar to the concept of function approximation. In case of the unsupervised learning, the data is not labeled and the model does not predict a number or a class but rather it is used to discover patterns in data or to group similar objects. A simple example would be a model fed with pictures of cats and dogs that, without 'knowing' which is which, divides the pictures in two groups containing cats and dogs by finding some features that differentiates one group from another. In the case of the work presented in this document, only the supervised learning techniques were used and as such only this part of machine learning universe will be presented.

The process of creating a machine learning model is called 'training'. In it the model goes through an optimalization process where its parameters and hyperparameters are optimized so that it returns the best possible results. The difference between hyperparameters and parameters is as follows. The hyperparameters control the learning process and can be set manually by the user, examples include: choice of an optimization algorithm, the learning rate coefficient, number of layers in neural network etc. On the other hand, parameters are internal to the model and cannot be changed by the user. They are the 'knobs' that are being turned during the training process in order to train the best model. A simple example would be the case

of training a very simple linear regression in the form of $y = a*x + b$, where $y$ is a dependent variable and $x$ is an independent variable. In this instance the parameters of the models are the coefficients $a$ and $b$. At the beginning of the training process, those parameters are usually initialized to some value at random and then in the iterative process are corrected in order to achieve the best possible fit of the model to the provided data. It is important to mention, that while training a supervised model the data must be first divided into so called 'training' and 'test' sets. The first one is used to train the model while the second one to test it and ascertain that it will generalize well to the new, unseen data, avoiding so called 'overfitting'. An overfitting occurs when the model fits too closely to the training data resulting in very good results on the training set but fails to generalize well on the new data. An example of overfitting is presented in the Figure 8. On the left side a dependent variable Y vs an independent variable X is plotted. The black line shows the target function without the noise while the orange, blue and green lines present different fitted models with increasing flexibility (degrees of freedom of the smoothing splines). On the righthand side plot the Mean Squared Error (MSE) calculated on the test (red) and training (gray) sets as function of model flexibility is presented. The colored rectangles correspond to the models shown in the plot on the left. It can be seen that although with increasing flexibility the training error decreases the test error quickly starts to rapidly grow. Looking at the left plot one can intuitively feel that the green line seems to follow the data too closely, while it is easily noticeable that the general trend is close to linear.

In the paragraph above one of many metrics used to assert model performance was mentioned – MSE. There are many other metrics used to evaluate how a created model is performing. The decision which metric to choose depends on a number of factor with the most important being if the model is a regressor or a classifier. In the presented work only the regressor was used so only those metrics will be described, and the most popular ones are: Mean Squared Error, Mean Absolute Error (MAE), Mean Absolute Percentage Error (MAPE) and, probably the most popular, coefficient of determination – $R^2$. The definitions of those metrics as well as of all the methods and models used will be provided in later chapters.

Nowadays machine learning is going through its renaissance. The ML techniques are being implemented in almost, if not, all fields of science as well as in all aspects of people's everyday life, examples include: medicine [77–79], churn prediction (in any business) [80, 81], banks [82, 83] or engineering [84–86]. Machine learning opens a third way of performing research, complementary to the experimental research and numerical modeling. In this thesis I will show its application to predict the detonation cell size of biogas – oxygen mixtures.

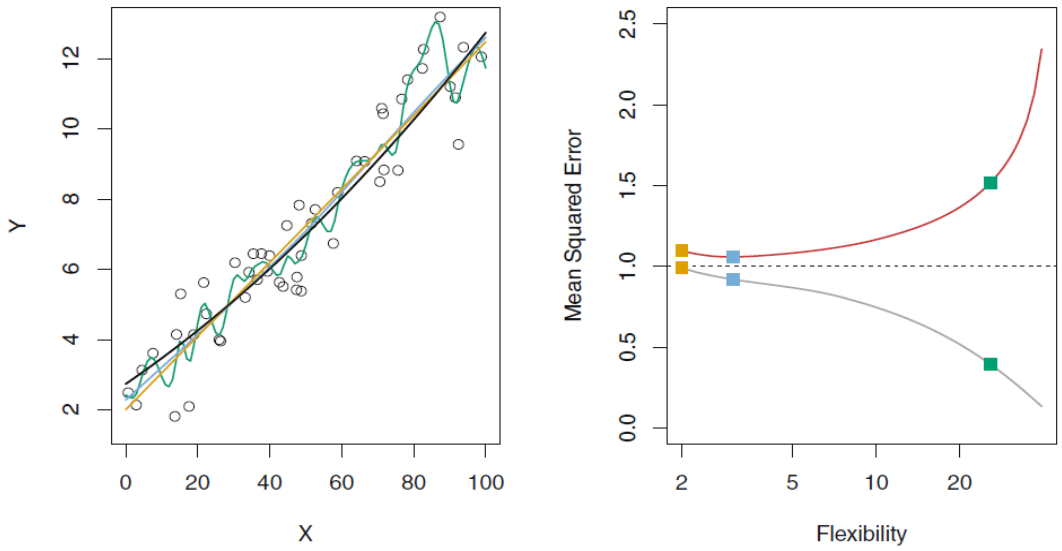


**Figure 8** An example of overfitting [87].

# 2. Objectives and outline

The aim of the presented work was first to experimentally investigate the detonation cell size of a biogas-oxygen mixture and then to create a machine learning model that would allow for reliable prediction of the cell size. The experiments were conducted for a number of different initial pressures $p_0$, equivalence ratios $\phi$ and biogas compositions. As will be shown later in the thesis, the number of studies dealing with the biogas detonation is extremely limited and with biogas detonation cell size, even more so. In this context, the presented research will significantly extend the knowledge base of the biogas detonation parameters.

In the second part of the work, a predictive model was created using the data gathered in the experiments, as there is almost no data available in the literature. The rationale behind it was to create a model that would allow for reliable predicting the detonation cell size for parameter sets that were not experimentally tested. The main thesis of the dissertation is as follows:

*It is possible to create a machine learning model to reliably predict the detonation cell size of biogas-oxygen mixtures with satisfying accuracy.*

The aim of the work was achieved after performing the following steps:

- design and build an experimental stand for gathering the measurements of the biogas – oxygen detonation cell size;
- performing the experiments, gathering and analyzing the measurements;
- creating and validating the machine learning model for predicting the detonation cell size.

The dissertation is divided as follows. Chapter 3 presents the state-of-the-art research on the topic of the biogas detonation and machine learning in the field of combustion with the special consideration for detonation cell size prediction. Chapter 4 shows the experimental research done while preparing this dissertation. It contains results for over 200 cases of different biogas compositions, initial pressures $p_0$ and equivalence ratios $\phi$ for which the detonation cell sizes were measured. Additionally, a discussion about the need for wider statistical description when reporting the detonation cell size measurements is provided. Chapter 5 presents the results of the work done on the machine learning model for predicting the detonation cell size of the biogas - oxygen mixture. Finally, in Chapter 6 the presented work is summarized and conclusions are drawn.

The work presented in this dissertation is a basic research on the topic of biogas – oxygen cell size. However, it also has a long term impact as this research lays the foundations for designing a proper combustion chamber for a detonation engine (either PDE or RDE) fueled by biogas.

# 3. State of the art

## 3.1. Biogas Detonation

As mentioned earlier the number of studies on the subject of biogas detonation is extremely limited. In order to put it into perspective let us start with the work of Dairobi [88] from 2013. They published a feasibility study on a pulse detonation engine fueled by biogas. In the paper, they shortly summarized what is a biogas, how it is acquired and what are its characteristics. They also presented the problems with using biogas as a fuel in a PDE as well as very briefly showed some strategy how to deal with those problems in the future. Finally, they also presented the current state of biogas detonation research that at the time was even more limited than today as they were able to describe only two studies. One was of Saqr et al. [89] studying the influence of hydrogen and hydrogen peroxide additions on the detonation characteristics. The other was the study of Wahid and Ujir [90] that experimentally compared the detonation parameters of biogas to other gaseous fuels. Both of these works will be described later in this section. In general, the research conducted so far on the topic of biogas detonation can be divided into three areas: general investigations of the detonation parameters [89, 91], research on the topic of PDE [88, 92] and research of the detonation cell size [90, 92–95]. All of this research except that being presented in this dissertation was conducted at the Universiti Teknologi Malaysia.

In the topic of general detonation parameters research, in 2010 Saqr et al. [89] studied the effect adding hydrogen ($H_2$) and hydrogen peroxide ($H_2O_2$) on the ideal detonation characteristics of biogas - air mixtures. The idea behind it was that because, depending on the source and production process, biogas can have a low content of methane and as such it may be difficult to achieve a consistent detonation so using highly reactive gases as additions should increase the characteristics and usability of biogas as energy source. The investigation was performed using chemical equilibrium code NASA CEA [96] in order to obtain Chapman - Jouguet detonation characteristics. As mentioned above, they investigated two types of mixtures and for both of them four different equivalence ratios {0.7; 0.8; 0.9; 1.0} and six molar concentration of the secondary fuel ($H_2$ or $H_2O_2$) {0.0; 0.1; 0.2; 0.3; 0.4; 0.5} at the temperature 343 K and ambient pressure were tested. It was found that the addition of hydrogen peroxide provided higher peak pressure and Mach number than of hydrogen. On the other hand, hydrogen mixtures provided higher detonation velocity and temperature. Overall, it was concluded that hydrogen peroxide is favorable over hydrogen as biogas addition. This can be

explained by the molecular composition of hydrogen peroxide. The additional oxygen atom in its molecular structure provides enhanced combustion for biogas, especially near to the stoichiometry and rich limits. In 2022, Rahman et al. [91] investigated the application of one-step irreversible Arrhenius kinetics to the numerical description of biogas - oxygen detonation with varying level of N2 dilution. They showed that the simple Arrhenius rate law (see eq. 13) can allow to calculate the biogas detonation velocity with reasonable accuracy (less than 15% discrepancy when compared to experiments and detailed chemistry model GRI Mech 3.0). This can be done by treating the pre-exponential factor $A_r$ , the temperature exponent $n$ and the activation energy $E_a$ in the equation 13 as variables that can be optimized. In order to find this optimum set of parameters they conducted experiments to calculate detonation propagation velocity using a PDE rig with the length of 1500 mm and inner diameter of 100 mm. The experiments were carried using one biogas composition (65% CH4 + 35% CO2) and varying composition of the oxidizer-diluent mixture that consisted of oxygen O2 and nitrogen N2. Additionally they recreated the experiments numerically by performing simulations in ANSYS Fluent software with the detailed chemistry model (GRI Mech 3.0). Using the data collected from both experiments and simulations they searched for the best set of the parameters described above using a comprehensive validation feedback loop.

In 2020, Elhawary et al. [92] investigated the influence of $H_2$ addition to biogas on the performance of a PDE as well as on the recorded cell size. First, they conducted a theoretical study of the influence of methane concentration in biogas on the detonation peak pressure, temperature and Mach number. For this, they used a chemical equilibrium software - NASA CEA [96]. It was shown that as the methane content in biogas increases all the parameters also increases. After that, they performed the aforementioned experimental research of the influence of $H_2$ addition on the biogas - oxygen mixture. The experiments were performed at the ambient pressure and temperature with the biogas containing 60% of methane and 40% of carbon dioxide. The hydrogen addition ranged from 0% up to 20% in 5% increments, and was added to the prepared beforehand, stoichiometric mixture of biogas and oxygen. As such it was shown that the hydrogen addition increased recorded pressure and Mach number and decreased the cell size up to 15% addition. On the 20% hydrogen addition level the reverse trend was observed, the cell size increased while the pressure and Mach number decreased. This was most probably caused because the overall equivalence ratio of the biogas - hydrogen - oxygen mixture deviated significantly from 1 towards rich mixture (phi > 1). The results of their cell size measurements are presented in the Figure 9. They also tested fueling a PDE with those

mixtures and achieved stable engine's operation at the frequency of 10 Hz for mixtures with 15% and 20% hydrogen addition.

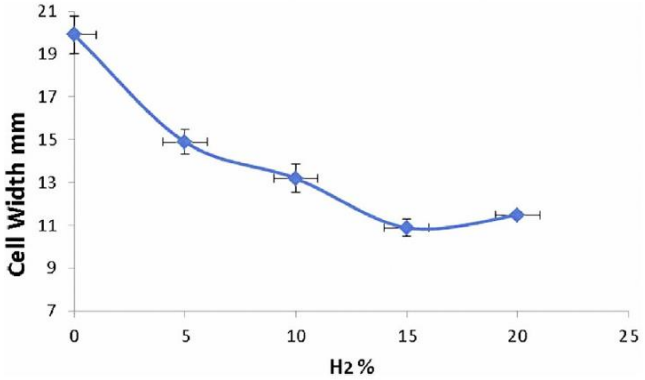


**Figure 9** The detonation cell size plotted vs the hydrogen addition to the 60-40 biogas – oxygen stoichiometric mixture [92].

In [90, 93] Wahid et al. presented the results of their experimental study comparing the detonation cell sizes of biogas - oxygen and hydrocarbon - oxygen mixtures with varying levels of nitrogen dilution. The fuels used were as follows: biogas (65% $CH_4$ + 35% $CO_2$), propane ($C_3H_8$) and natural gas (92.7% $CH_4$ + 7.3% $CO_2$). The experiments were done at the atmospheric conditions, the pressure was equal to 1 atm and temperature to 300 K. It was shown that for the same level of nitrogen dilution propane presented the smallest cell size while biogas the biggest with natural gas in the middle. It was then concluded that out of the researched three fuels, propane is the most sensitive to a detonation initiation while biogas is the least sensitive. Additionally the same was confirmed by comparing the calculated from experiments, as well as theoretical, detonation propagation velocities. What is more it was also shown that for all researched fuels the sensitivity to detonation initiation decreases with increasing nitrogen dilution which is proved by the increase in the detonation cell size. Figure 10 shows the detonation cell sizes measured in that study. The last two articles mentioned above by Siatkowski et al. [94, 95], on the topic of a biogas detonation, are the results of the work performed by the author of this dissertation together with his advisor and a colleague. Those results will be discussed in great details in the subsequent sections.

## 3.2. Machine learning for detonative combustion

As mentioned above, the use of machine learning techniques in most, if not all, disciplines of science is gaining more and more momentum nowadays. The combustion science is no exception. The articles, published in 2020 by Zheng et al. [97] and in 2022 by Zhou et al. [98],

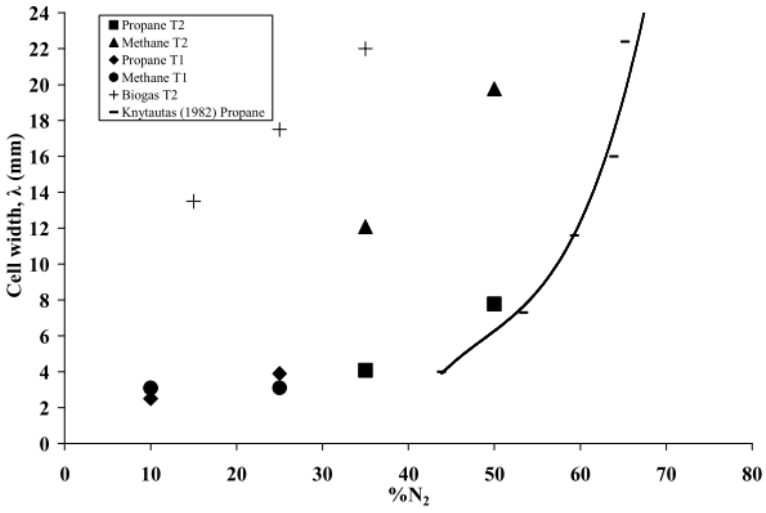


**Figure 10** The detonation cell sizes measured by Wahid et al. [90, 93].

provide a general, wide overview of the numerous branches of combustion science in which the machine learning is already present. Examples of an application of ML in combustions include: fuel properties prediction and fuel design, combustion optimization in engines, combustion instability monitoring, combustion regime diagnostics, combustion kinetic model uncertainty quantification, and many others. However, those overviews are by no means comprehensive and do not cover a lot of work done in the specific topic of detonative combustion. To the author's best knowledge the literature review provided in the following section covers all, or almost all, the work done in that specific topic – detonative combustion, as of May 2023. Nevertheless, those articles ([97, 98]) are useful to make a reader aware and convinced that the machine learning is gaining more and more attention in the research society of combustion scientists. Figure 11a, shows the number of publications in the topic of ML in combustion published in between 2015 and 2020 [97]. It clearly visible that the number of publications was steadily increasing over the last 5 years. It is important to notice that the data for year 2020 is not complete as it only reflects the state of publications up to August 2020. On the other hand, Figure 11b provides the overview of the number of publications treating strictly on the topic of machine learning in detonative combustion. Those number are, naturally, lower than in Figure 11a, but it is also clearly visible that the number of publications rose in the last 3 years. Similarly to Figure 11a, in the Figure 11b the number for year 2023 is not complete as it only reflects the state of the publications up to May 2023.

A thorough literature review revealed that the published papers can be grouped into specific 'research topics'. In such groups the research revolves around different aspects of a

given topic or different solutions, or ways to approach it. In the subject of machine learning in detonative combustion most of the articles fall into the three following groups:

- predicting the detonation cell size
- reconstructing the detonation front
- real-time RDE diagnostics

The following subsections are going to present the state of the art following this grouping. Additionally, the articles that did not fit into any of the groups will be presented collectively in the last subsection.

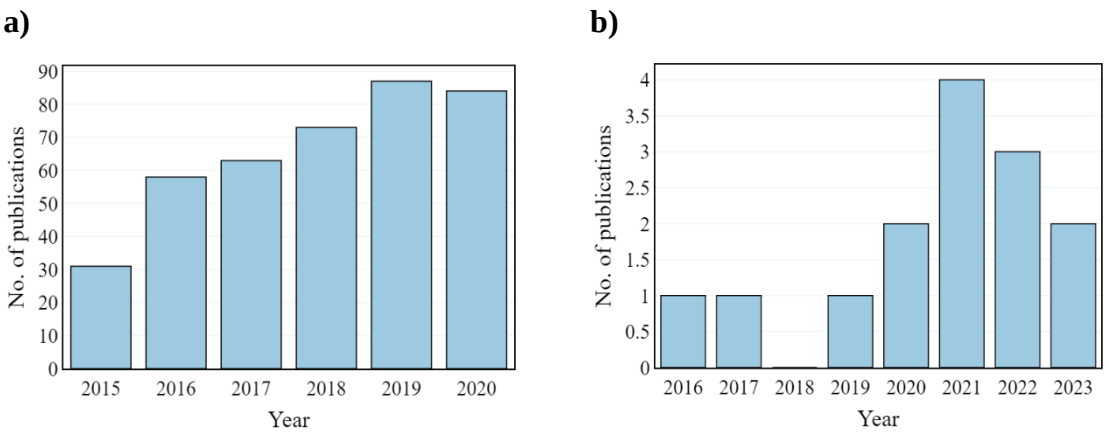


**Figure 11** Number of publications in a topic of: a) machine learning in combustion science, reproduced from [97]; b) machine learning in the detonative combustion.

### 3.2.1. Predicting the detonation cell size

As the main focus of this dissertation is the detonation cell size of the biogas, this review will start with the detonation cell size prediction. In 200 Gavrikov et al. [99] presented, probably the first, widely used and referenced model for predicting the detonation cell size. They started with the model proposed by Schelkin and Troshin [100] and then expanded their idea proposing more robust model. The model proposed in [100] was in a form of the following, simple correlation: $\lambda/\delta = A$ . This can be interpreted that the detonation cell size is proportional to the reaction zone width, calculated on the basis of the ZND model of 1D detonation wave. It was shown, that if a suitable factor A is provided that model captures the effects of mixture composition, temperature, and pressure in a qualitative manner. However, it does not provide accurate quantitative results. As such, Gavrikov et al. expanded the idea and showed that the model can be vastly improved by treating the factor A (in other words the ratio: $\lambda/\delta$) not as a constant but as a function. This function takes two parameters describing the stability of the detonation - dimensionless effective activation energy ($E_a/RT_{ps}$) and a parameter describing the

relation between chemical energy and initial thermal energy of the combustible mixture ($T_{vn}/T_0$). The $E_a$ is the activation energy, R is the gas constant, and T and p are temperature and pressure, respectively. The subscripts *0, ps* and *vn* represents the initial state, the post-shock state and von Neumann state, respectively. In order to find the best correlation they used a linear regression technique and an extensive feature engineering. The two parameters above were transformed and provided to the model in many forms, for example as ln(X), 1/X, $X^2$ etc., where X symbolizes one of the two parameters. The created semi-empirical correlation proved to yield significantly better results than the Schelkin's model for a wide range of different mixtures and initial conditions. Additionally, it was tested on a data that was not used for training and also provided satisfying results. Nevertheless, the authors noted that the estimates of λ provided by the model should be treated carefully if the values of the input parameters reach outside the range on which the model was trained. Additionally, they also mentioned that when applying the methodology, the limitations of the kinetic calculations (in their case with the CHEMKIN-II [101] code) should also be taken into consideration.

In 2017, Yu et al. presented a Support Vector Regression (SVR) model for predicting the cell size of various combustible mixtures. The fuels were mostly hydrogen but also different hydrocarbons and the oxidizer was either air or oxygen, additionally different dilutants such as $CO_2$, Ar, He, $N_2$ were tested as well. The data came mostly from the detonation database [102], but also from unpublished experiments. The independent variables used in the study were as follows:

1. dimensionless activation energy: $\frac{E_a}{RT_{ps}}$
2. dimensionless temperature: $\frac{T_{vn}}{T_0}$
3. dimensionless pressure: $\frac{p_{ps}}{p_0}$

The authors created and tested the model in two versions: containing two independent variable (no. 1 and 2) and all three. Additionally, they compared the results of the SVR models with parametric regressions using the same features. It was shown that adding the third variable to the SVR improved the results significantly making the SVR with three features the best model in the study with the $R^2$ score reaching 87,6%.

In 2018 Malik et al. [103] published an article in which they showed a neural network (NN) trained for predicting the detonation cell size for different combustible mixtures being a combination of the following fuels: methane, propane, hydrogen, and oxidizers: air, oxygen.

That kind of model needs a lot of data for training which is usually not available from the literature because only average cell size values are reported. In order to compensate for that, the authors used simple, interim models in form of polynomials fitted to the available data points. Using the fitted curves and additionally assuming normal distribution of the cell sizes as well as approximating a value of standard deviation by a rule of thumb ($\sigma \approx \frac{\max - \min}{4}$), they simulated the data points to use while training the model. An example of such simulation is shown in the Figure 12. The black dots with vertical lines depicts the data points from experiments with estimated standard deviations while the light-gray points are simulated using a fitted polynomial and the assumptions described above. In their study the authors checked a number of features generated using the Cantera software [104]. Ultimately, the model consisted of two continuous independent variables being the adiabatic flame temperature and fuel fraction in the mixture and a third variable indicating which mixture is under consideration ($H_2$ – Air, $CH_4$ – O2, etc.). The authors showed that the model achieved satisfying performance with $R^2$ ranging from 78% up to 99%, depending on the type of mixture. What it more, it proved to perform better when compared with the Gavrikov's empirical model [99]. The advantage of the presented approach over the one presented by Yu et. el. [105] was that the model did not rely on a-priori assumptions of the activation energy or reaction width. However, on the other hand the process of simulating the data points introduced the uncertainty of its own. What is more the encoding of the type of mixture is not a valid and sustainable solution in case of extending the model for a larger number of mixtures.

Lastly, in 2023 Bakalis et.al. [106] presented a research in which they created a series of Artificial Neural Networks (ANN) predicting the detonation cell size using different sets of chemical kinetic and thermodynamic parameters as independent variables. The number of independent variables in the models that was checked ranged from 1 to 7. The researched parameters were as follows: the initial pressure $p_0$, the initial temperature $T_0$, the equivalence ration $\phi$, the Mach number $M_{CJ}$, the induction length $\Delta i$, the maximum thermicity $\sigma_{max}^{\cdot}$, the activation energy $E_a$ and the stability parameter $\chi$ [107]. The authors showed that a model using only three of those parameters (induction length, thermicity and Mach number) provided

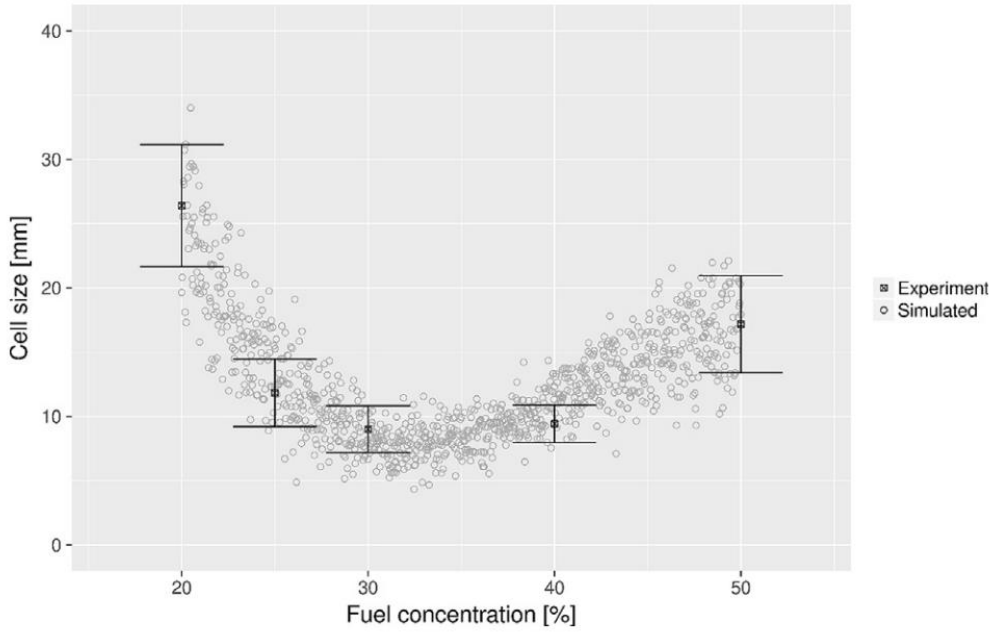


**Figure 12** An example of simulated 1000 cell sizes (light grey points) for H2 – Air mixture, as a function of fuel concentration [103]. The black dots with vertical lines represents the average cell sizes collected from literature and the estimated standard deviation, respectively.

accurate estimations of the detonation cell size. What is more, further increasing the number of feature did not improve the accuracy sufficiently enough to justify adding to complexity of the model. It is also worth noticing, that the three parameters that were found to give the best results relate indirectly to the stability parameter $\chi$. The data for training and testing the results was obtained from the detonation database [102] (initial conditions, mixture composition, cell size) and CHEMKIN II package [101] (chemical kinetics parameters). The average prediction error achieved by the 3-feature model was at the level of 22%. As a comparison, existing models developed or applicable for a wide range of applications such as those proposed by Gavrikov [99] and Ng et al. [108, 109] have the mean absolute percentage error at the level of about 50%. However, it is important to notice, that as the authors commented, the limitation of the model is that it uses features calculated by a single chemical kinetics mechanism (Konnov [110]). This is a potential drawback in cases where other mechanisms tailored specific for some other mixture were to be employed.

### 3.2.2. Reconstructing the detonation front

The next research topic found in the literature was the effort to reconstruct the detonation wave front using machine learning techniques. In 2020, Zhang et al. [111] proposed a reconstruction method of a detonation wave cellular structure based on a post-surface flow field. In order to do that they used the proper orthogonal decomposition (POD) method coupled

with the Neural Network. The POD was employed to extract a reduced number of features from the post-surface pressure field and translate it back to a full flow field of a detonation using the neural network. The data was obtained by conducting numerical simulations and extracting the flow fields with various wave structures from them. The method proved to give good results with an overall average relative error of around 9.4% for a stable detonation waves. However, for unstable oblique detonations the results were significantly worse with an overall, average error raising to 24.8%. Nevertheless, it was showed that the method has a potential as a way to reconstruct and research the cellular structure of the detonation except for a traditionally used smoked foil technique. In the article only pressure field was reconstructed but the method could also be applied to any other parameter like velocity field, species field, etc.

In 2021, Zhou et al. [112] took the work a step further and tackled the problem in a slightly different way. They dropped the POD and proposed a method of reconstructing a shock front present in a detonation structure using information of the state of the reactive front. In order to do that they introduced a simplified approach of predicting the distance between the leading shock and the reactive front using a multi-layer perceptron (MLP). The positions of both zones were simplified as the points corresponding to the reaction index equal to 0.5 for the combustion front and the location where the pressure value is twice of that of pre-shock for the shock front. The reaction index represents the reaction progress in the steady ZND detonation and varies from 0 (for unburned reactant) to 1 (for combustion products). The value of 0.5 means that half of the reactants were consumed. In the Figure 13, an example of typical temperature field obtained from the simulations is presented. Additionally, the positions of the reactive front (black, dashed line) and leading shock (white line) are also marked. Multi-layer perceptron is one of many possible architectures of a neural network. It is the oldest one and in literature is usually referred to as simply neural network (NN) or artificial neural network (ANN). In order to train and test the model the authors used 1D and 2D numerical simulations of a detonation, using the reactive Euler equations with a one-step irreversible chemical reaction model [113]. The data gathered from those simulations in form of snapshots of parameters from the grid points was used both as dependent and independent variable. The former was, the aforementioned, distance between the reaction zone and leading shock while the latter were: density $\rho$, temperature T, velocities $u$ and $v$ (in X and Y directions, respectively), as well as the temperature and density gradients in the X direction T' and $\rho$'. It was shown, that in case of 1D simulations, the MLP trained on three parameters (T, $\rho$ and $u$) achieved an average relative error below 1% for both training and test sets. In case of 2D simulations, the error increased

and problems with generalizations appeared but as the authors themselves mentioned, this was the first work of this kind and the results proved to be promising. Given more attention into a development of such a model it might be a very useful tool allowing for quick and relatively easy reconstruction of shock front structure using the measured or known reactive front parameters and images of the heat release zone obtained during experiment through, for example, planar laser induced fluorescence (PLIF) imagining method. Nevertheless, it is important to mention, as the authors observed, the method still needs to be developed further as the set of parameters that gave the best performing model might not be fully available from the experiments due to technical limitations.

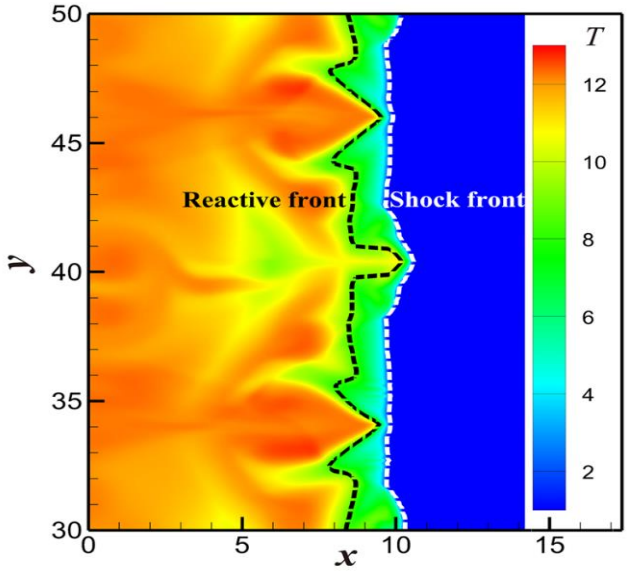


**Figure 13** An exemplary temperature field obtained from simulations, with reactive (black) and shock fronts (white) marked [112].

The final work in this topic is the article of Bian et al. [114] which they further developed the method presented in [112]. However, this time they used a Convolutional Neural Network (CNN) instead of a multi-layer perceptron. This was caused by the fact that this time the number of input parameters was significantly higher as they did not only use six parameters gathered from one grid point (as in [112]) but also from K pointed above and below it. The parameters used in the study were the same as in [112]. This, in turn, resulted in 6*(2K+1) parameters which proved to be challenging from the computational point of view. Because of that, the authors decided to use different neural network architecture - CNN, that has the advantage of parameter sharing and sparsity of connections when compared to MLP. They idea of using additional K grid points to predict the distance between the reaction zone and shock front tried to reflect the fact that the vicinity of any given point in the reaction/shock front influences its parameters. In the Figure 14 the black and white dashed lines represents the

reaction and shock front, respectively. The red dot is the point for which the distance to the white dot is being predicted using the six reaction front parameters gathered from the point itself as well as from the K black dots above and below it. The training and test data was provided in the same way as in [112] - through a numerical simulations, but only 2D this time, without 1D. The authors showed that the CNN achieved better results than MLP. However, again there were problems with generalizations when the model was tested for simulations run with different values of energy activations. Nevertheless, this series of articles shows a promising work direction in the topic of reconstructing the shock front in the detonation wave using a machine learning technique.

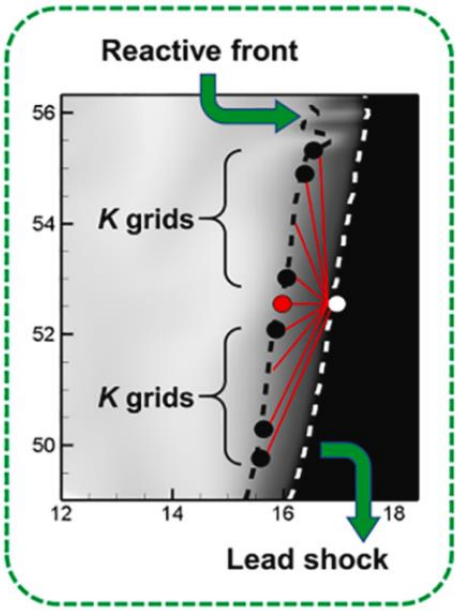


**Figure 14** An illustration of the data gathering setup. The model predicts the distance, in the X direction, between the red and white grid nodes, using not only data from the red dot but also from K black ones above and below it [114].

### 3.2.3. RDE diagnostics

The last research series found in the literature was the series of articles by Johnson et al. [115–119] on the topic of Rotating Detonation Engine diagnostics. In [115, 117], Johnson et al. used a Convolutional Neural Network to identify a differentiate between ten work modes of a RDE. The modes included deflagration, clockwise and counterclockwise co-rotating waves (from one to three), as well as single, double and triple counter-rotating waves. In order to train the network a set of individual down-axis images of the combustion waves, manually labeled by researchers was provided to it. Additionally, another set of labeled images - the validation set - was used to evaluate model's performance on new, unseen data. The results showed that it is possible to accurately differentiate between the ten modes of the detonation wave in the

combustion chamber of the RDE using only a single image. The authors claimed that those results show that it is possible to circumnavigate the need for signal processing or analyzing a sequence of images which substantially reduces the computational complexity and power needed to achieve the task. As a results it is the next step towards further integration of a machine learning in RDE research and real-time diagnostics. Especially the latter will be much needed when the concept of RDE progresses from the research state into a real-world usage. It is however very important to notice that the authors pointed out that the quality of an image is of critical importance for the model's results.

In this 2021, Johnson et.al. [116] tackled the same problem as previously [115, 117], although in a different manner. Instead of using a Convolutional Neural Network they used a computer vision method called "You Only Look Once" (YOLO) to detect the detonation waves. This method, just as any ML mode, also requires to be trained using a set of labelled examples. However, after the training phase, it is able to identify the objects almost in real-time. The authors reported that they were able to achieve a resolution of 20 μs in tracking the location and rotational direction of the wave allowing them to reliably calculate the detonation's average velocity using as few as 10 frames. It is also important, that in contrast to the their work presented in [115, 117], the currently presented method is impartial to wave modes not included in the original training set and calculates the wave velocities independent of the high-speed pressure data. The difference, between the previous method and the one presented, is that the former was only classifying between 10 modes provided during training while the latter detects objects rather than classifies them and is insensitive to the number of different cases.

In the next work, Johnson et.al [118], took yet another approach in the topic of RDE diagnostics. They decided to perform time series classification using the data obtained from ion and pressure probes placed near the detonation propagation plane in a tested RDE. Using this data gathered during the experiments they created 8 datasets with varying sample rates: 200, 500 and 700 samples, out of which 6 were univariate and 2 were multivariate. Next, the datasets were labeled using the down - axis images obtained at the same time during the experiments. Finally, 24 neural networks were trained using the aforementioned data, using three different deep learning architectures for every dataset - an encoder network, a fully convolutional network and a residual network (ResNet). It was shown that models trained on shorter data lengths and multivariate datasets had better results, with multivariate encoder proving to be the best. However, as the ultimate goal was to progress in the topic of real-time RDE diagnostics, the prediction time of a model also needed to be taken into account. It is defined as the time

that elapses between providing the input data to the model and receiving the prediction. In that context, the fully convolutional network proved to be the best having the shortest prediction time of 28,76 ms while maintaining the prediction accuracy on the high level of over 91%. The classification time of this network translated to a classification rate of almost 35 Hz which outperformed the image classification model described in the previous paragraph ([118]).

Finally, in 2023, the authors [119] presented the comparison of methods described in the previous studies [115–118], taking into consideration a diagnostics feasibility, external applicability and performance of those models. Additionally, they evaluated the models alongside conventional techniques in order to assess their real-time diagnostics capabilities. The conventional methods and image classification method described in [116] are both limited only to post processing and cannot be used in real-time. On the other hand, the image [115, 117] and time-series [118] classification models are not restricted to post processing and could be used in a real-time diagnostics. However, as they require an additional correlation of sensor data, their time-step resolutions is around 80 ms. It was shown that no single method outperforms the rest across all metrics but rather they can complement each other across them.

### 3.2.4. Other works

Except for the works presented above, there were also some standalone articles that could not be grouped together. Those presented in this subsection.

In 2016, Wolff et al. [120], created a model for detecting the misfiring of a tube in an annular pulsed detonation combustor. This kind of combustor consists of a number of pulsed detonation tubes that are firing in a predetermined sequence into a common downstream annular plenum. Misfiring event of even one tube can significantly lower the performance or stop the engine. In order to create the model, the authors built a mockup of an annular pulsed detonation combustor using loudspeakers to mimic the acoustic signature generated during an engine's operation. Using this setup to generate data of both correctly and faulty working engine, they trained an artificial neural network (ANN) to classify if a tube is working properly or is misfiring. It was showed that a very good results can be obtained on a level of 99% accuracy on a test set, proving that an ANN can be successfully used to diagnose a PDE.

In 2021, Barwey et al. [121] showed an interesting work focused on creating a model for predicting the source terms of different combustion regimes encountered within a detonation wave. In order to do that, they divided the work into two phases. In the first one, they used a K-mean clustering method to delineate different combustion regimes present in the detonation

wave. The method was used on the results of detailed numerical simulations of a linearized model detonation engine (LMDE). They showed that the optimal number of delineated regions is six, and that a physical representations can be assigned to them. The regions represented the following regimes: ambient fuel-air mixture, a strong detonation region, a shock separated region in the absence of fuel and post-detonation deflagration areas withing the reaction zones. In the phase two, they used the results of the simulations and clustering to train six local neural network that used the data from the separated regions for training. Additionally they created a global neural network trained on the whole simulation results, disregarding the clustering. The goal of the networks was to predict the source terms for every grid point of the simulation. It was shown that it can be achieved and that using the local networks yielded better the results when tested on the unseen data from the LMDE configuration. However, it is important to notice that when the models (local and global ANNs) where tested on the unseen configuration of detonation propagating through a stratified mixture, they failed to generalize well and showed poor performance. Nevertheless, the locally trained models worked better than the global one. This shows that there is still work to be done in this filed but the results are promising. The work presented in that paper is claimed by the authors to be the next step towards enabling the prolonged simulations of complex combustor geometries, for examples of RDE, by bringing down the computational cost of running them.

The final work presented in this review is the article Ryu [122]. The author tackled the problem of predicting the mode (deflagration/detonation) of the reaction front initiated from a hot spot by the use of the machine learning techniques. This kind of analysis is hard to research experimentally due to a very high pressure of the detonation and the fact that it is extremely difficult to set the right conditions for a detonation initiation in mixtures that are not homogenous. It is also computationally very expensive because of the stiff governing equations with detailed chemical kinetic models. In this context, the machine learning models that, when trained properly, can generalize sufficiently well to new, unknown conditions promise to be a good solution. In the article the author presented the results of a comparison of three different predictive algorithms: logistic regression, decision tree, and neural network. Additionally, he compared them to a widely used Zel'dovich reactivity gradient theory [123, 124]. There were six independent variables: normalized temperature difference between the hotspot center and ambient temperature, hot spot radius, ambient temperature, ambient pressure, equivalence ratio and fuel type (either H2 or syngas: 50%$H_2$ + 50%CO). The data for training and testing the results came from a detailed numerical simulation. There was 82 different cases in total, with

varying sets of initial conditions. The accuracy of the model based on the Zel'dovich reactive gradient theory was at the level of around 38% while the logistic regression and decision tree both gave the accuracy of over 70%. The best results were achieved by the neural network with the accuracy reaching 85%. However, it is important to mention that the author himself recognized that the number of gathered data points was quite low. This in turn resulted in the problem with having enough data in the test set to sufficiently represent the range of the conditions. Additionally, the author suggested that through careful feature engineering like scaling or normalizing the independent variables as well as by expanding the sample size, the model should be able to achieve even better results. Nevertheless, the potential of using the machine learning techniques in order to predict the combustion mode of a flame initiated in the hot spots was shown.

# 4. Experimental research

## 4.1. Experimental setup

The experiments were conducted in the Institute of Heat Engineering at Warsaw University of Technology. A total number of experiments was 389, including the experiments conducted while testing the setup and those that needed to be repeated. Three main reasons for a repetition of an experiment were:

- the visible cells were very big which resulted in a low number of acquired measurements from one experiment;
- the foil on which the cells were recorded was destroyed during the experiment;
- the soot on the foil was blown out by the reflected shock wave.

During the study a wide range of initial pressures, equivalence ratios and biogas compositions was tested. The biogas used, was an artificial mixture of methane and carbon dioxide mixed in different volume proportions. The notation for mixture composition used in this thesis is as follows: XX% $CH_4$ + YY% $CO_2$ where XX represents volume percentage of methane and YY volume percentage of carbon dioxide. For example, 65% $CH_4$ + 35% $CO_2$ means a mixture containing 65% methane and 35% carbon dioxide. Throughout the dissertation a simplified notation in the form of XX-YY (e.g. 65–35) is used. The exact, tested values of the parameters are as follows:

- initial pressure $p_0$ [bar]: {0.6; 0.7; 0.8; 0.9; 1.0; 1.2; 1.4; 1.6};
- equivalence ratio $\phi$: {0.5; 0.75; 1.0; 1.25; 1.5}
- biogas composition: {70-30; 65-35; 60-40; 55-45; 50-50; 45-55; 40-60}

It is important to note that for the biogas compositions 45-55 and 40-60 the experiments were carried out only for $\phi = 1$ while for the remaining compositions, the experiments were done for the full range of $\phi$. At the same time, for every combination of the mixture composition and $\phi$, the experiments were carried out for the full range of the initial pressure $p_0$.

The experimental setup consisted of four subsystems:

- the detonation tube;
- the ignition device;
- the data acquisition system;
- the filling and evacuating system;

The subsystems are described in greater details in the following subsections. Figure 15 presents a schematic overview of the test stand while Figure 16 shows photographs and a 3D model of the entire test stand with the aforementioned subsystems outlined.

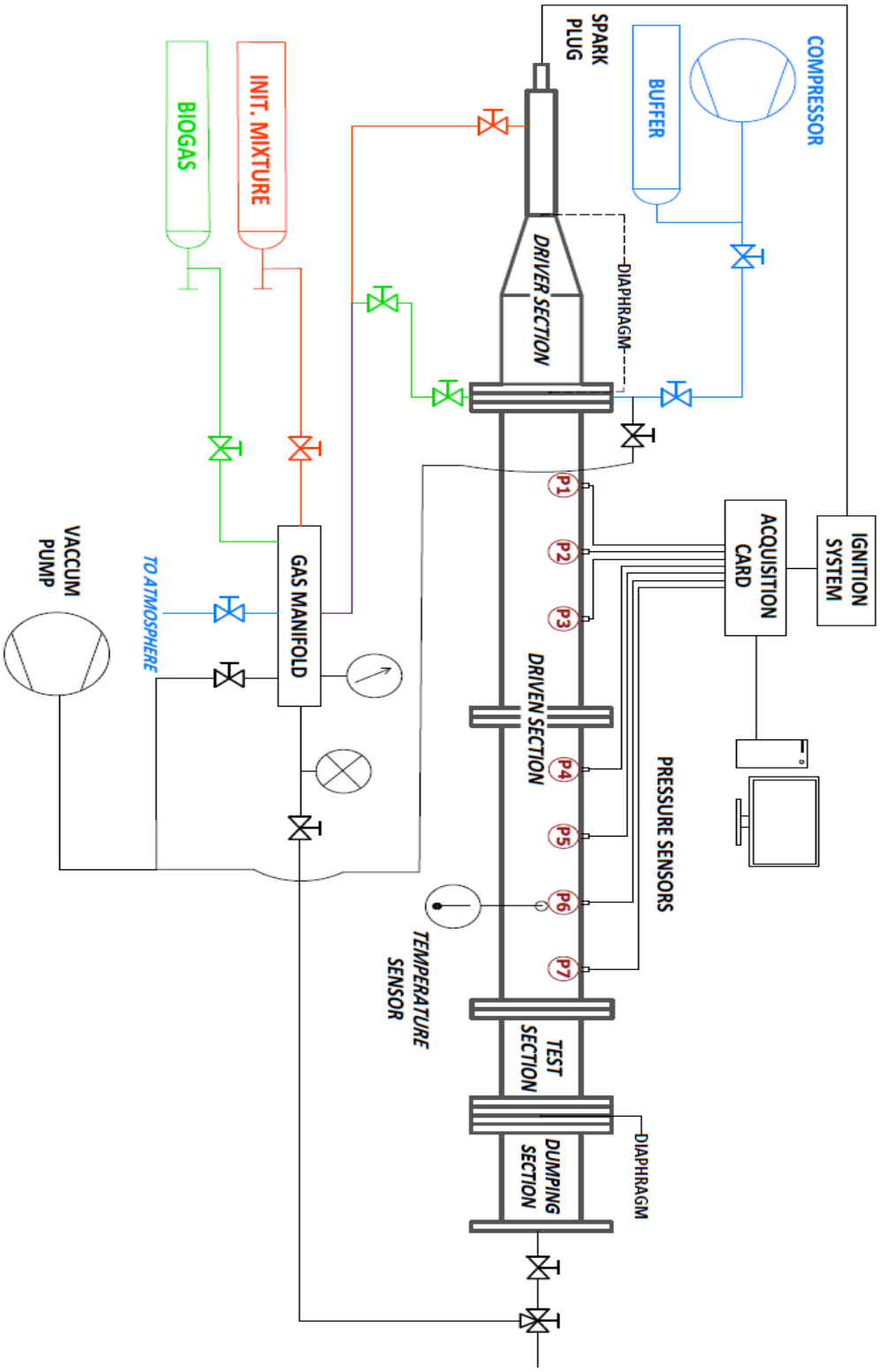


**Figure 15** Test stand configuration schematic.

**a)**

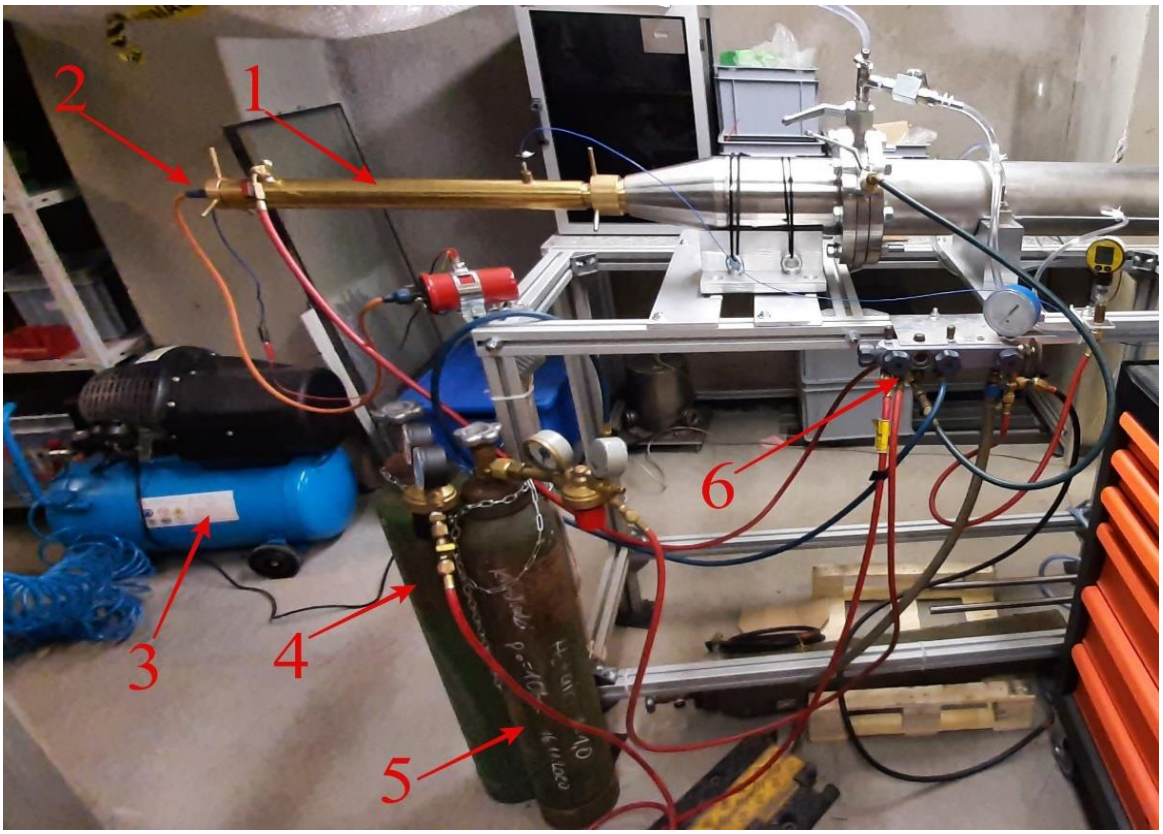


**b)**

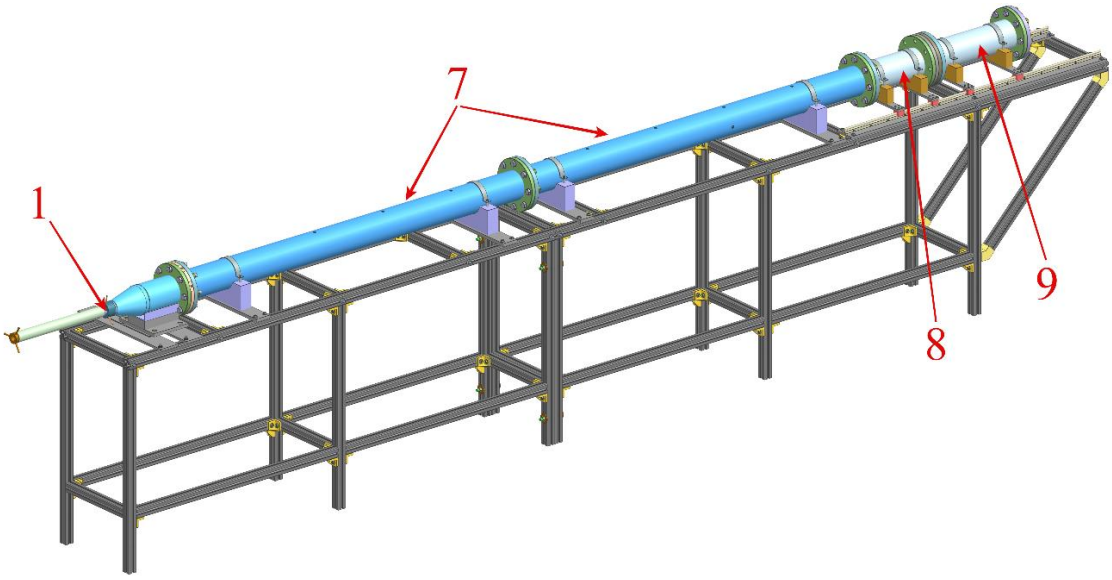


**Figure 16** The experimental stand: a) driver section and parts of the filling and evacuation system: b) the model of the detonation tube; 1 – driver section; 2 – spark plug; 3 – compressor; 4 – $H_2$ – $O_2$ initiating mixture; 5 – biogas – oxygen mixture; 6 – gas manifold; 7 – driven section; 8 – test section; 9 – dumping section.

### 4.1.1. The detonation tube

The main part of the test stand was the stainless-steel detonation tube with an inner dimeter of 122.2 mm, a total length of 4718 mm and a volume of 54.7 $dm^3$. It was divided into four sections: driver section, driven section, test section and dumping section, as shown in the Figure 15 above.

The driver section consisted of a smaller tube, usually referred to as 'initiator', and a short cylindrical tube connected by a conical section. The smaller tube had an inner diameter of 30 mm and volume equal to 0.343 $dm^3$. The driver section purpose was to ascertain repeatable detonation during the experiments. In order to achieve that, it was filled with the stoichiometric hydrogen – oxygen mixture with the pressure that ranged from 3 to 4 bars depending on the initial pressure in the detonation tube (the higher the $p_0$ in the tube, the higher the pressure in the initiator). The $H_2 – O_2$ mixture was chosen because it is a highly reactive and quickly develops a stable CJ detonation upon ignition. The conical section helped to further ease and smooth the transition of the detonation from the tube of smaller diameter to larger diameter. The two mixtures ($H_2$-$O_2$ and biogas – oxygen) were separated by a thin foil membrane that was placed either between the small tube and the conical section or after the short cylindrical section. Its position depended on the initial parameters of the tested mixture, usually for mixtures with low methane content it was needed to place the membrane after the short cylindrical section. This was because the flame tended to decouple from the leading shockwave after transitioning from the smaller tube to larger one and the detonation transitioned into a fast deflagration.

The driven section was 4 m long, divided in the middle into two tubes. Along its length, seven pressure and one temperature sensors were placed. The positions of the pressure sensors are shown in the Figure 17. The pressure sensors will be described in the section concerning the acquisition system. An exemplary pressure traces recorded during an experiment are presented in the Figure 18, they were used to ascertain that a detonation took place. Detonative combustion is easily recognizable as it presents itself as a sharp 20-30 fold spike in a pressure. In the plot, seven traces from seven sensors are shown on one plot with common X-axis. It is clearly visible that the detonation wave passed subsequently every sensor one by one by the delay in pressure spikes. Additionally, the longer distance between third sensor P3 that is the last in the first segment of the driven section and the sensor P4 that is the first in the second section is visible. This can be recognized by the longer time gap between spikes on P3 and P4 in the Figure 18. The temperature sensor was a simple, digital thermometer used to measure

the temperature of the fresh mixture before running the experiments and after filling the tube. During the experiments, the temperature of tube was slowly raising due to a constant, repeated exposure to detonation waves. As a consequence, in the time between filling the tube and running the experiment, the fresh mixture was also heated up. However, the fluctuations in the registered temperature had an amplitude of around 5°C which, based on the literature [125] as well as on the author's experience, was assumed negligible and not influencing the cell size.

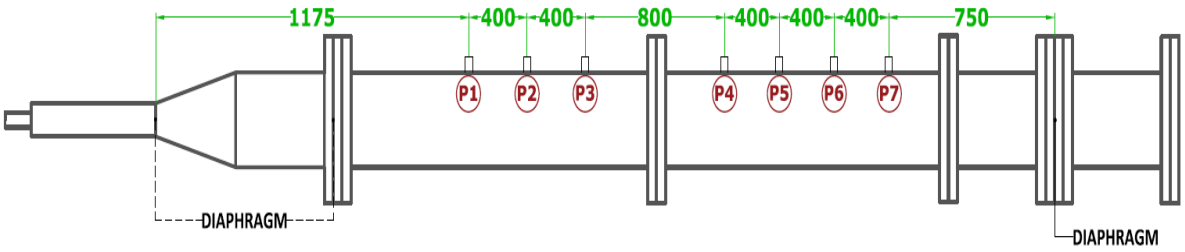


**Figure 17** The schematics showing the positioning of the pressure sensors in the driven section of the detonation tube.

After the driven section, a 350 mm long test section was mounted. Inside it, a smoked foil on which the cellular structure of the detonation was recorded, was placed. The sheet was mounted in such a way that it lined the wall of the tube. The foils preparation process is described in the section 4.2., later in the document.

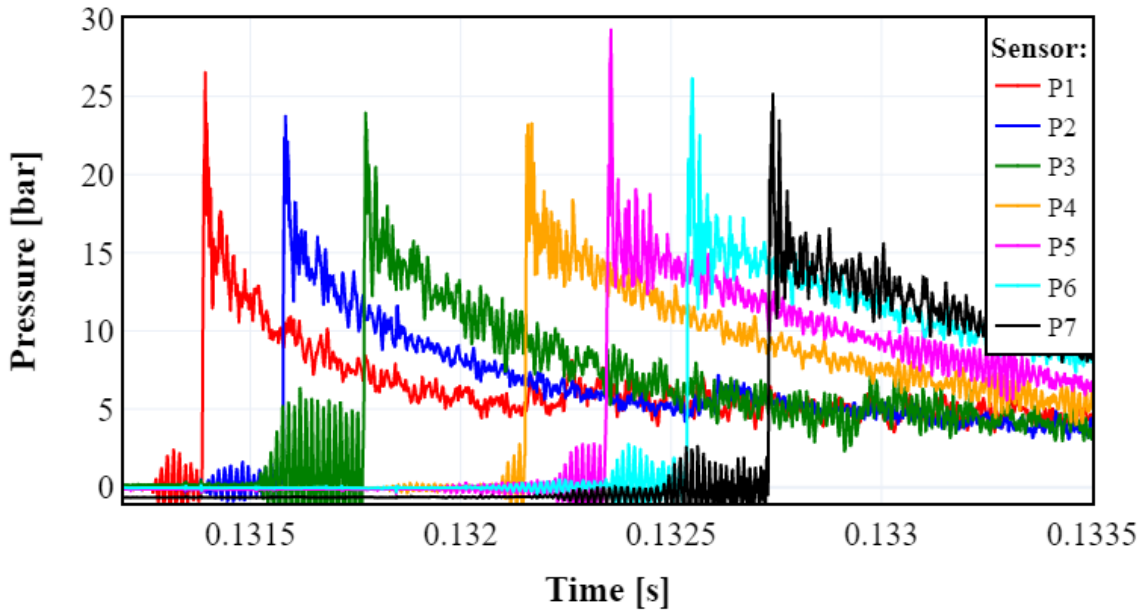


**Figure 18** An example with typical pressure traces characteristic of a detonation.

The last section of the detonation tube was the dumping section. It had a length of 500 mm and was filled with densely packed circles of steel mesh of different mesh sizes. The

purpose of this section was to attenuate the detonation wave and prevent the shock wave reflected from the end of the tube from blowing out the cell pattern recorded on the foil in the test section upstream. In order to increase the attenuation effect the dumping section was separated by a foil membrane from the rest of tube and evacuated before the experiment. Figure 19 shows the inside of the dumping section after a number of experiments.

**a)** **b)**

**Figure 19** The inside of the dumping section: a) the damaged mesh circles after a number of experiments; b) new portion of the mesh circles added on the top of the old ones.

### 4.1.2. The ignition system

The ignition system consisted of a high energy spark plug and an ignition coil. The parts were standard parts used in automotive industry. It was connected to the acquisition system that initiated the detonation when the experiment was started. Figure 20 shows the parts of the ignition system mounted on the test stand with the positions of the spark plug and the ignition coil marked.

### 4.1.3. The data acquisition system

The data acquisition system consisted of a computer with in-house software that controlled the course of the experiment. To the computer a National Instruments PCI 6133 data acquisition card was connected that collected the data from the sensors with the frequency of 2 MHz. The pressure transducers used in the experimental campaign were PCB model 113A24. They were employed to record the pressure traces in the tube. From those readings the time of arrival of the detonation and the detonation peak pressure were read. Figure 21 presents the computer post used to control the course of the experiment.

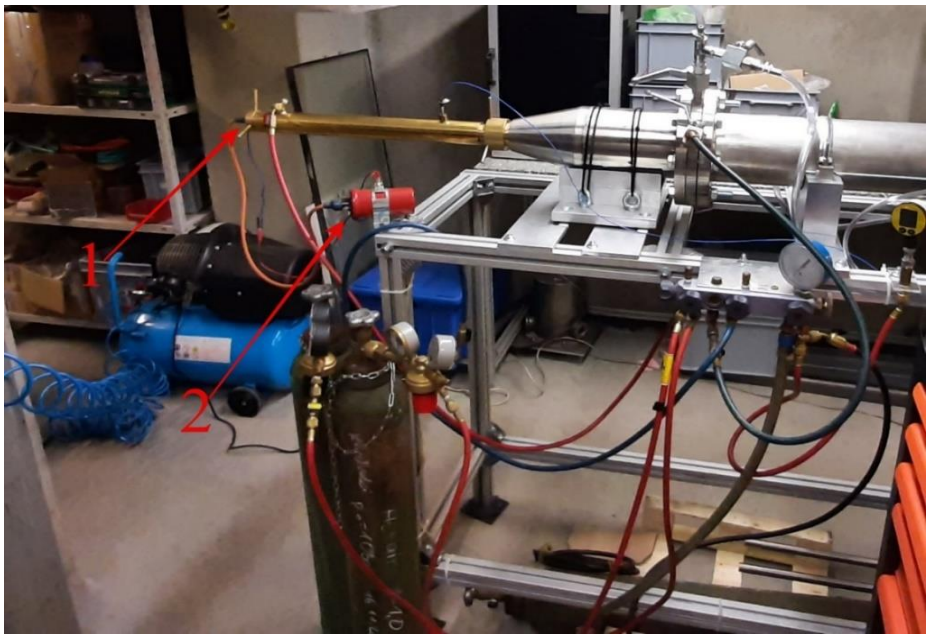


**Figure 20** The ignition system mounted on the test stand: 1 - spark plug; 2 - ignition coil.

**Figure 21** The computer with the in-house measurement software and the acquisition card.

### 4.1.4. The filling and evacuating system

The last subsystem of the test stand was the filling and evacuating system. An oil vacuum pump was used to evacuate the detonation tube before filling it with combustible mixture and to remove the combustion gases after an experiment and before opening the tube to remove the smoked foil. The compressor was used mostly to remove the remnants of the combustion gases and to cool down the tube by purging it with compressed air. The set of tubes, gas manifold, pressure gauges and bottles with initiating and test mixture completed the subsystem. In order to control the process of filling in the detonation tube a digital pressure

manometer Keller LEO 2 was mounted on the gas manifold. It had an accuracy of ≤0.1% FS, which in the case of manometer's scale of 0–30 bar gave an accuracy of 0.03 bar.

### 4.1.5. Mixture preparation stand

The combustible mixtures, both hydrogen – oxygen and biogas – oxygen, were prepared in the gas cylinders using the partial pressures method at least 24 hours before the experiment to ensure the homogeneity of the mixture. The pressure in the gas cylinder was always set to 10 bar abs. Figure 22 presents the schematic of the mixture preparation stand. It consisted of a gas manifold to which an oil vacuum pump and gas cylinders with gases and one for creating the combustible mixture were connected. Additionally, on line was left unconnected to enable venting the system into the atmosphere. In order to control the process of creating the mixture the same digital pressure manometer Keller LEO 2 that was described in the subsection above was used.

**a)**

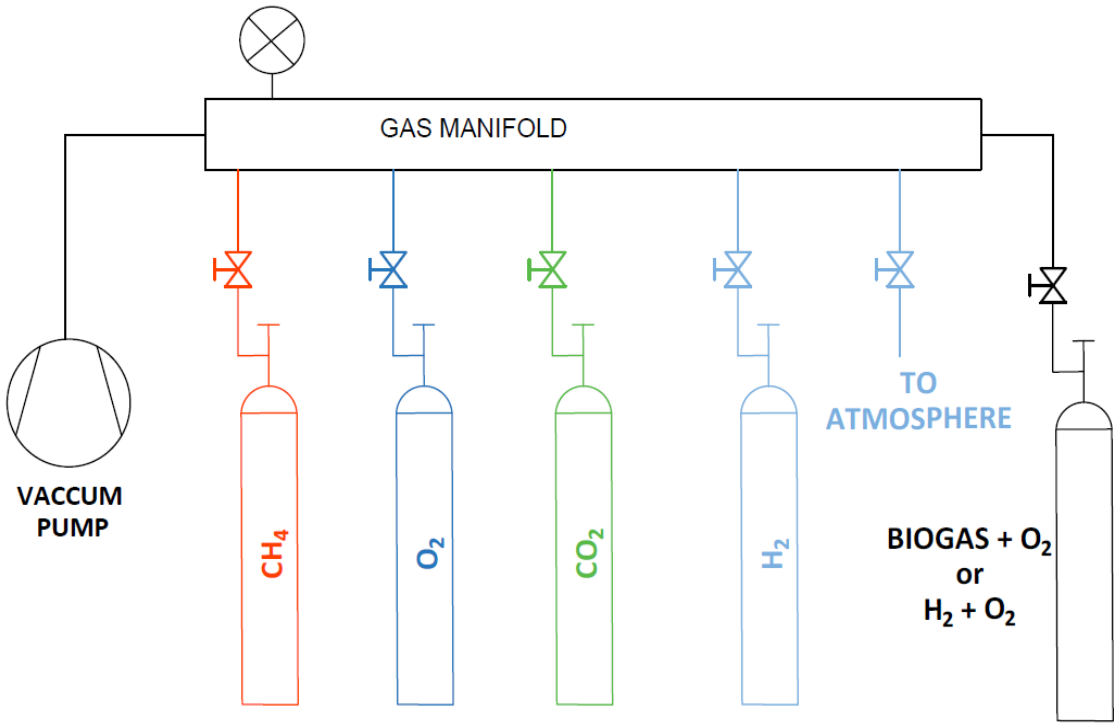


**Figure 22** Mixture preparation stand schematic

## 4.2. The experimental procedure

The experimental procedure was as follows. As the first step, the foil membranes separating initializing mixture from tested mixture and tested mixture from the dumping section were replaced. Next, a smoked foil was prepared by covering a 0.5 mm thick aluminum sheet with soot using an oil lamp burning a mixture of paraffine oil and toluene. When the foil was

thickly covered with soot it was then inserted into the test section and the whole tube was evacuated using the vacuum pump. After that, the driven and test sections were filled with biogas – oxygen mixture to the desired initial pressure and left for few minutes to stabilize. Finally, the driver section was filled with the hydrogen – oxygen mixture and the experiment was run. After the detonation took place, the combustion gases were evacuated and the tube was opened to remove the foil with the recorded cellular structure of the detonation. In the Figure 23 pictures documenting the process of replacing a membrane separating $H_2$ – $O_2$ and biogas – O2 mixtures, as well as preparing and inserting the smoked foil into the test section, are presented. The process of collecting the cell size measurements is described in the following section.

**a)**

**b)**

**c)**

**d)**


**Figure 23** Selected steps of the experimental procedure: a) replacing the membrane separating H2 – O2 and biogas – O2 mixtures; b) covering the foil with soot; c) smoked foil before the experiment; d) inserting the foil into the test section

## 4.3. Measuring the detonation cell size

The cell measurements collection was done in three steps. Firstly, after an experiment was conducted the foil with recorded cells was carefully removed from the tube and photographed using the camera at a resolution of 25 megapixels. In order to ensure that the photos were always taken from the same distance and perspective and as such to minimize the parallax error a special frame was used. It held the camera in a fixed position relative to the foil. Additionally, a paper scale was positioned inside the frame while taking the pictures. The next step was to load the photographs into the AutoCAD software and mark the widths of all recognizable and visible cells with line segments. Figure 24a-c presents examples of different cell sizes and cellular structures encountered during the experiments. In the Figure 24d triple points trajectories and one exemplary cell width are marked. Finally, the lengths of those segments were exported to csv file, loaded into a Python environment and scaled using the reading from the aforementioned paper scale. This method allowed to obtain between a dozen and a few hundred cell size readings, depending on the size of the cells and their visibility. It also has an advantage over traditional method of measuring a detonation cell size by hand with calipers in that the latter usually produces between 10 to 30 readings. The main limitation while taking the measurements by hand is the time constraint. While it is entirely possible to measure over 100 cell sizes by hand it would take a lot of time, ultimately slowing down the research.

At some point, it also becomes increasingly harder when the cells are very small. In such a case, not only measuring them is hard but also the process becomes more and more error prone as the calipers might slip on the foil. What is more, the smaller the cell size the bigger the relative error becomes when a researcher makes a mistake in positioning the ends of the calipers. For example, if an average cell size is 20 mm a mistake of 1 mm while taking the measurement makes for only 5% error, while for an average cell size of 5mm it becomes 20%. On the other hand, when the measurements are done in a software using a high resolution digital image, it is a lot easier to position the end of line segment precisely at the edges of a cell size. What is more, the image can be zoom in and out at will making the process faster, easier and more reliable. An added advantage is that results gathered in a digital form are easily storable and shareable. Additionally, they can be also easily re-examined if there is a suspicion that an error was made. Using the data gathered in that way a detonation cell size distribution for each tested case can be constructed. This in turn allowed calculating mean, standard deviation and other descriptive statistics of the gathered samples. Schumaker et al. [126] presented similar approach in their recent study on methane – oxygen detonation characteristics. Due to cell irregularity they conducted measurements at many locations across the foil and reported both average and standard deviation of those measurements. In the research presented in this thesis even more detailed statistical description of the experimental results is provided.

In the literature, one can find various methods of measuring the detonation cell size. On of the most popular method is to identify the collection of well-defined, easily visible cells over the entire foil, measure them and calculate the mean of the results [127]. The second most popular method is the ‘dominant mode’ method, as described by Diakow et al. [127]. The focus in it is put on prominent, long, continuous triple-point trajectories visible as continuous traces creating the boundaries of the cells. While taking measurements for the presented work a mixture of both methods was used, with an emphasis on the ‘dominant mode’. Wherever possible, triple-point trajectories were identified and traced which guided the process of marking the cell widths. In the Figure 24d an example of such traces, marked with white, dashed lines is presented. Additionally, the width (cell size) of one of the cells is marked and the direction of the detonation propagation is showed as well. It is worth noting that the trajectories of the triple-points are not marked using straight lines, nor they create a stable, repetitive structure, as it is sometimes showed in the literature on simplified images. In this case those trajectories are marked exactly as they were on the foil.

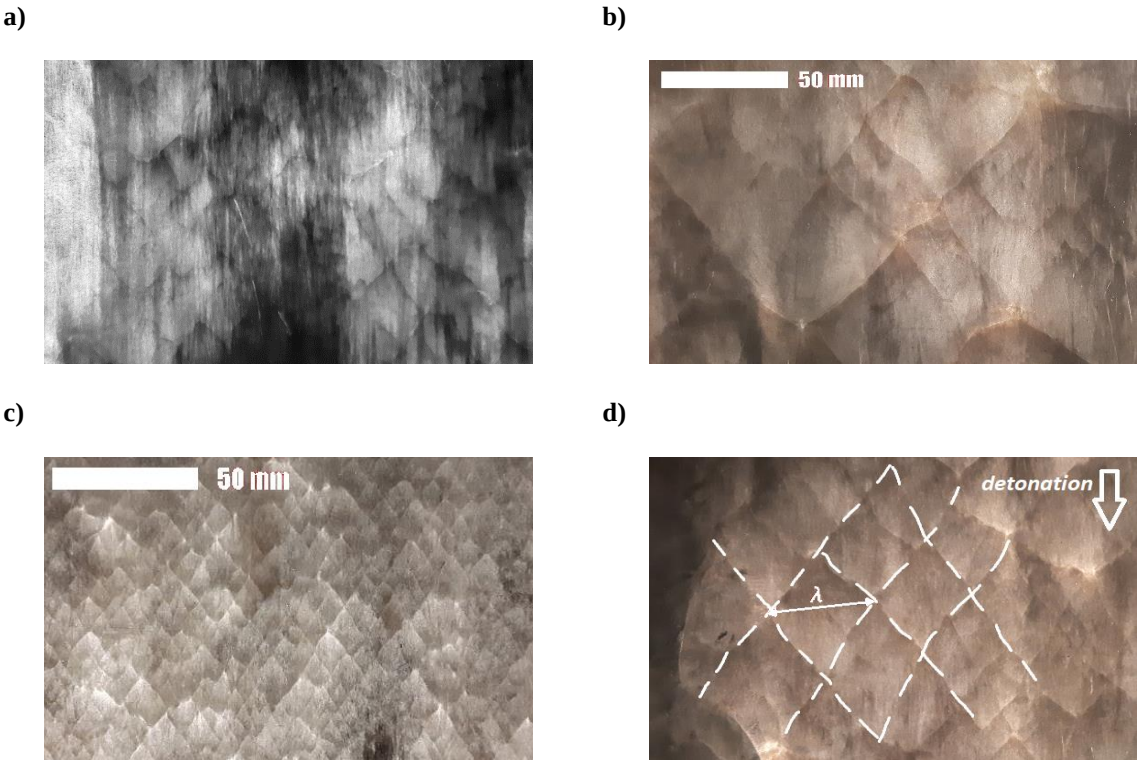


**Figure 24** Examples of recorded cellular structure during experiments: a) partially blown out soot; b) low Φ, $p_0$ and $CH_4$ content resulting in big cells; c) very small cells obtained from high $CH_4$ content and high $p_0$; d) an example of marked triple-point trajectories and detonation cell size.

## 4.4. Experimental uncertainty sources

An experimental research is always a subject to potential errors deriving from different sources. In the case of the research presented in this thesis three main sources of those errors were as follows:

1. the process of preparation of the combustible mixtures using the partial pressure method;
2. determining the initial pressure of the biogas – oxygen mixture in the tube;
3. cell size measurements.

In the first and second process, the same type of pressure manometer was used – Keller LEO 2. As described above, it has an accuracy of ≤ 0.1% FS and a scale of 0 – 30 bar. This results in an absolute value of uncertainty equal to ±0.03 bar. This in turn translates into an uncertainty of the equivalence ratio of 2% resulting in $\Delta\phi$ ranging from ±0.01 for $\phi = 0.5$ to ±0.03 for mixture with $\phi = 1.5$.

It is hard to assess the influence of the third mentioned source of uncertainty (cell size measurement process) in terms of numbers due to its complicated nature. It consists of a number

of ‘smaller’ sources, one of the being a parallax error. However, as mentioned earlier, steps were taken to minimize this problem by using a special frame that ensured a fixed position of the camera relative to the foil while taking the picture. Another problem, was the process of marking the detonation cell widths in the software. As can be seen in the Figure 23 above, the detonation cellular structure was very unstable resulting in a wide variety of traces left on the foil. Sometimes the soot was partially blown out so that it was hard to spot and trace the triple-points trajectories and as such to mark the widths of the cells. What is more, in some cases a secondary cellular structure appeared which added, yet another layer of complexity to the task. Those unstable cellular structures observed during the experimental campaign resembled those presented by Ng [108] and Pintgen [128] and can also by treated as a source of uncertainty introduced into the process of marking the cell sizes.

## 4.5. The experiments of different biogas composition mixtures with oxygen detonations

In the experimental part of the presented work a number of experiments was conducted. Those experiments included different combinations of, aforementioned, initial pressure, equivalence ratio and methane concentration. As mentioned above, for the cases up to 50% of methane content the experiments were conducted for the full range of initial pressure (0.6 ÷ 1.6 bar) and equivalence ratio (0.5 ÷ 1.5). In case of the 45-55 and 40-60 mixtures, the experiments were also only for $\phi = 1$ for most of the initial pressures. The reason for that is that although the experiments were conducted the foil was destroyed every time. During the talks with more experienced researchers two hypotheses were made. First was that it was due to the flame extinction after passing from the $H_2 – O_2$ into the biogas – $O_2$ mixture and then being reinitiated and transitioned into a detonation by a shock wave reflected from the end of the tube. Such a detonation would then propagate in a pre-compressed mixture with much higher initial pressure and as such would be much stronger capable of destroying the thin foil. The second hypothesis was that after passing through the membrane separating the two mixtures the flame decoupled from the shock wave and slowed down as it propagated as a deflagration. In such conditions the foil would be exposed to high temperature of the flame front for much longer than in case of a detonation and as such would be destroyed by it. Nevertheless, as it was impossible to verify those hypotheses without altering the test stand and because it was not the main focus of the work, this topic was not investigated any further. It is also worth noting that the destruction

of the foil might have been also caused by wrong mounting of the foil inside the tube. If a part of the foil did not align with the tube wall a shockwave could go between the foil and tube wall causing the destruction of the former.

The goal of the experimental part of the work was to first gather the cell size measurements for different combinations of the initial mixture parameters. The influence of each of the parameter on the cell size was tested and described. This data was then used, in the second part of the work, to train and validate a machine learning model. That model allows to predict the cell size for mixtures with combinations of initial parameters that were not tested. It will be described in full details in the section 5 of this dissertation. The secondary goal of the experiments was to enable a detailed statistical description of the cell size distributions. In the literature, usually only an average value of a measured cell size is reported, which is not enough, especially in cases where the cellular structure of the detonation is very unstable. Fortunately, nowadays researchers more often report also a calculated variance or standard deviation of the measured cell sizes. In the author's opinion those two values - variance and mean should be a bare minimum, mandatory when reporting any kind of measurements of a value that is believed to follow a normal distribution. In this thesis, an even more comprehensive and detailed description is provided as the author believe that it is of vital importance for modern science to take into consideration not only an average value but the whole distribution.

This section is structured as follows, first in subsection 4.5.1. an analysis of calculated from experimental data detonation velocities compared to theoretical Chapman – Jouguet detonation velocity is presented. Next, in the subsections 4.5.2 ÷ 4.5.4. the influence of each of the three mixture's initial parameters on the detonation cell size is described. In the sections 4.5.5. and 4.5.6. results of additional calculations of an induction length and instability parameter $\chi$ and their correlations with cell size are presented. Finally, the aforementioned, comprehensive statistical description and distribution analysis is presented in the subsection 4.5.7. The section is then closed by a brief summary of the presented work before moving to the second part of the dissertation.

### 4.5.1. Detonation velocity analysis

First thing that was done, before analyzing the rest of the results, was to compare the detonation velocities from the experiments ($V_{exp.\ det.}$) to the theoretical Chapman – Jouguet detonation velocities obtained using the NASA CEA software [96]. This was done to ascertain that the detonation was stable. The experimental detonation velocity was calculated using the

time difference of arrivals of the wave at the position of two consecutive pressure sensors and the known distance between those sensor (as seen in the Figure 17). In order to ascertain that the detonation has sufficient time to stabilize after passing $H_2 – O_2$ mixture into biogas $– O_2$ mixture, only the velocities between sensors P4 ÷ P7 were calculated and then averaged. Figure 25 presents the comparison of the calculated velocities on Y-axis and theoretical values on X-axis. The methane concentration in a biogas is denoted by a color of the dot while the subplots presents the results for a given equivalence ratio. The initial pressure is not shown directly however, from the analysis it was confirmed that, for every case, the higher the initial pressure the higher the velocity. This is clearly visible as in every methane content group of points there is a clear trend towards the higher velocities that is caused by the increasing initial pressure. The diagonal solid line is the theoretical line of a perfect agreement of a theoretical and calculated velocities ($V_{exp.\ det.} = V_{CJ}$). The dashed lines around it presents a ±2% deviation boundary. It can be seen that a vast majority of the points fall withing those boundaries, showing very good agreement with theory which shows that in all experiments the detonation was stable. It is also clear that except for, aforementioned relationship between the detonation velocity and the initial pressure, the latter also increases with the increasing equivalence ratio as well as $CH_4$ percentage, ranging from around 1820 m/s for the low initial pressure 50-50 mixture, up to almost 2300 m/s for the 70-30 mixture with high initial pressure. In case of the relationship with $CH_4$ this can be seen by observing the position of unicolor groups of points. At the same time, in case of the equivalence ratio, as all subplots have the same scale on both axes, one can observe that all the groups move up along the solid line as the equivalence ratio is increased.

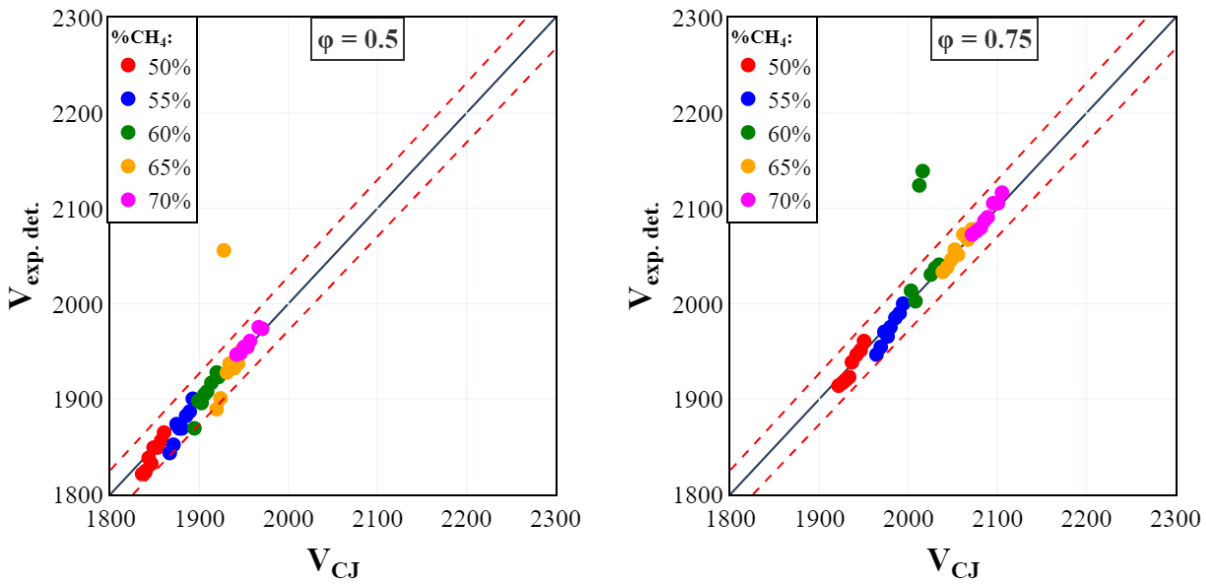

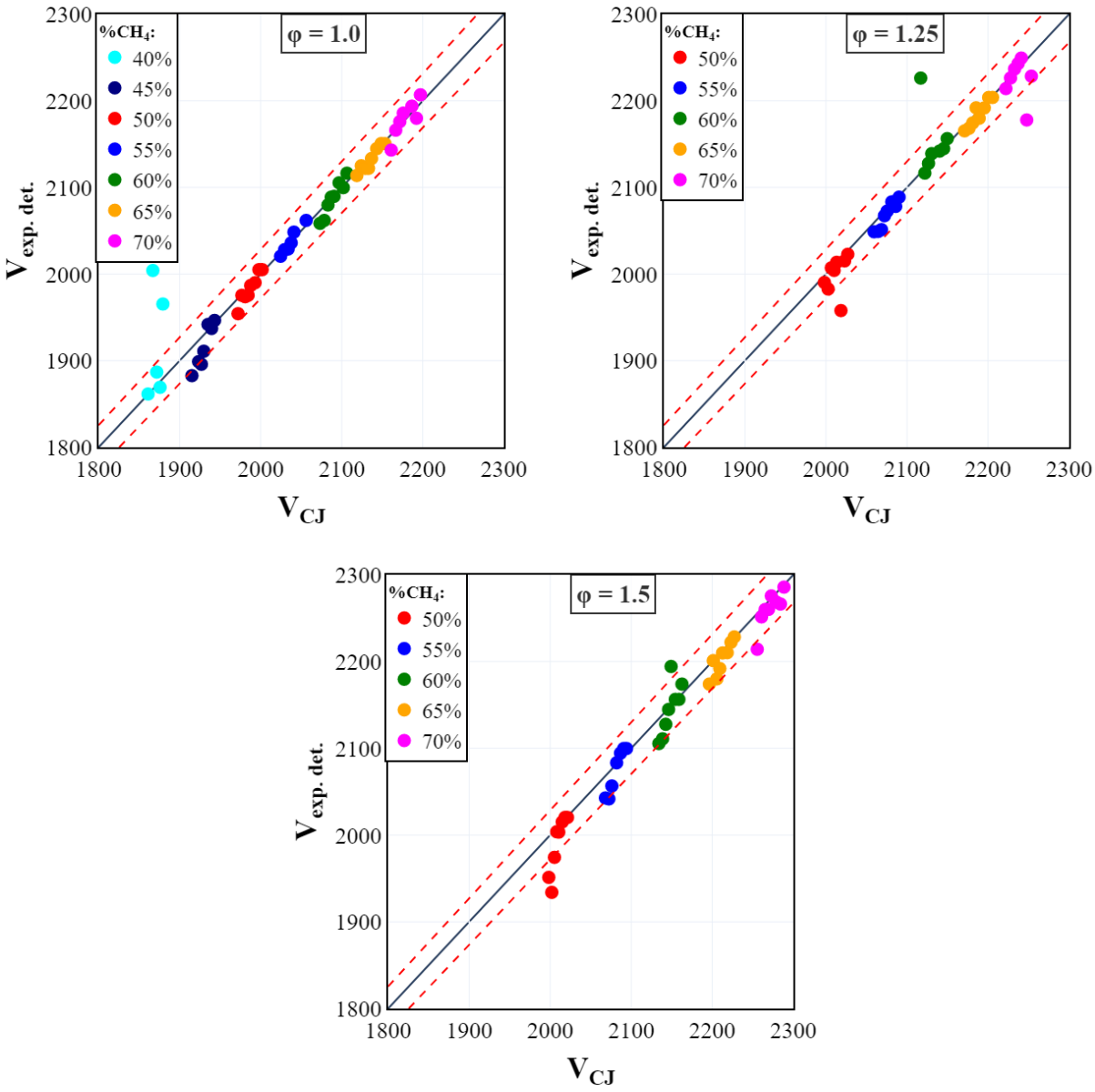


**Figure 25** Calculated experimental detonation velocity cs theoretical Chapman - Jouguet detonation velocity, grouped by CH4 content and equivalence ratio. The dashed lines show a ±2% boundary around ideal agreement line ($V_{exp.\ det} = V_{CJ}$).

### 4.5.2. Influence of the initial pressure $p_0$ on the cell size

In the Figure 26, average cell size plotted against mixture's initial pressure is presented. Each of the subplots presents results for a given equivalence ratio while methane content is denoted by color. Both X-axis and Y-axis in every sub plot have logarithmic scales and the same limits, in order to make comparing the subplots easier. The error bars are not shown neither on this plot nor on the subsequent ones because, due to a high number of cases, they would render the plots unreadable. Instead, a comprehensive statistical description and analysis is provided in the subsection 4.5.6. The solid lines present fitted trend lines described by the following equation: $\ln(\lambda) = A*\ln(p_0) + B$. The coefficient of determination $R^2$ for those trend

lines falls between 0.93 and 1. Due to the high number of cases the specific values of coefficients A and B for the each of the fitted trend line are provided in the Appendix A at the end of this thesis.

It can be seen that average cell size ranges from around 5 mm at the minimum up to 53 mm at the maximum and it depends on all the tested parameters: $\phi$, $p_0$ and $CH_4$ content. It is clear that the cell size is inversely proportional to the mixture's initial pressure $p_0$, providing that both $\phi$ and $CH_4$ percentage are held fixed while changing the $p_0$. The higher the pressure the smaller the smaller the resulting cell size. As mentioned above, for the presented data the relationship between cell size and initial pressure is logarithmic in nature. However, it is important to note that this is true only for the tested and presented range of values, outside of it, it cannot be guarantee that the same relationship holds. What is more, while analyzing the data different equation types for the fitted lines were tested and $\lambda \sim 1/p_0$ also proved to fit well, but nevertheless $\ln(\lambda) \sim \ln(p_0)$ yielded slightly better results. Both relationships were encountered in the literature and as such it is important to highlight the fact that the one presented in the plot holds only for that range and will not guarantee good results outside of it. This is true for every kind of fitted trend lines, they should not be blindly trusted outside of the data range for which they were defined.

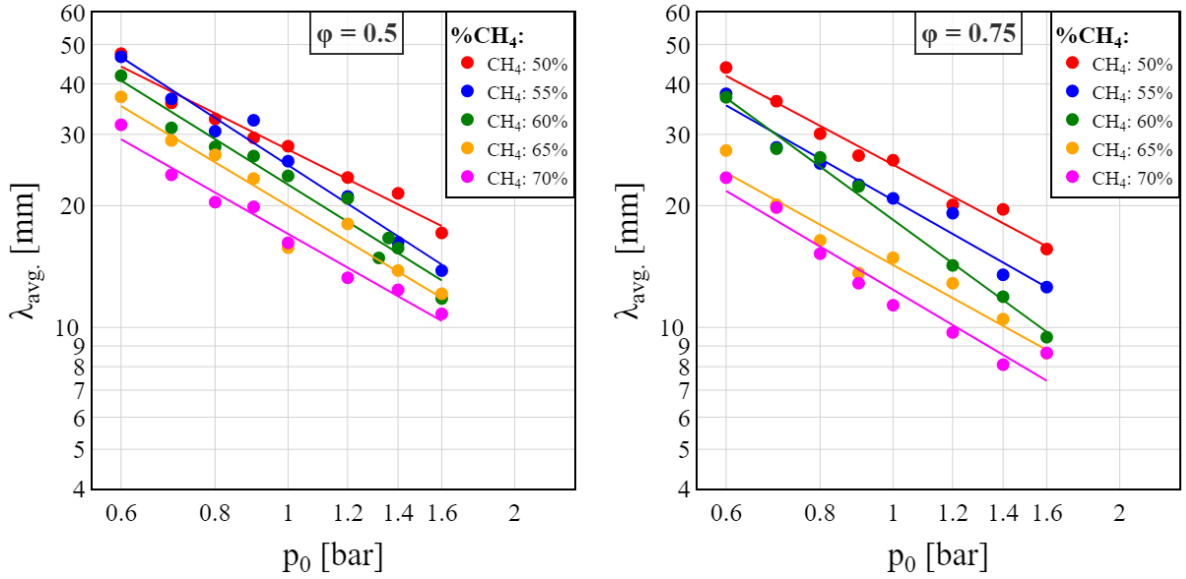

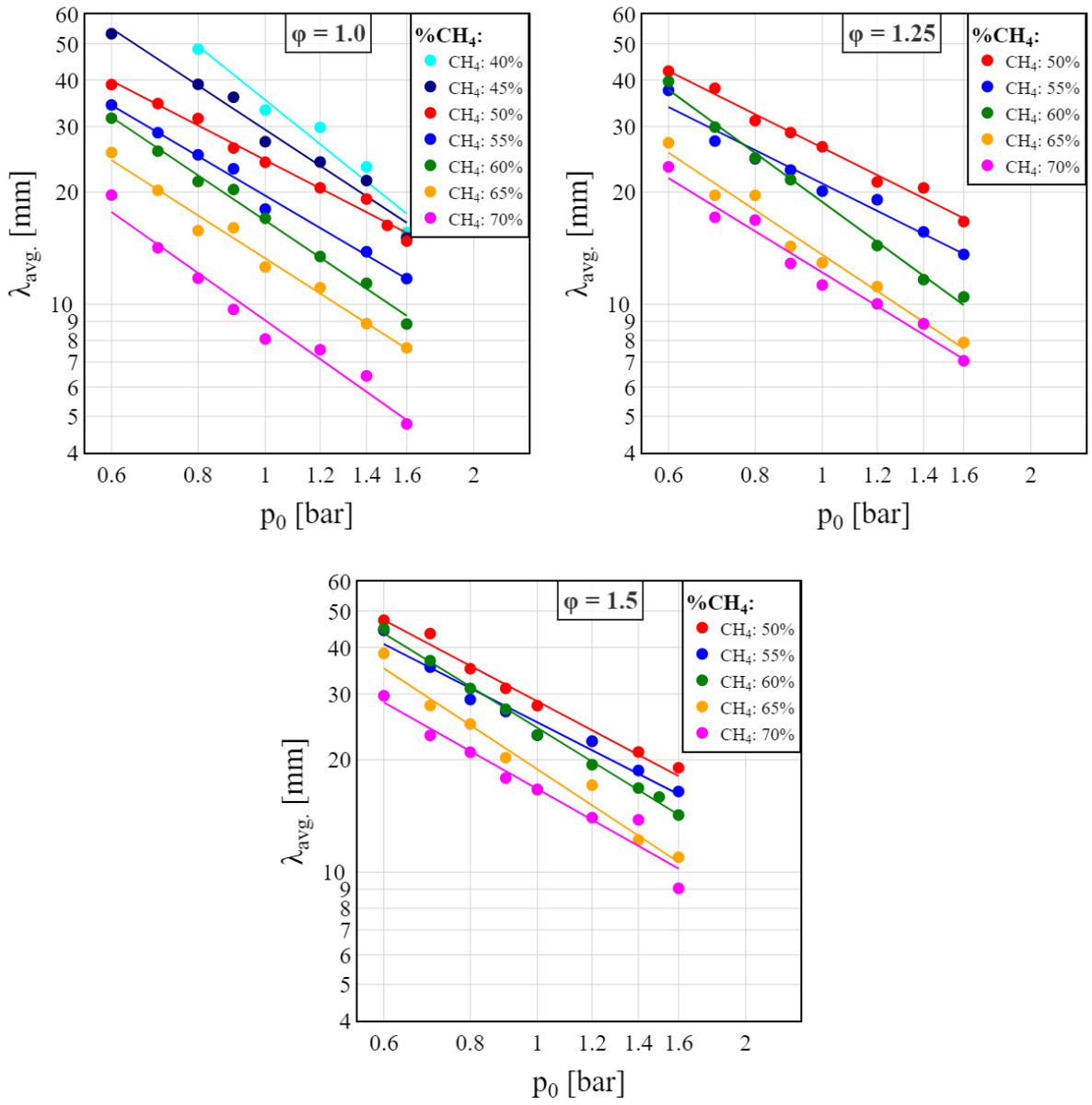


**Figure 26** The cell size as a function of mixture's initial pressure $p_0$. The color denotes the $CH_4$ content while the sublots correspond to different equivalence ratios ϕ. The scales on both axes are logarithmic.

### 4.5.3. Influence of the equivalence ratio ϕ on the cell size

Figure 27 below presents the relationship between average cell size and equivalence ratio when $CH_4$ percentage and initial pressure $p_0$ are held constant. The colors show the level of methane content while the subplots present the value of initial pressure for which the results were achieved. In contrast to the Figure 26, neither Y-axis nor X-axis has a logarithmic scale. On the other hand, similarly to Figure 26, the solid curves present fitter trend lines described by a quadratic equation in the following form: $\lambda = A + B*\phi + C*\phi^2$. The values of the coefficients A, B and C are also included in the Appendix A. The coefficient of determination $R^2$ falls between 0.8 and 1, showing a good fit. Not all cases has enough points to fit the trend curve. As mentioned above, the mixtures with methane content below 50% were not tested in

the full range of pressures and equivalence ratios. This can be seen in the presented plots as the data points for mixtures 40-60 and 45-65 are present only for some initial pressures and always for only $\phi = 1$. In order to ease the comparison all subplots have the same scales.

As can be seen, the cell size approaches minimum when the equivalence ratio approaches unity, and increases when the equivalence ratio moves away from 1. This is in general agreement with the data that can be found in the detonation database [102]. However, it is important to note that some researchers suggest that the minimum is not achieved at stoichiometry but at a value of $\phi$ slightly higher than 1. This was not confirmed in the presented research but the next value of tested $\phi$ is 1.25 so it is possible that the minimal value would be achieved somewhere in between. It is also important to note, that this reasoning is based on the studies conducted for different mixtures as there is almost no data for biogas – oxygen/air detonation cell sizes. As such it is hard to draw final conclusion as to whether the minimal cell size value is achieved for $\phi = 1$ or not, but it was also not the goal of this research. As mentioned above, in the Figure 27 the fitted lines are second degree polynomials. Nevertheless, it should be noted that although for the presented data it proved to be the best fit, the literature suggests that if a wider range of equivalence ratio was to be taken into account the quadratic equation could turn out to not be the best fit. This is because for different mixtures the fitted curve usually is not ideally symmetrical around the minimum in a way that a parabola is. Nonetheless, a quadratic equation was the best fit for the obtained data and as such, it is presented below.

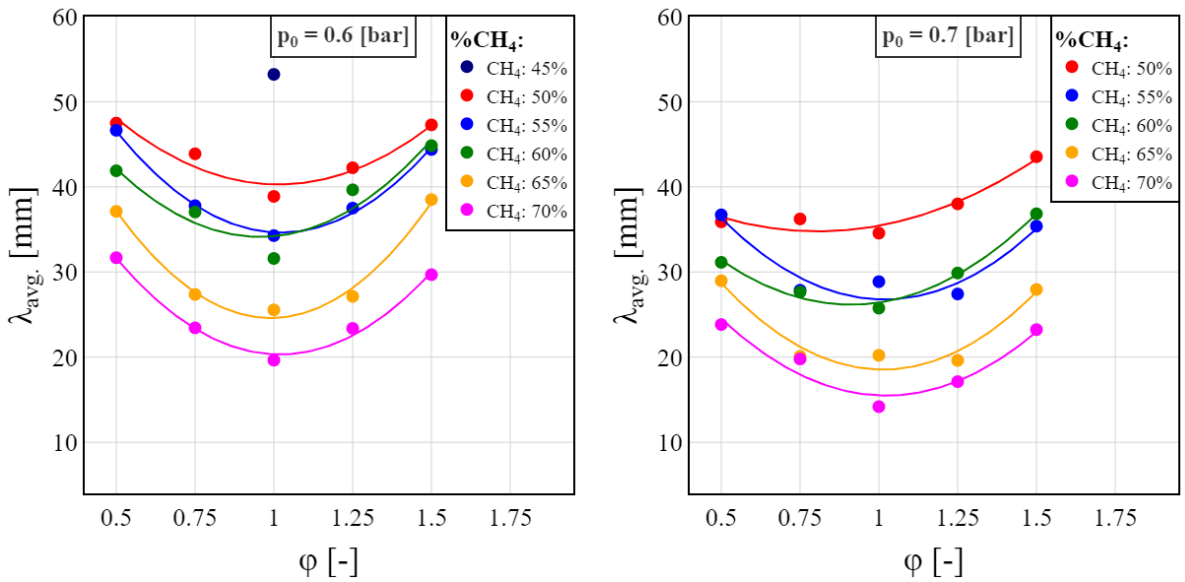

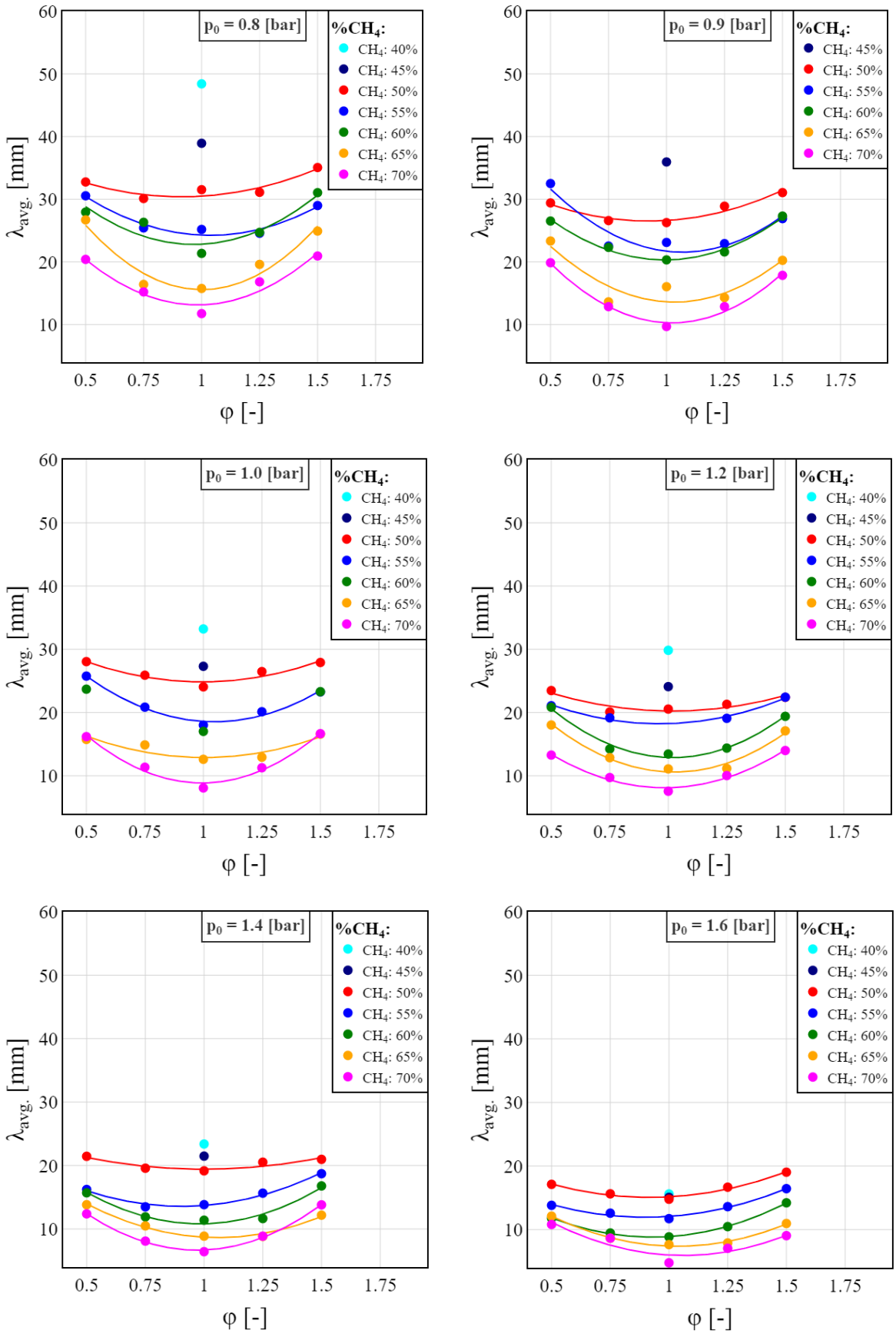


**Figure 27** The cell size as a function of mixture's equivalence ratio ϕ. The color denotes the $CH_4$ content while the sublots correspond to values of the initial pressure $p_0$.

### 4.5.4. Influence of the $CH_4$ content on the cell size

Figure 28 presents the dependency between average detonation cell size and methane content in a biogas. The same as in previous subsections, each of the subplots shows the results for different equivalence ratio while the colors correspond to different initial pressures. The scales on both X and Y axes are kept constant in order to help with comparison of the plots. The solid lines are trend lines described by the following equation: $\lambda = A*(\%CH_4) + B$. The coefficient of determination $R^2$ ranges from 0.81 up to 1 showing a very good fit. The values of A, B and $R^2$ for every fitted line are provided in the Appendix A.

From the presented plots it can be concluded that the relationship between the average cell size and the methane concentration is linear. The higher the methane content in the fuel mix, the smaller the resulting detonation cells are. The $CO_2$ present in the biogas acts as a diluent effectively lowering the detonability of the mixture and increasing the cells.

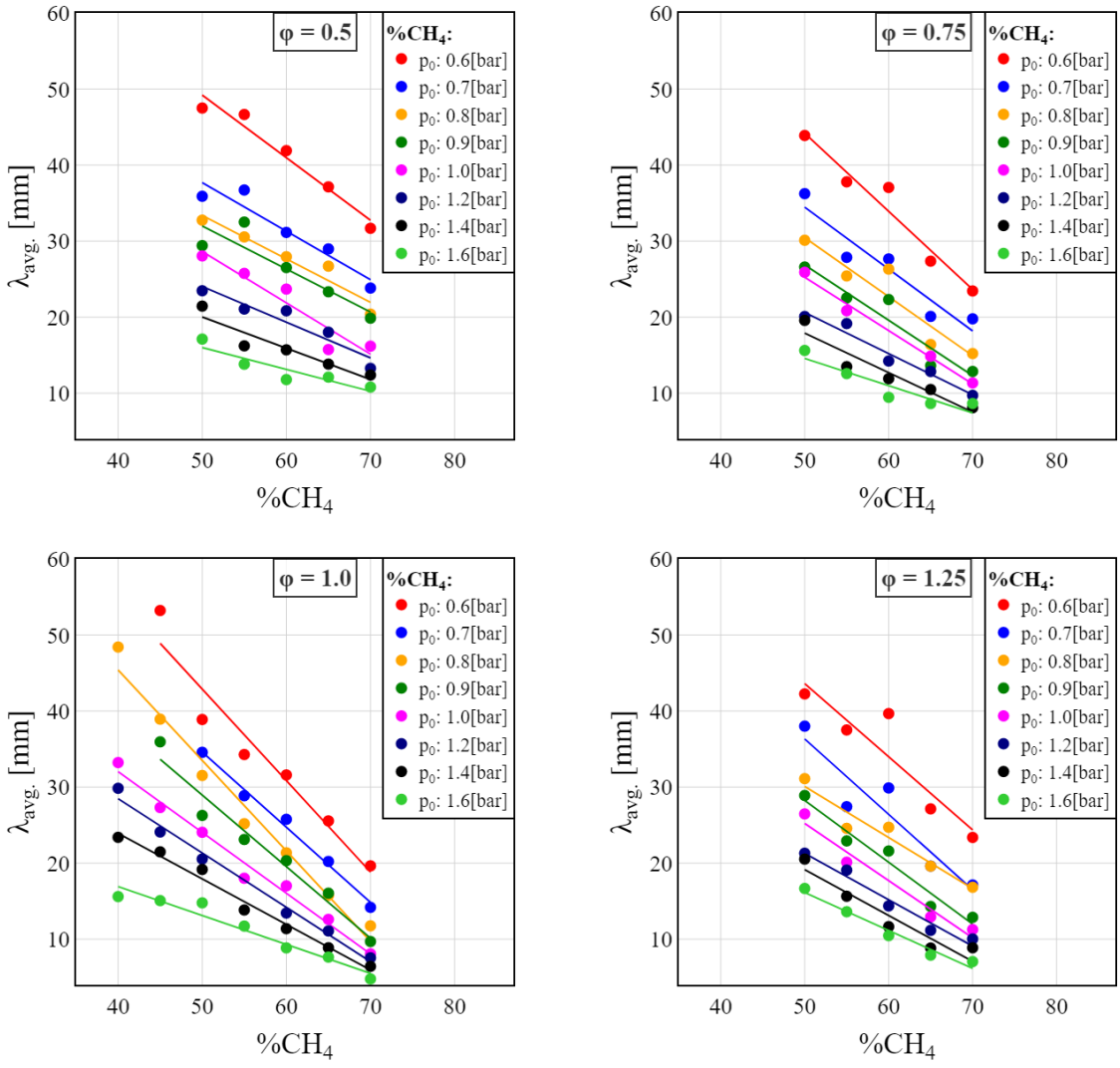

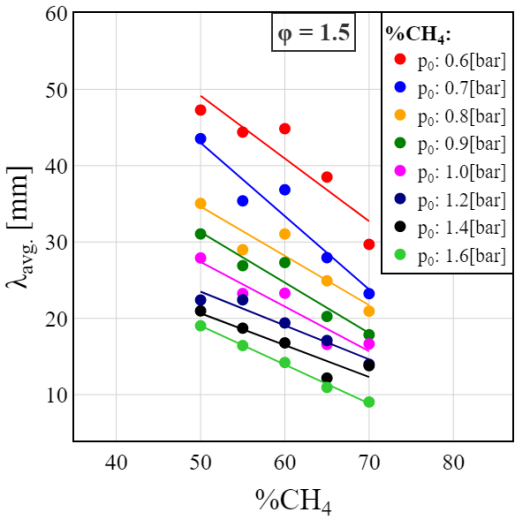


**Figure 28** The cell size as a function of methane content. The color denotes the mixture's initial pressure $p_0$ while the sublots correspond to different equivalence ratios $\phi$.

### 4.5.5. Induction length correlation with the detonation cell size

In addition to the experimental results the ZND induction length $\Delta_i$ and instability parameter $\chi$ (presented in the next subsection) were calculated. The calculations were performed using the San Diego kinetics mechanism [129] with the Cantera [104] and SDToolbox software [130]. It is very important to be aware of the mechanism that was used because the results are very sensitive to that choice and as such care should be taken when comparing the results across different studies.

Figure 29 presents the average sell size $\lambda_{avg.}$ plotted against the ZND induction length $\Delta_i$. The subplots show the data for different equivalence ratios $\phi$ with different methane percentages shown in different colors. Solid lines are fitted trend lines described by the following equation: $\lambda \sim A^* \Delta_i + B$. The color of the fitted trend line corresponds with respective methane content in biogas. The values of coefficients A and B as well as $R^2$ are presented in the Appendix D. It can be clearly seen that there is linear relationship between cell size and induction length, which is in agreement with previous research [126, 131]. This is additionally confirmed by a very high values of the coefficient of determination $R^2$ that ranges from 92% up to 99.5%. Furthermore, for a given methane percentage and equivalence ratio, induction length is inversely proportional to the initial pressure. The higher the pressure, the lower the induction length. In each series of points corresponding to a chosen methane content the colors corresponding to the higher pressures are always on the side of low cell size and induction length. On the other hand, those corresponding to the lower pressures are always on the side of high cell size and induction length.

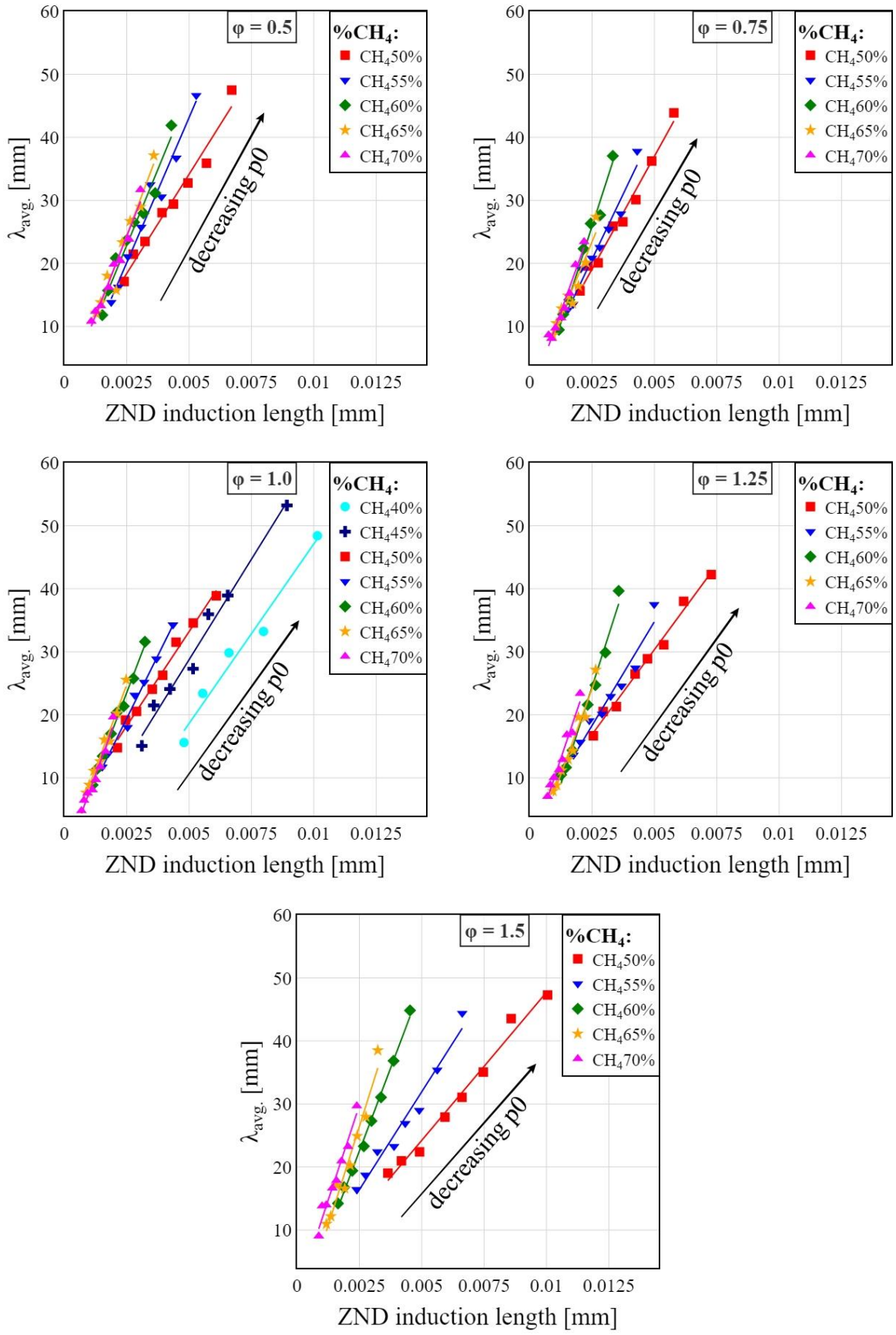


**Figure 29** Average cell size plotted against ZND induction length. Subplots present the results of calculations for different ϕ, symbols and color scales correspond to CH4 content and initial pressure, respectively.

### 4.5.6. Stability parameter χ analysis

Aside from the ZND induction length, a stability parameter χ was also calculated using the same kinetics mechanism. There are two definitions of that parameter that can be found in the literature. One was introduced by Radulescu et al. [132] while the other by Ng et al. [107], in this thesis the latter was used. The instability parameter χ is then defined as the activation energy for the induction process $\varepsilon_I$ multiplied by the ratio of the induction length $\Delta_i$ to the reaction length $\Delta_R$.

$$\chi \equiv \varepsilon_i * \frac{\Delta_i}{\Delta_r} = \epsilon_i * \Delta_i * \frac{\dot{\sigma}_{max}}{u_{CJ}} \tag{13}$$

The reaction length is defined as the inverse of maximum thermicity ($1/\dot{\sigma}_{max}$) multiplied by $u_{CJ}$ that is the particle velocity at the CJ plane in shock-fixed coordinates. It is important to note that when comparing the results across different studies, except for the definition of the parameter, one must also pay attention to the kinetics mechanism used for the calculations.

Figure 30 shows the stability curve introduced by Ng et al. [107] as well as the calculated values of the stability parameter for different mixtures. The initial conditions of those mixtures were as follows, $T_0$ = 298 K, $p_0$ = 0.2 atm. In their work, the authors concluded that the $CH_4 + 2O_2$ and $C_3H_8 + 5O_2$ mixtures had a highly irregular structure, with $C_2H_2 + 2.5O_2$ having irregular structure and the rest having regular or even highly regular, for those slightly above and below the curve, respectively. It is important to keep in mind that the Y-axis is logarithmic making the differences look smaller than they, in reality, are.

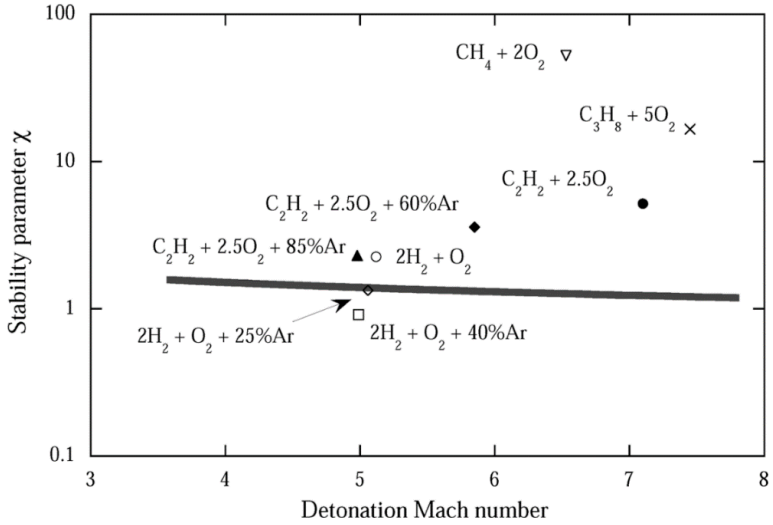


**Figure 30** Stability parameter calculations and the stability curve as a function of $M_{CJ}$ [107].

Figure 30 presents the results of the stability parameter calculations for the cases presented in this dissertation. The parameter χ is plotted against the initial pressure $p_0$, with the

subplots presenting different ϕ and colors different methane percentages. The solid lines are fitted trendlines described by the following equation: $\ln(\chi) = A*\ln(p_0) + B$. The values of A, B

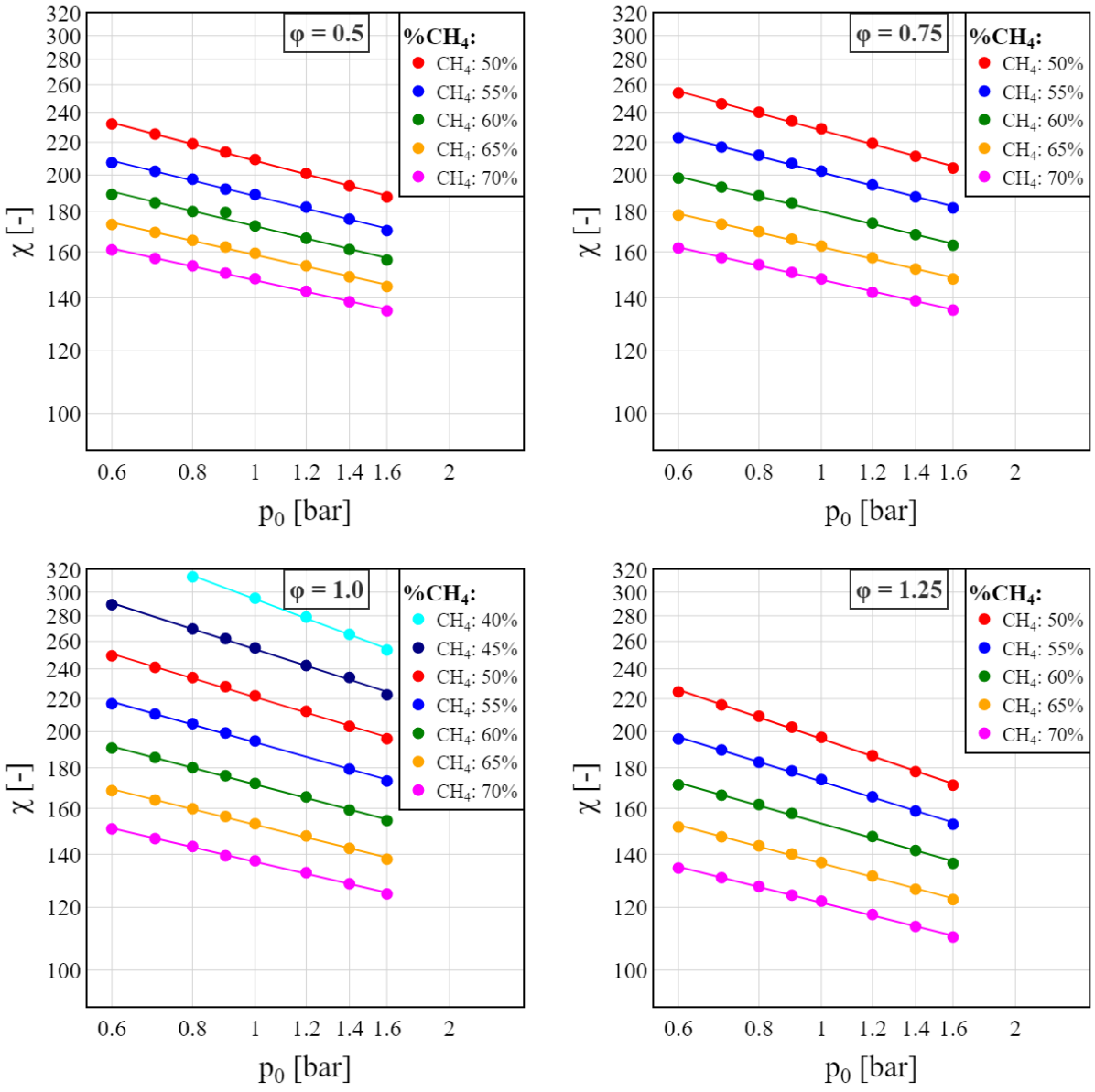

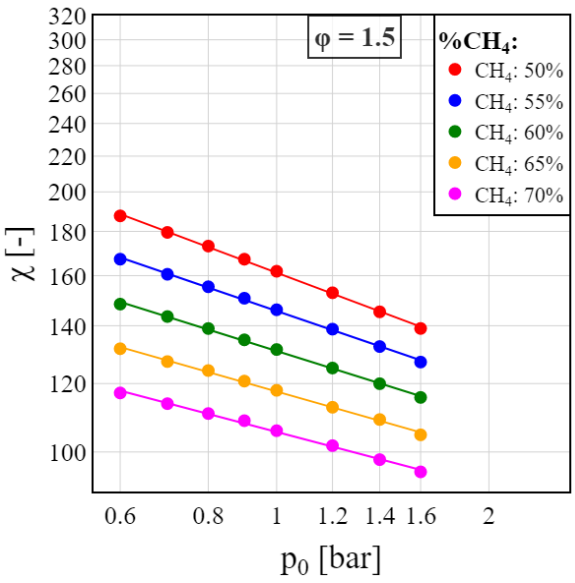


**Figure 31** The stability parameter χ plotted against the initial pressure p0, grouped by the equivalence ratio ϕ and methane percentage.

and $R^2$ are presented in the Appendix E. By comparing the stability curve in the Figure 29 with the numbers shown in the Figure 30, it is immediately evident that the latter lay well above the stability curve. As such, it can be concluded that the tested biogas – oxygen mixtures have a highly irregular structure. This is in agreement with what was observed visually while taking the measurements. What is more, one can also see that the correlation between χ and $p_0$ is logarithmic in nature. Additionally, the χ decreases not only with the increasing initial pressure but also with increasing methane content in a biogas. It is then evident that the CO2 acts as diluent that not only increases the cell size but also the stability parameter, making the structure even more irregular. In case of the equivalence ratio ϕ the relationship with χ is not that monotonic, as going from 0.5 to 0.75 the χ increases and only after passing that value the stability parameter keeps decreasing with the increasing ϕ.

### 4.5.7. Statistical description and cell size distribution analysis

In this subsection a more in-depth view on the data set gathered from the experiments is provided. The distribution of number of measurements gathered for each case, a standard error of the mean and the variation of the results and a way to meaningfully compare them is discussed as well. The purpose of this is to provide a better understanding of the entire dataset of the gathered cell size measurements. This is in contrast to the previous subsections in which the focus was solely on the average cell size and its correlation with the initial parameters. Below, the most interesting finding are described, while in the appendix F a very comprehensive, statistical description of the measurements is provided.

***Measurements counts***

Figure 32 presents the distribution of number of cell size measurements taken for each of the researched cases. The data is shown in two ways, as a boxplot and a histogram, in the top and bottom part, respectively. A boxplot presents the data, as the name suggests, in a form of a box with, so called, whiskers (it's also called box and whiskers plot for that reason). The box shows the interquartile range (IQR), namely the data points between 1$^{st}$ (Q1) and 3$^{rd}$ quartile (Q3), or equivalently 25$^{th}$ and 75$^{th}$ percentile. The whiskers mark either the span of 1.5*IQR with dots marking the, so called, outliers or the maximum/minimum value of the datapoint, whichever is either higher (left whisker) or smaller (right whisker). Mathematically, the end of the left whisker is written as *max(minimum value; Q1 - 1.5*IQR)* and the end of the right whisker as *min(maximum value; Q3 + 1.5*IQR).* The vertical solid and dashed lines represent the sample's median and mean, respectively. A histogram is created, by dividing the entire range of values into a series of intervals, called 'bins'. The data points falling into each bin are then counted and the plot is created by showing the bins on one axis and the corresponding counts on the other. In Figure 32b those are X and Y axes, respectively. Additionally, the counts might be normalized by dividing them by the total count and presenting data in that form. This is shown in the plot in which, the normalized counts are presented on the Y-axis, showing the probability of getting a data point from a given interval by choosing randomly, the sum of those values is equal to one.

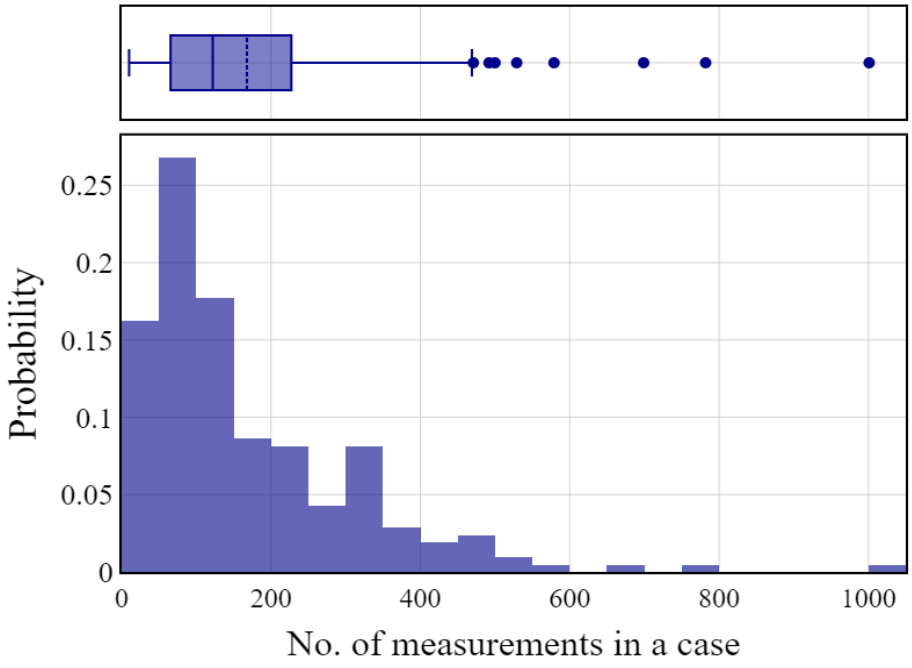


**Figure 32** The distribution of the number of measurements taken for every case, shown as boxplot (upper plot) and histogram (lower plot).

From the plots it can be seen that the range of numbers of measured cells for every case is wide, starting from around 10 and ending in over 1000 (precisely 1001). However, 75% of the data falls between 0 and around 225 data points with median and mean being 122 and 168, respectively. The total number of measured cells in all cases was 35096. The differences in number of measured cells was caused by a number of factors. First, due to the wide variety of the tested parameters, the cell sizes differed significantly ranging from around 3 mm all the way up to around 50 mm. Because of that, the number of measurements acquired from one foil differed significantly. On top of that, as mentioned above, the cellular structure of the cells was very irregular making it very hard or even sometimes impossible to correctly measure the cells. Finally, in some cases, either part of the soot or all of it was blown away from the foil, partially or completely destroying the results.

***Standard Error of the Mean***

Figure 33 presents the distribution of the standard error of the mean (SEM) obtained for the researched cases. Simply put, SEM is an estimate of how far the sample mean is likely to be from the population mean. In mathematical terms, the standard error of the mean is the standard deviation of the distribution of sample means [133]. The word 'sample' refers to the sample of a variable in question, in a presented case this is the detonation cell size. In other words, if one would repetitively take a sample of a given size from a distribution and calculated the mean of the sample, those means would form a normal distribution with the mean equal to the sampled distribution's mean and the standard deviation of that means distribution would be equal to the described standard error of the mean. A mathematical formula for SEM is:

$$SEM = \sigma_{\bar{x}} = \frac{\sigma}{\sqrt{n}} \approx \frac{s}{\sqrt{n}} \tag{14}$$

where σ is the distribution's standard deviation and n is the sample size. However, because the distribution's standard deviation is not known it is approximated by the sample's standard deviation – s.

Looking at the boxplot shown below, it is evident that for almost 75% of the researched cases the SEM was below 0.5 meaning that an average cell size was approximated very accurately. The mean and median values of the calculated SEMs were 0.43 and 0.31, respectively. For the rest of the points the spread is fairly big going from a little more than 0.5 all the way up to 3.5. This is mostly because of the low number of gathered measurements as from the equation (15) it is evident that the higher the sample size the lower the SEM is. This is additionally clearly backed up by the scatter plot shown in the Figure 33b. It presents the

SEM plotted against the sample size. The decreasing of SEM as the number of measurements increases is clearly visible, tending asymptotically to 0 as the sample size grows.

**a)**

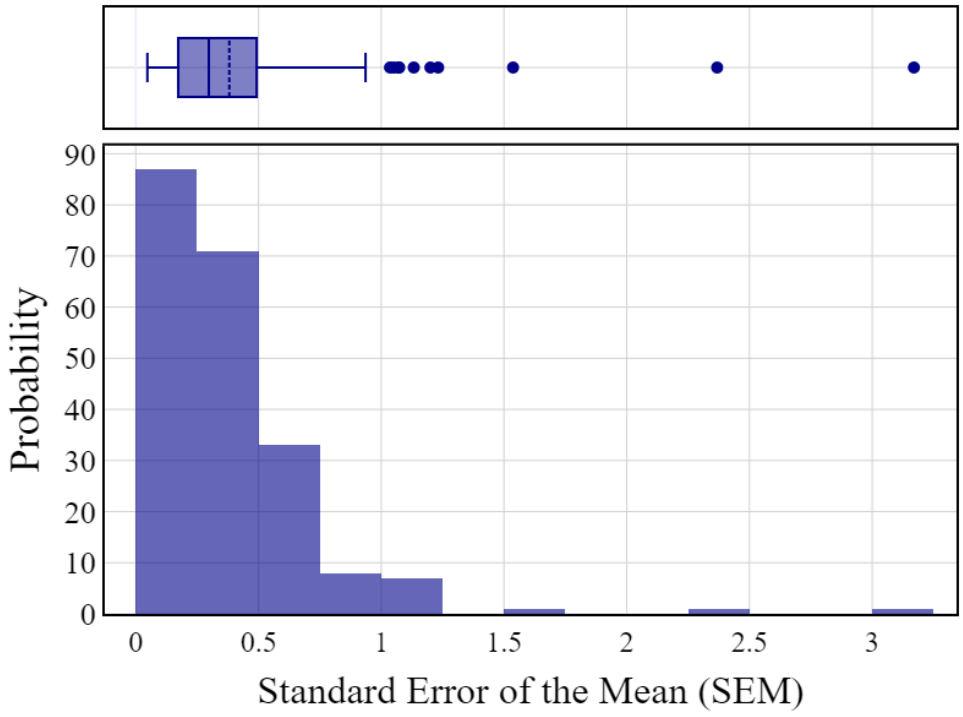


**b)**

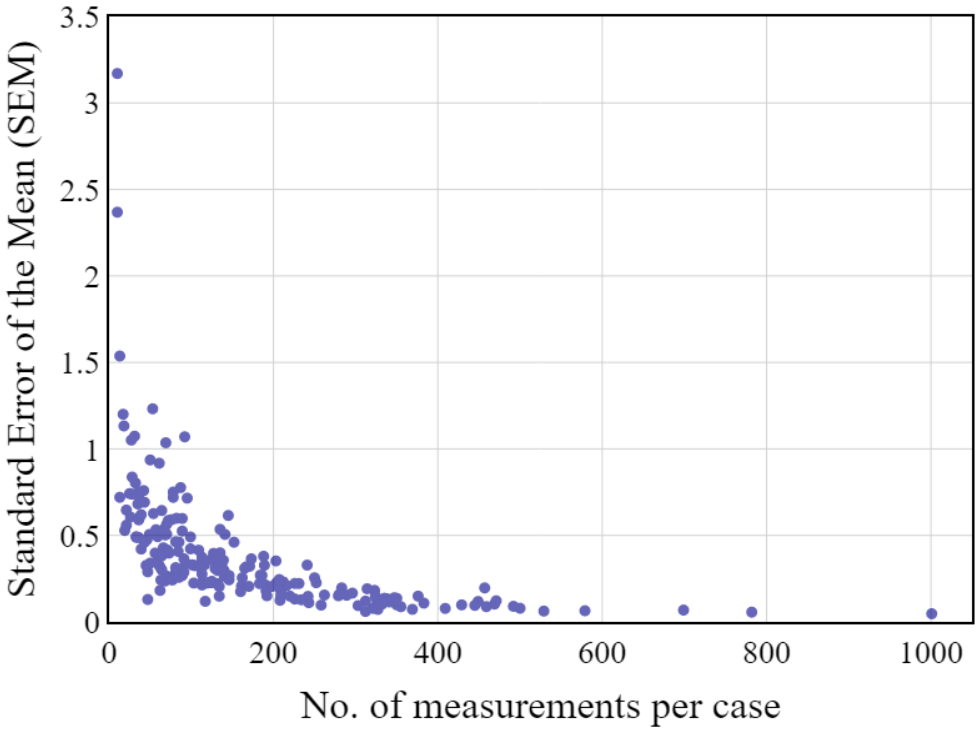


**Figure 33** a) The distribution of the Standard Error of the Mean (SEM) shown as a boxplot and a histogram; b) SEM plotted against the sample size.

***Coefficient of Variation***

Figure 34 shows the density distributions of the gathered cell size measurements for $\phi = 1$, three methane percentages and different initial pressures $p_0$. In order to keep the plot readable it was decided to only show selected cases, however the rest follow the same pattern. As described in the previous subsections, one can clearly see that with higher initial pressure and higher $CH_4$ content, the cell size decreases. However, the most important thing to notice is that as the cell size increases, the width of the distributions increases as well. This in turn, suggests that the variance of the measurements also increases. However, because the range of the cell sizes span from a few mm to almost 50 mm, depending on the mixture initial parameters, the variance cannot be directly compared between different cases. Instead, a coefficient of variation (CV) should be employed to allow comparisons of two distributions with different means. Coefficient of variation is a very useful metric as it shows the extend of variability in relation to the mean of the population. It is calculated by dividing the sample's standard deviation by its mean. In the described study, the variance increases together with the increasing cell size. However, there is no significant variation in the CV values that are centered around the value of 16% (mean) - 17% (median) with the standard deviation of 4%. This is shown in the Figure 35, it can be seen that over 75% of the cases had the relative variation lower than 20% and for only around 6% of the cases it is higher than 22.5%. Figure 36 presents the coefficient of variation plotted against the number of cell size measurements collected for every case. It is worth noting that it looks like the value of CV tends to some constant value as the sample size increases. This value is probably somewhere between 0.18 and 0.2. However, without further investigation it is not possible to determine this value with a high degree of probability. In order to help visualize it, the red and green lines denoting an average and median value of CV respectively, were added to the plot. Additionally, red, dashed curves showing a probable boundaries are also shown. However, it is important to note that they are shown to help visualize the point and are not formally calculated.

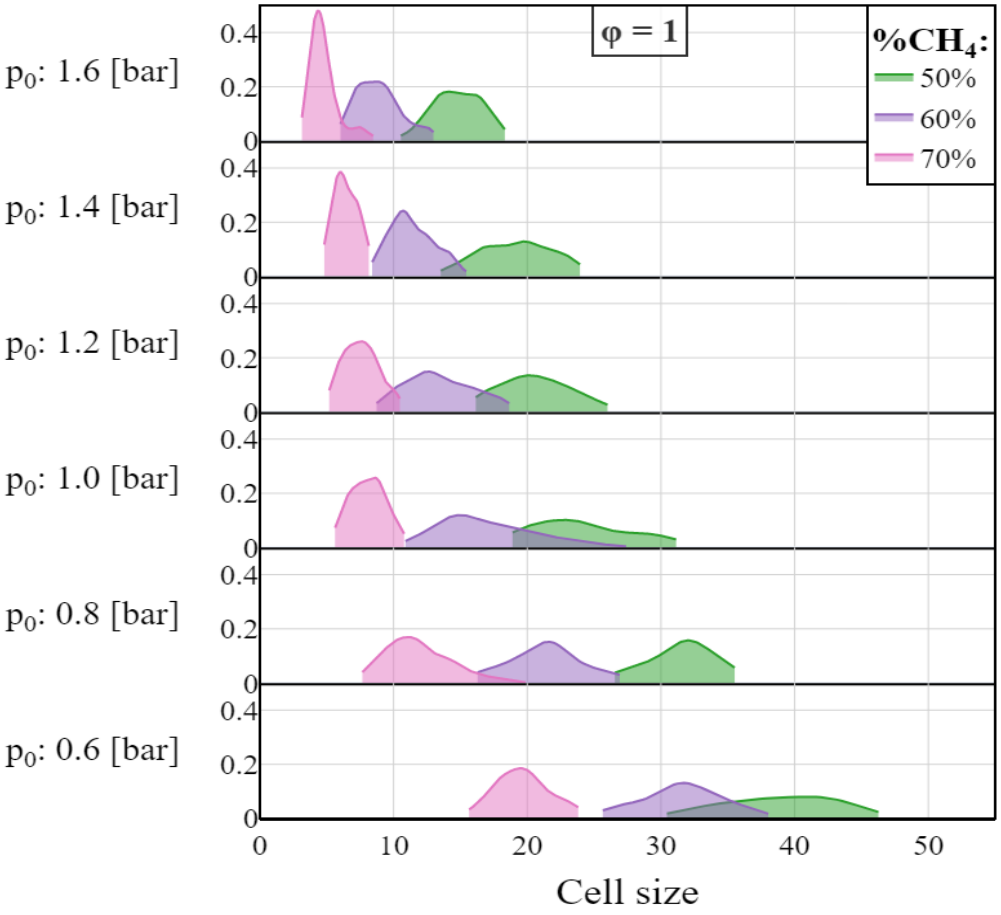


**Figure 34** Cell size distributions for the equivalence ratio $\phi$ = 1, different initial pressure $p_0$ and biogas compositions.

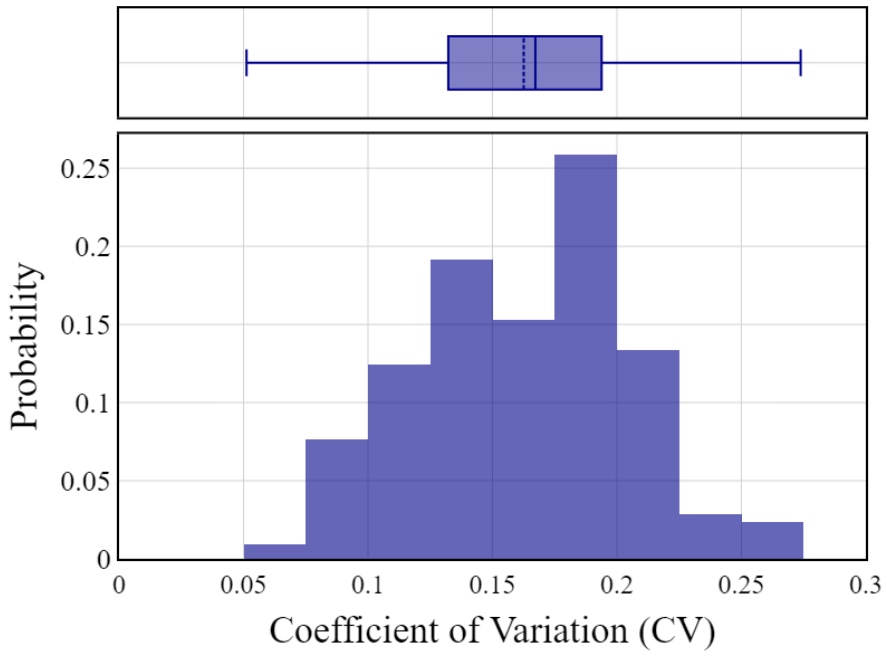


**Figure 35** Distribution of the Coefficient of Variation (CV), shown in a form of: a boxplot and a histogram.

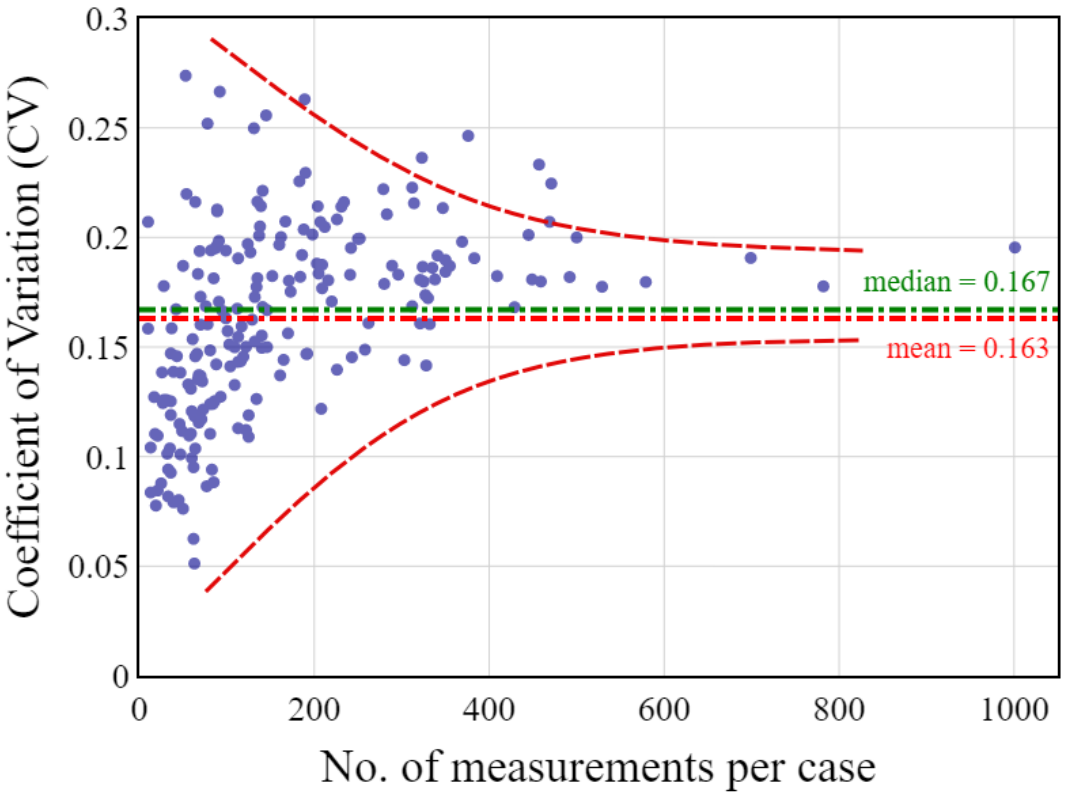


**Figure 36** Coefficient of Variation plotted against the number of measurements collected for every case.

## 4.6. Summary of the experimental part

In the section 4 the experimental part of the described work was presented. First, the experimental setup as well as the procedure were described in details. Next, the influence of the mixture's initial parameters: equivalence ratio $\phi$, initial pressure $p_0$ and the methane content in biogas, on the average detonation cell size was discussed. Additionally, the results of ZND induction length calculations and its correlation with the cell size were provided. What is more, the stability parameter $\chi$ for the researched cases was calculated and compared with the literature. This in turn, proved what was seen during the experimental campaign, that the cellular structure of the biogas – oxygen detonation is highly irregular. Finally, the statistical description and analysis of the collected measurements was conducted. In the course of the experiments over 35 thousand cell size measurements were gathered. The distribution of number of measurements per case was shown and discussed together with the distribution of standard error of the mean. Lastly, the measurements variation and a way to compare it across different cases, in form of a coefficient of variation (CV) was presented.

# 5. Prediction model of the detonation cell size

In this section, the results gathered through the experimental campaign described in the previous section are used to train a machine learning model for predicting the detonation cell size using the mixture's initial parameters: $p_0$, $\phi$ and $\%CH_4$. It is important to note that the models were restricted only to those three parameters and their combinations or transformations. The rationale behind it was that, firstly, those parameters are easy to obtain by direct measurement or simple calculation, and secondly, they are not based on any kind of assumptions. Many other parameters like activation energy, induction length etc. depend on a number of assumptions stemming out from the choice of a kinetics mechanism. As such, they introduce an additional source of error into the calculations and make it harder to compare results between studies. What is more, those parameters usually must be calculated beforehand using special software increasing the workload. From the practical point of view, being able to quickly predict the detonation cell size using only basic parameters like initial pressure, equivalence ratio and biogas composition, is an additional advantage. It saves time and, as already mentioned, reduces the workload of a person conducting, for example safety analysis or designing a detonative combustion chamber.

In the following subsections, results obtained from three different types of ML models: linear regression (LR), support vector regression (SVR) and neural network (NN), are presented. Typically a process of training a model requires checking a number of different versions of the same model creating tens of them along the way. In following subsections only the final results are presented. For every of the aforementioned three types of the models, two 'final' models were created and discussed using two different approaches. In the first one, the model was trained using average cell sizes. This means that the dataset on which model was trained and tested consisted of a single row for every tested case, each unique combination of $p_0$, $\phi$ and $\%CH_4$ corresponded with one value of an average cell size. The data was first aggregated and then used to train the model. In the second approach, raw measurements were used which resulted in a different number of datapoints corresponding to every case. As mentioned in the previous sections, those numbers ranged from around dozen to few hundreds and even around thousand for one of the cases. The idea behind testing both of the approaches is that although, in general, while training the model, the more data the better, it is not always possible to collect such vast amounts of data. Especially, when one considers a case of gathering the data through a literature review. Usually, in the literature only an average cell size is provided. This is why in this work the comparison of both approaches is provided, in order to

check how much they will differ from each other. Additionally, the models are also cross-checked by using the model trained on averages to predict on raw data and vice versa. This is done to provide a full, comprehensive comparison of the both versions of the model.

However, before presenting the results, sections 5.1 ÷ 5.3 describe some common techniques and parameters used in all models, in order to introduce more background and make the latter parts more understandable.

## 5.1. Metrics used to measure the quality of fit

As the metrics used to assess the quality of a model fit are common among all the models presented below it makes sense to introduce them separately. In the subsections below, four most popular metrics that were used in course of this work are presented. These are: Coefficient of Determination ($R^2$), Mean Squared Error (MSE), Mean Absolute Error (MAE) and Mean Absolute Percentage Error (MAPE).

### 5.1.1. Coefficient of determination ($R^2$)

The coefficient of determination $R^2$ is one the most widely used metric used to assess the quality of a model fit. In general terms, it measures the proportion of variance in the independent variable Y explained using variable(s) X [87]. It takes on a value between 0 and 1. The closer the value of $R^2$ is to 1, the better the fit is. An additional advantage of this metric is that it is independent of the scale of Y. To calculate $R^2$ the following formula is used:

$$R^2 = \frac{TSS - RSS}{TSS} = 1 - \frac{RSS}{TSS} \tag{15}$$

where TSS and RSS are the Total Sum of Squares and Residual Sum of Squares, respectively. They are defined as follows:

$$TSS = \sum_{i=1}^{n} (y_i - \bar{y})^2 \tag{16}$$

$$RSS = \sum_{i=1}^{n} (y_i - \hat{y}_i)^2 \tag{17}$$

here $y_i$ is the $i^{th}$ observed ("real") response value, $\bar{y}$ is the average of all the observed response values, $\hat{y}_i$ is the $i^{th}$ response value predicted by the model and n is the number of observations.

One issue with the $R^2$ metric is the fact that with an increasing number of variables added to the model the RSS always decreases leading to increase in $R^2$. This is true even if a variable is, in fact, meaningless or its influence over the dependent variable Y is minimal. To avoid unnecessary adding more and more variable a metric called 'Adjusted $R^2$' can be used.

This metric takes into account the number of variables used in a model as well as the number of observations. This metric is defined as follows:

$$Adjusted R^2 = 1 - \frac{RSS/(n-d-1)}{TSS/(n-1)} \tag{18}$$

where RSS, TSS and n are defined the same as in equation (17) and d is a number of variables in the model. The advantage of this metric over the $R^2$ is that while RSS always decreases with the increasing number of features in the model, $RSS/(n-d-1)$ may either increase or decrease, due to the presence of d in the denominator.

### 5.1.2. Mean Squared Error (MSE)

Another commonly used metric quantifying the quality of fit is the Mean Squared Error. It is defined as follows:

$$MSE = \frac{1}{n}\sum_{i=1}^{n}(y_i - \hat{y}_i)^2 \tag{19}$$

It always has a positive value due to the squaring of the error term. The closer the value of this metric is to 0 the better fit has been achieved. This metric is very similar to the Mean Absolute Error that is shown in the next subsection, but due to the square term it is more influenced by higher errors than MAE.

### 5.1.3. Mean Absolute Error (MAE)

Mean Absolute Error is yet another metrics use to measure the accuracy of a model. It is defined as follows:

$$MAE = \frac{1}{n}\sum_{i=1}^{n}|y_i - \hat{y}_i| \tag{20}$$

It can be interpreted as the average error that can be expected from the model in comparison to the actual observations. The closer it is to 0, the more accurate the model is. One drawback of this metric is that it is given on the same scale as the dependent variable that is being predicted. This in turn means that its value can only be interpreted within the dataset.

### 5.1.4. Mean Absolute Percentage Error (MAPE)

Last metrics that is presented is the Mean Absolute Percentage Error. It is defined as mean of all absolute percentage errors. In other words it is mean percentage difference between observed and predicted observations. An advantage of this metric is that, in contrast to Mean Absolute Error, it is a percentage which allows to use this metric to compare model accuracy across different use cases and datasets. Mathematically it is defined as follows:

$$MAPE = \frac{1}{n}\sum_{i=1}^{n} \frac{|y_i - \hat{y}_i|}{y_i} \quad (21)$$

## 5.2. Feature Engineering

Feature Engineering is a term that relates to the process of modifying or transforming an independent variable in order to achieve better model performance. There is a wide variety of techniques that might be employed and they depends heavily on the data and on the desired results. A simple example is transforming an independent variable X into $X^2$ or ln(X) if the data suggests that there might be such a relationship present between Y and X. Those kind of transformations were employed and showed in the previous subsections describing the relationship between an average cell size $\lambda$ and $p_0$ and $\phi$.

## 5.3. Cross validation

Cross validation (CV), or *k*-fold Cross Validation, is a commonly used technique for assessing model fit and stability and searching for model's parameters. When performing CV, the dataset is first randomly divided into a *k* equal-sized sets, usually 5 or 10, and then the model is trained on *k-1* sets and tested on the remaining one. The process is repeated *k* times, each time testing on a different set and training on the remaining *k-1* sets. The results of the *k* rounds of training and testes are then averaged and reported as a cross-validation score. When using this technique a researcher can not only obtain better estimation of the quality of the model fit but also model's stability can be checked by examining the results in each round. If in all of them the metrics were stable and did not differ too much from each other, it can be concluded that the model is stable and is not influenced too much by any single observation.

## 5.4. Linear Regression model: theory and results

### 5.4.1. Linear Regression theory

Linear regression is one of simplest and oldest type of ML models. Nevertheless, it is still very useful and capable. It belongs to the family of parametric models which means that the type of the relationship a model is trying to approximate is assumed up front. In case of a linear regression the model being trained has the following form:

$$y_i = \beta_0 + \beta_1 x_{i1} + \beta_2 x_{i2} + \cdots + \beta_p x_{ip} + \varepsilon_i, \text{ i} = 1, 2, \ldots, \text{n} \quad (22)$$

where, n is the total number of observations in the dataset, p is a number of independent variables, $y_i$ is the $i^{th}$ observation of the dependent variable and $x_{ip}$ is the value of $p^{th}$ predictor corresponding with the $i^{th}$ observation. The coefficients $\beta_0, \beta_1, \ldots, \beta_p$ are the model's parameters that are being found in the process of model training. Interpretation of a parameter $\beta_i$ is as

follows, it is an average change of Y in response to a unit change in $x_i$ while holding all the other independent variables fixed. The $\varepsilon_i$ is the error term for the $i^{th}$ observation. It is assumed that it comes from a normal distribution with some unknown variance and mean equal to 0, mathematically: $\varepsilon \in N(0, \sigma^2)$. The parameters $\beta_0$, $\beta_1$, …, $\beta_p$ are found using the least squares method that chooses a set of those parameters' values that minimizes the sum of squared residuals, called residual sum of squares (RSS). The residual is another name used for the error term $\varepsilon_i$ and can be defined as the difference between the actual and predicted value of the dependent variable. The formulas for $\varepsilon_i$ and RSS are as follows:

$$\varepsilon_i = y_i - \hat{y}_i \tag{23}$$

$$RSS = \sum_{i=1}^{n} \varepsilon_i^2 = \sum_{i=1}^{n} (y_i - \hat{y}_i)^2 \tag{24}$$

Nowadays those calculations are easily done using one of many available programs and/or programming languages like Matlab [134], Python [135] or R [136]. In case of the presented work, all the calculations and models training were done using Python, and more specifically the training of the models was done using Python library – scikit-learn [137]. This library includes a wide variety of machine learning models as well as additional functions that let the user perform feature engineering and model quality assessment tasks.

Before presenting the results it is important to mention an effect called a synergy or, alternatively, interaction. It is a case in which a change in one independent variable values influences the effect another independent variable has on the dependent variable. In order to account for the synergy effect in a model a product of multiplication of both variables is added as, another predictor [87]. It can be shown using a simple example of a model consisting of two predictors: $x_1$ and $x_2$, this is shown in the equation (25). Adding the interaction term as a third predictor results in the equation (26) that can be then rewritten into the form shown in (27). It is now clearly visible that the value of the parameter $\widetilde{\beta_1}$ depends on the value of $x_2$.

$$y_i = \beta_0 + \beta_1 x_{i1} + \beta_2 x_{i2} \tag{25}$$

$$y_i = \beta_0 + \beta_1 x_{i1} + \beta_2 x_{i2} + \beta_3 x_{i1} x_{i2} \tag{26}$$

$$y_i = \beta_0 + (\beta_1 + \beta_3 x_{i2}) x_{i1} + \beta_2 x_{i2} = \beta_0 + \widetilde{\beta_1} x_{i1} + \beta_2 x_{i2} \tag{27}$$

### 5.4.2. Linear Regression results

In the course of training the model a number of different features was tested. Those features consisted either of a base or transformed values of the three base variables ($p_0$, $\phi$, $\%CH_4$), or were in the form of interaction terms, for example $p0*\phi$. Finally, using 10-fold Cross

Validation, six parameters were selected as giving the best results: $p_0$, $\phi$, $\%CH_4$, $\phi^2$, $\ln(p_0)$ and ($p_0$ * $\%CH_4$). In order to properly train the model and then assess its performance, the dataset was divided into training and test set, with 80% of the data being assigned to the former and 20% to the latter. The performance of the model was measured by calculating the values of all of the metrics described in the subsection 5.1: $R^2$, $R^2_{adj}$, MSE, MAE and MAPE, using the test set.

Figure 37, shows the predicted detonation cell size plotted against the average cell size. The data comes from the test set. The colors marks the model version, blue points correspond to the model trained using average cell sizes while red points correspond to the model trained on raw data. The black, solid, diagonal line represents the perfect fit where the predicted value is equal to the real one. It can be seen that the latter, consistently predicts lower value of the detonation cell size, for every case. In some cases this results in the 'red model' being closer to

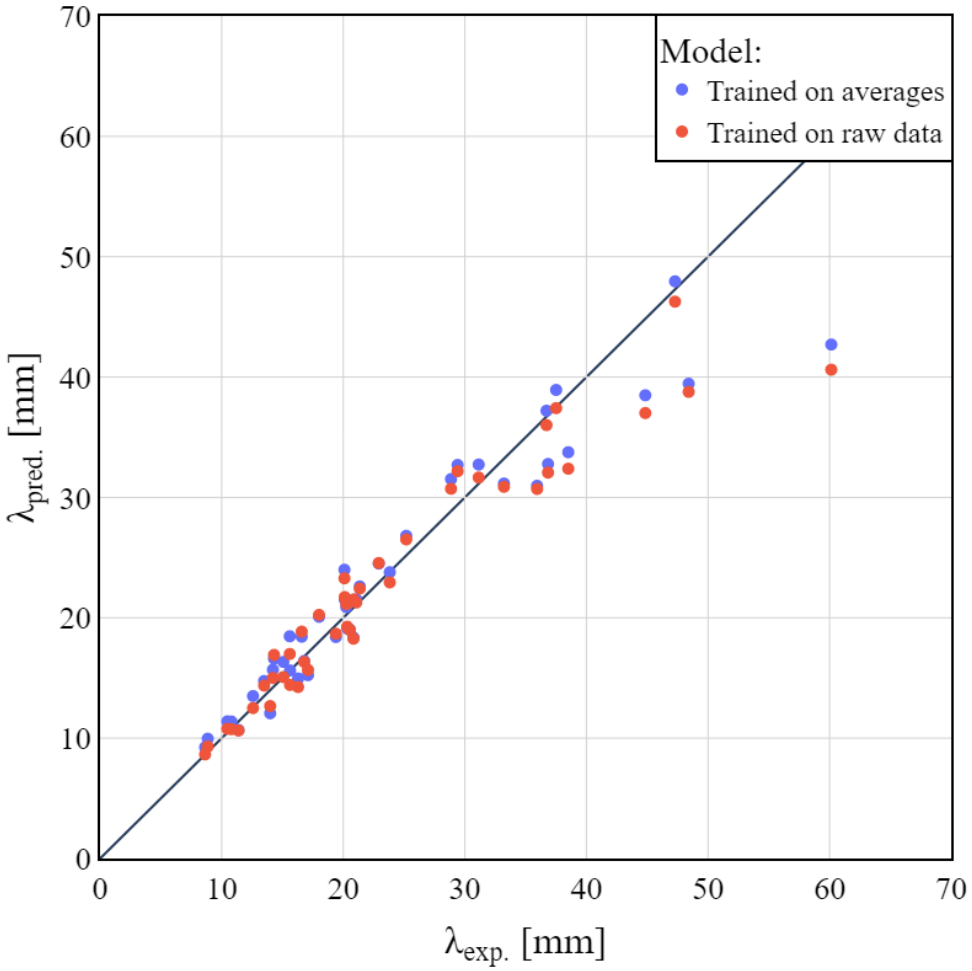


**Figure 37** Predicted cell size plotted against the calculated average cell size. The data comes from the test set.

**Table 3** The results of the Linear Regression models, tested on the aggregated test set.

| Model \ Metric | $R^2$ | $R^2_{adj}$ | MSE | MAE | MAPE |
|---|---|---|---|---|---|
| Trained on averages | 0.90 | 0.89 | 13.44 | 2.27 | 0.09 |
| Trained on raw data | 0.88 | 0.86 | 15.98 | 2.23 | 0.08 |

the perfect fit while sometimes it is further away. It is hard to judge which model is better, just by looking at the plot. In order to compare the models in a more formal way, the aforementioned metrics are calculated and presented in the Table 3. It can be seen that there is almost no

difference between the two models when tested on the aggregated test set. All of the metrics are almost identical and the observed differences are well within the expected variability. Nevertheless, both models prove to give very good results with low errors and high $R^2$. It is, however, important to notice that both models struggles with predicting the higher values of the detonation cell size. Those values correspond to the experiments with very low methane percentage in biogas. The coverage of experiments was smaller in that region as for biogas compositions 40-60 and 45-65 they were conducted only for $\phi = 1$. What is more, due to the larger cell size, the numbers of measurements collected for those cases were smaller which resulted in higher variance and less accurate estimation of the average cell size. This in turn led to a worse performance of the model in that region of parameter space. Nevertheless, it can be safely assumed that most probably, if the model was provided with more data it would fit better.

Figure 38a presents the same models but tested on the test set consisting of raw data collected from the experiments. Similarly to the Figure 37, the model trained on raw data predicts smaller cell size compared to the model trained on averages. What is more, the same problem with larger cell sizes is visible. However, in this plot it is easier to see that the number of datapoints is smaller and the variance is higher for the cases with larger cells. Interestingly, each separate case can be easily observed in the plot as horizontal lines of points. This is because the model predicts one value for every case while from measurements for each case a distribution of cell sizes was obtained. Those distributions are easily visible in the form of the, aforementioned, horizontal lines of points. However, they can be taken into account when assessing the fit of the model. It stands to reason to assume that if the values of the measurements fall within some range from the predicted value then the model prediction can be treated as a perfect fit. This is because, as mentioned earlier, for every case the cell sizes do not take a single value but rather follow some distribution, while the model predicts only one value. In the presented work, based on the analysis of the coefficient of variation it was assumed

that this range is ±17% of the predicted value. That range is represented by the yellow-shaded area in the Figure 38a. Figure 38b presents the same data but modified to take into account the cell sizes distributions, as described above. It can be seen that the cloud of the points is narrower as the black, diagonal line represents now, in a sense, the shaded region from the Figure 38a. Table 4 presents the values of the five metrics used to assess the quality of the model fit, for both models tested on the raw data. What is more, it presents those values before (part A) and after (part B) taking into consideration the distribution of the cell sizes, as described above. Analyzing the table, two conclusions can be drawn, first that there is virtually no difference between the two models, both give basically the same, very good results on the test set, with small errors and high $R^2$ of over 80%. Second conclusion is that, as expected, by taking into account the cell size distribution the results are greatly improved with the value of $R^2$ reaching 96%, average absolute error being below 1mm and average percentage error taking a value of 5%.

**a)**

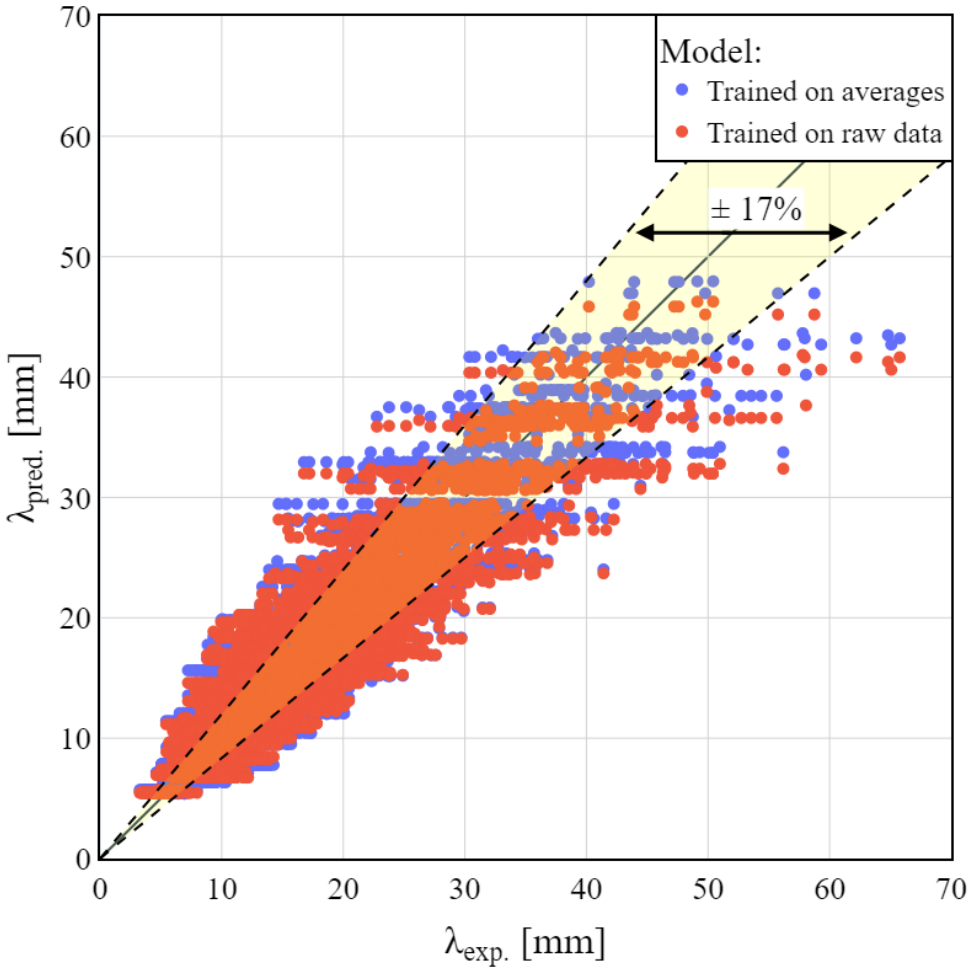

**b)**

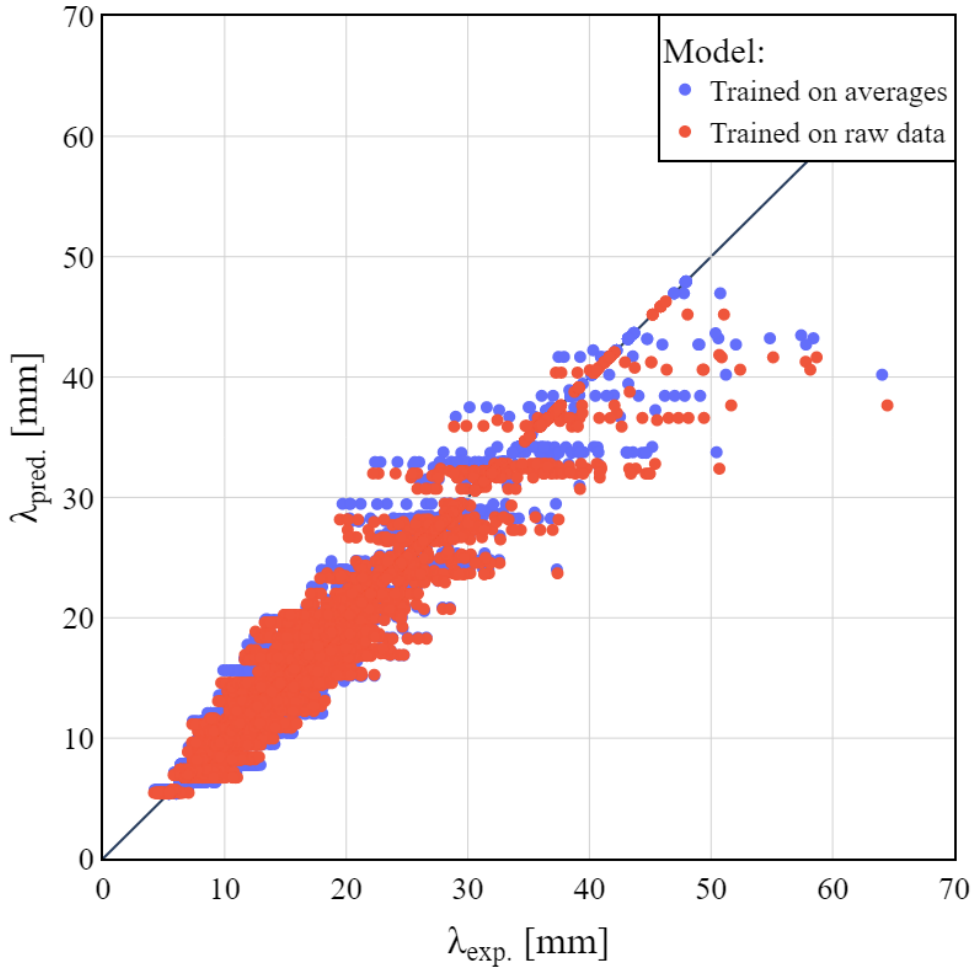


**Figure 38** Cell sizes predicted by LR models plotted against the measurements from the test set: a) – before taking into consideration the distribution of the cell sizes; b) after taking it into consideration.

Because of the simplicity of the Linear Regression model it's underlying equation can be easily extracted and analyzed. This is in contrast to the SVR and NN that are presented next. Those models are more flexible than LR but they do not provide a user with easily interpretable equation. It is a known trade-off of using more complicated types of models, that although usually they give better results but the underlying 'logic' cannot be easily extracted and explained. Nevertheless, that can be done in a case of Linear Regression and the Table 4 presents the equations of both models: trained on averages (eq. 28) and raw data (eq. 29). Again, it is evident that the differences between the models are not that big. Two biggest differences are the values of the coefficients next to the parameters $\ln(p_0)$ and $p_0$. Interestingly, the coefficient corresponding to the second parameter has different signs between the equations. In the equation (28) it is positive while in the equation (29) it is negative. Nevertheless, the influence of the parameter $p_0$ is minimal as the absolute value of the corresponding coefficient is small compared to the rest.

$$\lambda_{pred\ avg.} = 77.52 - 45.58 * \phi + 22.81 * \phi^2 + 5.92 * p_0 - 61.17 * ln(p_0) - 125.93 * (\%CH_4) + 52.12 * (p_0 * \%CH_4) \quad (28)$$

$$\lambda_{pred\ raw.} = 87.16 - 43.53 * \phi + 21.97 * \phi^2 - 6.36 * p_0 - 49.04 * ln(p_0) - 124.98 * (\%CH_4) + 54.0.7 * (p_0 * \%CH_4) \quad (29)$$

**Table 4** The comparison of the LR models trained on average and raw data: A – without taking into consideration cell size distribution; B – with taking into consideration cell size distribution.

| Version \ Model \ Metric | | $R^2$ | $R^2_{adj}$ | MSE | MAE | MAPE |
|---|---|---|---|---|---|---|
| **A** | Trained on averages | 0.82 | 0.82 | 13.03 | 2.71 | 0.18 |
| | Trained on raw data | 0.82 | 0.82 | 12.73 | 2.64 | 0.18 |
| **B** | Trained on averages | 0.96 | 0.96 | 2.71 | 0.78 | 0.05 |
| | Trained on raw data | 0.96 | 0.96 | 2.77 | 0.75 | 0.05 |

## 5.5. Support Vector Regression model

### 5.5.1. Support Vector Regression theory

Support Vector Regression is a variant of Support Vector Machine family of models. It is more complicated than Linear Regression but it also often gives better results when trained properly. This is because, thanks to so called 'kernel trick' it can handle non-linearity that might be present in the data. However, its drawback is that, in contrast to LR, it does not provide a simple, easy to analyze equation that shows how each of the parameters influence the prediction.

During the training, the model tries to fit a hyperplane that minimizes the errors, however, without taking into account points that fall withing the space surrounding the hyperplane. This is in contrast to LR in which it tried to fit a hyperplane using all datapoints. For the simplicity of explanation, an example of a simple model using only one feature is now described, an example of such model is shown in the Figure 39. The solid black line presents the fitted SVR model while the dashed lines presents the boundaries between which the errors are neglected. Those lines boundaries are positioned at the distance ±ε from the fitted function. During the training the model tries to find such a hyperplane that minimizes the errors marked with symbols ξ and $\xi^*$. The idea behind introducing the 'insensitivity zone' between ±ε is to accommodate for the possible noise that might occur in the data. In the simplest form the SVR fits a straight line using a linear kernel, as shown in the Figure 39. However, by using different

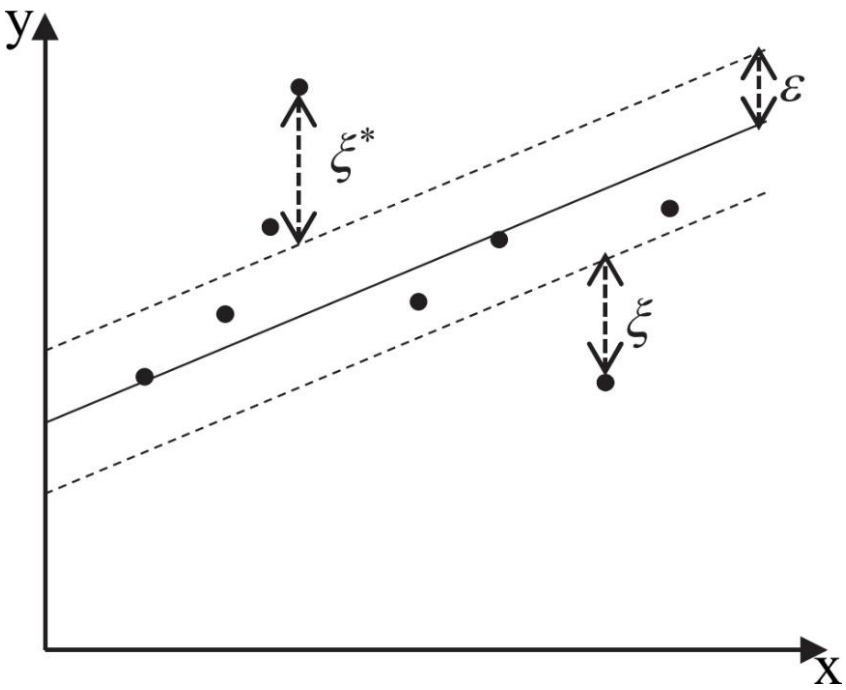


**Figure 39** An example of an SVR trained on one variable x [105].

kernels the model can be expanded to fit non-linear problems. A kernel allows to implicitly expand the feature space to a higher dimension. This is a huge advantage over doing this explicitly using functions of the original features because the number of calculations is significantly lower. Especially that for a sufficiently big feature space performing the explicit calculations would be simply impossible. There are many different kinds of kernel functions, the most commonly used is called the Guassian kernel or also RBF which stands for Radial Basis Function. This kernel is also used in the calculations that are presented in the following subsection as it proved to offer the best results.

In mathematical terms, the fitted function (eq. 30) and the kernel (eq. 31) have the following forms:

$$\lambda_{pred.} = f(x) = \beta_0 + \sum_{i=1}^{n} \alpha_i K(x, x_i) \tag{30}$$

$$\mathrm{K}(\mathrm{x_i}, \mathrm{x_j}) = \exp\left(-\gamma \sum_{j=1}^{p} \left(x_{ij} - x_{i'j}\right)^2\right) \tag{31}$$

where $n$ is the number of datapoints, $p$ is the number of independent variables, and $x_{ij}$ and $x_{i'j}$ are $i^{th}$ and $i'^{th}$ datapoints, while $\beta_0$, $\alpha_0$ and $\gamma$ are model's parameters determined during the training. An interested reader is referred to the works of Smola and Schölkopf [138], Schölkopf and Smola [139] and James et al. [87], for a more in-depth overview of the topic.

### 5.5.2. Support Vector Regression results

In order to make the results of different models comparable it was decided to use the same set of independent variables which were used in LR training: $p_0$, $\phi$, $\%CH_4$, $\phi^2$, $\ln(p_0)$ and ($p_0$ * $\%CH_4$). Additionally, using a cross validation the best type of kernel and the hyperparameter C was found. The former was discusses above while the latter – C, is a regularization parameter that controls the trade-off between maximizing the margin and minimizing the training error. The larger the C the heavier penalty is put for deviations from the tolerance zone. This in turn results, in model trying to fit the data more closely, which might potentially to overfitting. On the other hand, to small C might lead to a larger margin and ultimately to underfitted model. In order to find the optimal value of C, the cross-validation should be applied, which was done. It was found that the model performs best when the value of C is set to 1000. The chosen kernel, as mentioned above, was RBF.

Figure 40 shows the cell size predicted by two models, plotted against the aggregated, average cell size. Just as in Figure 37, the two models are differentiated by the colors while the diagonal, solid, black line shows the perfect match. The scales of the X and Y axis are the same as in the section discussing linear regression. It can be seen that both models give very good

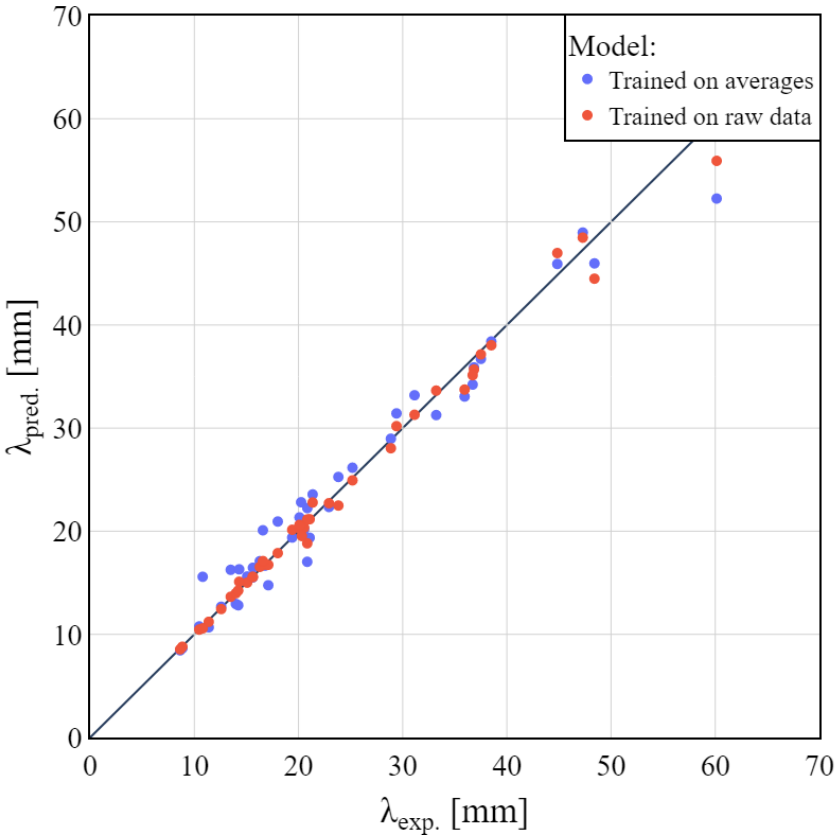


**Figure 40** Predicted cell size plotted against an average cell size for the cases from the test set. The results are shown for two models: blue – trained on averages, read – trained on raw data.

results with model trained on raw data looking slightly better. Nevertheless, compared to the LR results (see Figure 37), it can be seen that both SVR models behave significantly better, especially at the upper end of the spectrum, where the cell sizes are big. The predictions for the average cell size of around 60 mm are significantly closer to the diagonal line than in the Figure 37. It becomes more evident when one compares the Tables 3 and 5, showing the calculated metrics for LR and SVR models, respectively. It instantly evident that the results are exceptionally good, the coefficient of determination equals 97% for model trained on averages and reaches 99% in case of the model trained on raw data. What is more all the error metrics (MSE, MAE, MAPE) are very small, significantly smaller than in case of LR. It is especially visible in case of MSE which is very sensitive to bigger errors and was heavily influenced by the big errors at the, aforementioned, upper end of the spectrum. To sum up, when tested on the aggregated test set, both models give very good results, both better than LR, while between SVR models the one trained on raw data gives best results.

**Table 5** The results of the Support Vector Regression models, tested on the aggregated test set.

| **Model \ Metric** | **$R^2$** | **$R^2_{adj}$** | **MSE** | **MAE** | **MAPE** |
|---|---|---|---|---|---|
| Trained on averages | 0.97 | 0.96 | 4.6 | 1.55 | 0.07 |
| Trained on raw data | 0.99 | 0.99 | 1.38 | 0.7 | 0.02 |

Figure 41 presents the cell sizes predicted by both models, plotted against raw data coming from the test set. Similarly to Figure 38, Figure 41a presents the results before taking the cell size distribution and Figure 41b, after making the correction. The results look very similar to those of linear regressions except for the predictions in the upper spectrum of the cell sizes. Similarly to the Figure 40, it can be seen that SVR models perform better than LR when it comes to predicting big cell sizes. Table 6 presents the quality of fit metrics calculated for the SVR models tested on the raw data test set, with and without taking into account cell size distribution. Comparing those results to the corresponding ones for LR, shown in Table 4, one can see that this time the differences are not as significant as in case of testing on the aggregated test set described above. The differences in coefficient of determination $R^2$ and MAPE are around 1% between models, while differences in MAE are well below 1 mm. This might suggest that the models are reaching their limits beyond which they will not be able to progress due to the noise in the data. Nevertheless, both SVR models, the one trained on aggregated data as well as the one trained on raw data, shows very good results.

**a)**

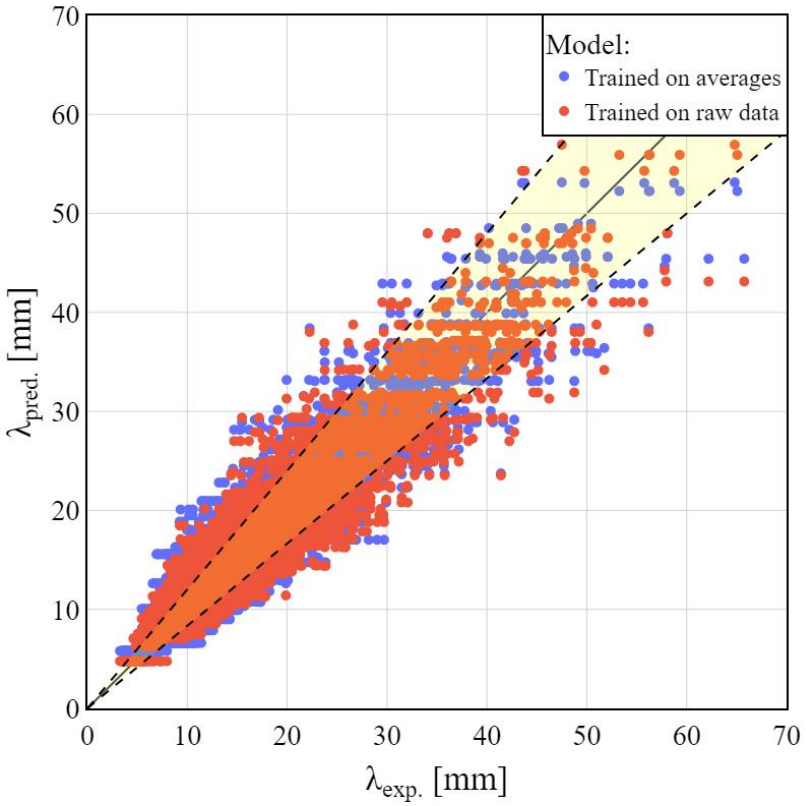


**b)**

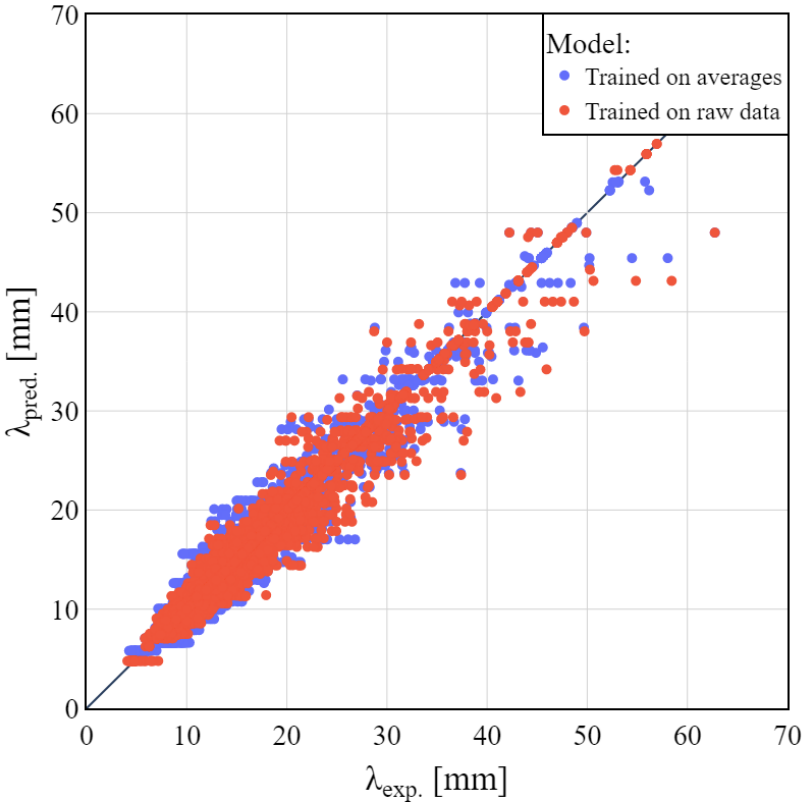


**Figure 41** Cell sizes predicted by SVR models plotted against the measurements from the test set: a) – before taking into consideration the distribution of the cell sizes; b) after taking it into consideration.

**Table 6** The comparison of the SVR models trained on average and raw data: A – without taking into consideration cell size distribution; B – with taking into consideration cell size distribution.

| Version \ Model \ Metric | | $R^2$ | $R^2_{adj}$ | MSE | MAE | MAPE |
|---|---|---|---|---|---|---|
| **A** | Trained on averages | 0.85 | 0.85 | 10.94 | 2.5 | 0.17 |
| | Trained on raw data | 0.86 | 0.86 | 9.86 | 2.34 | 0.15 |
| **B** | Trained on averages | 0.97 | 0.97 | 1.92 | 0.63 | 0.04 |
| | Trained on raw data | 0.97 | 0.97 | 1.64 | 0.55 | 0.04 |

## 5.6. Neural Network model

### 5.6.1. Neural Network theory

Neural Network (NN), also known as Artificial Neural Network (ANN), is a type of machine learning model inspired by the structure and principle of operation of a human brain. They are used for various tasks such as classification, regression, pattern recognition, image recognition or, very popular lately, text generation [140].

A neural network is built using neurons, also called perceptrons or nodes. The simplest version of neural network is just one neuron. On the other hand those neuron can be stacked together into one or many layers connected in different ways producing huge networks capable of performing very complicated tasks. Figure 42 presents the schematics of a basic building block of a neural network – neuron. A neuron takes a number of multiple input signals, processes them, and produces an output. Inside the neuron, the input signals are multiplied by a corresponding weights and then summed. Finally the sum is passed by an activation function that introduces non-linearity to the neuron. This step enables the network to learn complex relationships and patterns in the data.

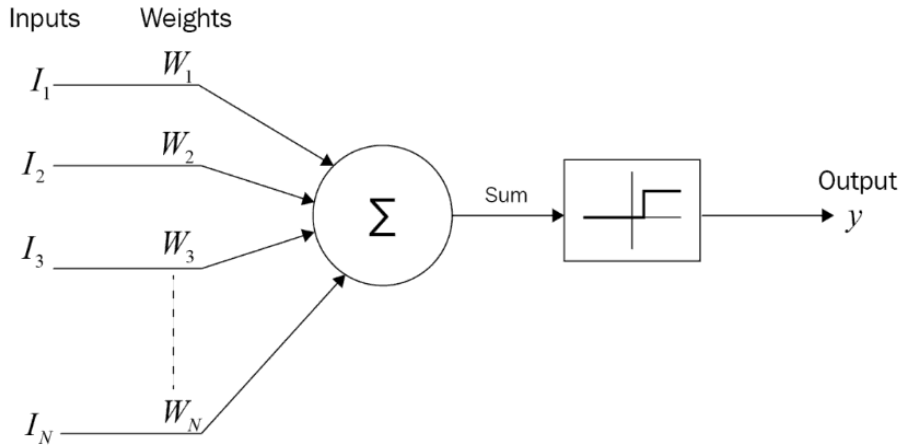


**Figure 42** A schematics of a singular building block of neural network – neuron [141].

As mentioned above, a neural network consists of a multiple layers of interconnected neurons. Depending on the network's architecture, on how the neurons are connected, many different types of networks can be distinguished. In this thesis a very popular architecture of fully connected neural network, called Multi-layer Perceptron (MLP) was used. It is sufficient for a relatively simple task of regression. The architecture of MLP used in the presented research is shown in the Figure 43. First is the input layer that receives the input data and passes it to the next layer. After the input layer, the hidden layers are positioned. They are responsible for learning and extracting the patterns from the data. The number of layers and nodes in those layers is a subject of optimization. In the presented study, using the 10-fold cross-validation method it was found that the best results are achieved for 5 hidden layers with 10 neurons in each. For the clarity of the image only, first and last hidden layer are shown in the figure below. Finally, at the end of the network an output layer consisting of one neuron is placed, that produces the final output. The number of neurons in that layer depends on the type of problem being solved. In case of a regression predicting only one value there is only one neuron, the same would be in a case of a binary classification problem. On the other hand, if the problem was a multi-class classification, the number of neurons in the output layer would match the number of predicted classes.

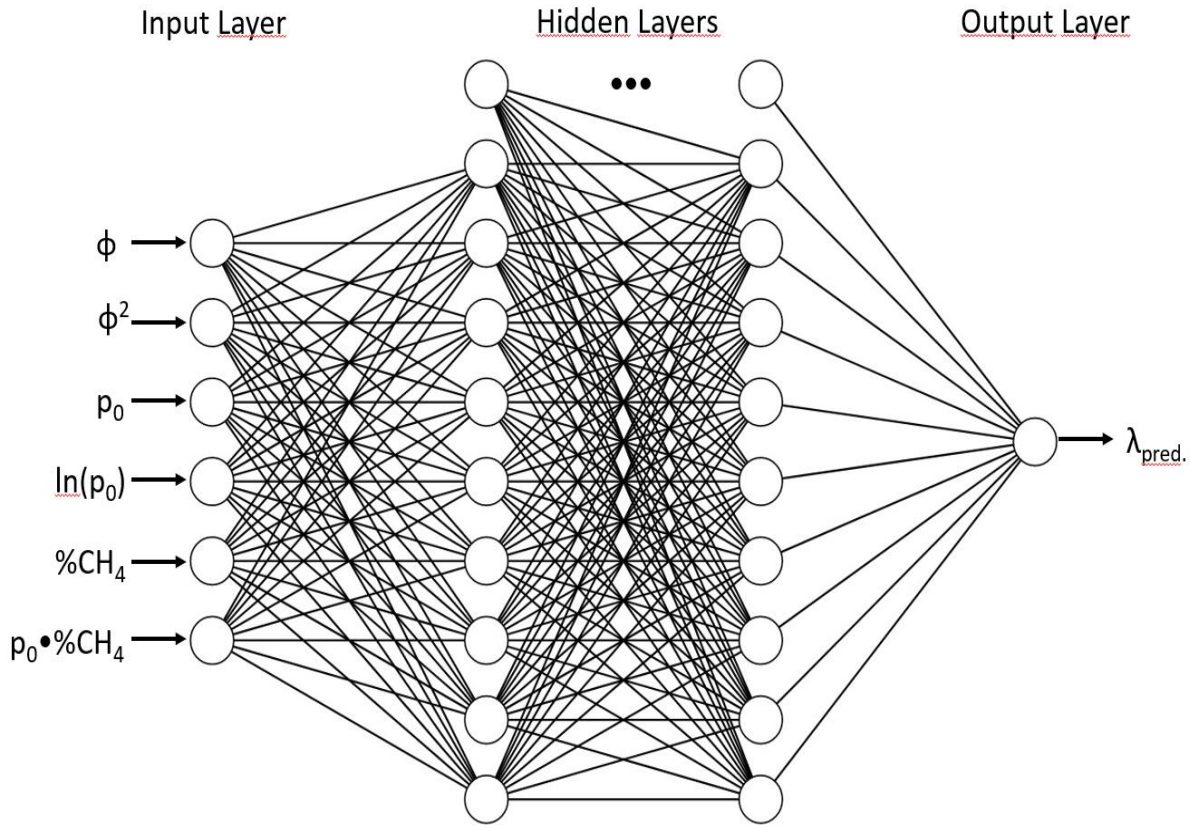


**Figure 43** The schematics of the Neural Network used in the presented study.

The process of training the network consists of three steps repeated iteratively until some stopping criteria is achieved, for example the error stopped decreasing for a number of iterations. In the first step the forward propagation is run, which is simply a forward pass of the input values through the network in order to obtain the predictions for the training set. In order to start the process of training, before the first forwards pass the weights in the network are initiated using random values. In the second step the output of the forward pass is compared to the ground truth labels and the value of a loss function is calculated. Finally, the backpropagation is performed. In this step, the algorithm updates the weights in the network using a predefined optimization algorithm like, for example Stochastic Gradient Descent (SGD) or its variant.

### 5.6.2. Neural Network results

In this section the results of training and testing the Neural Network model are presented. However, in contrast to the sections presenting the results for LR and SVR models, in this section only model trained on raw data is described. This is because the results of the model trained on the aggregated data were very poor. The model tended to overfit giving good results on the training set and very poor results on the test set. Neural networks are known to need a lot of data to be properly trained, in case of the presented study, 174 training points is a very low number. This is, most probably, the reason for very poor results of the NN trained on the aggregated data. On the other hand, the results of the model trained on raw data were very good and they are presented below.

Figure 44 presents the predicted vs measured cell size, without (Figure 44a) and with (Figure 44b) taking into consideration the detonation cell size distribution. It can be seen that the results look similar to those presented in the sections treating about LR and SVR results. There is not much difference in the spread of the data in both plots when compared to Figures 38 (LR results) and 41 (SVR results). All of those models were trained on the same training dataset. However, in case of NN, on can notice that some of the points in the upper spectrum of cell sizes appear to be missing. This is because while training the NN another set of data was used, called validation set. Its purpose was to tune the hyperparameters during the training of the model. This set was generated by randomly splitting the usual test set into two equal-sized groups. Out of those two groups one was used as validation set and the second one, as test set. The lack of some points with high cell sizes value means that they are in the validation set. Table 7 presents the values of the $R^2$, MSE, MAE and MAPE metrics, with and without taking into account the distribution of the cell sizes. It can be seen that for both cases the results are

**a)**

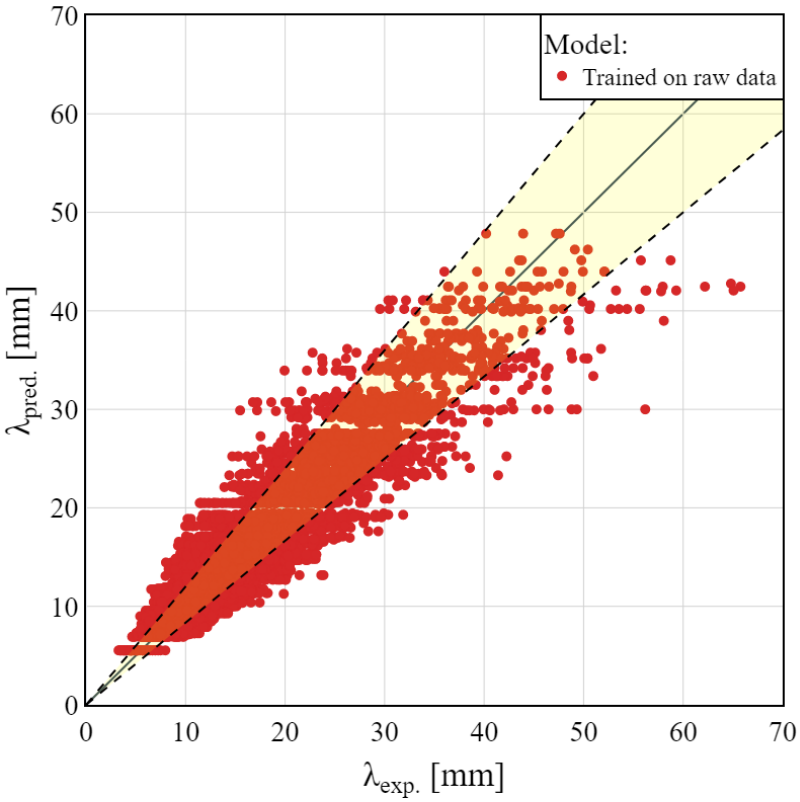


**b)**

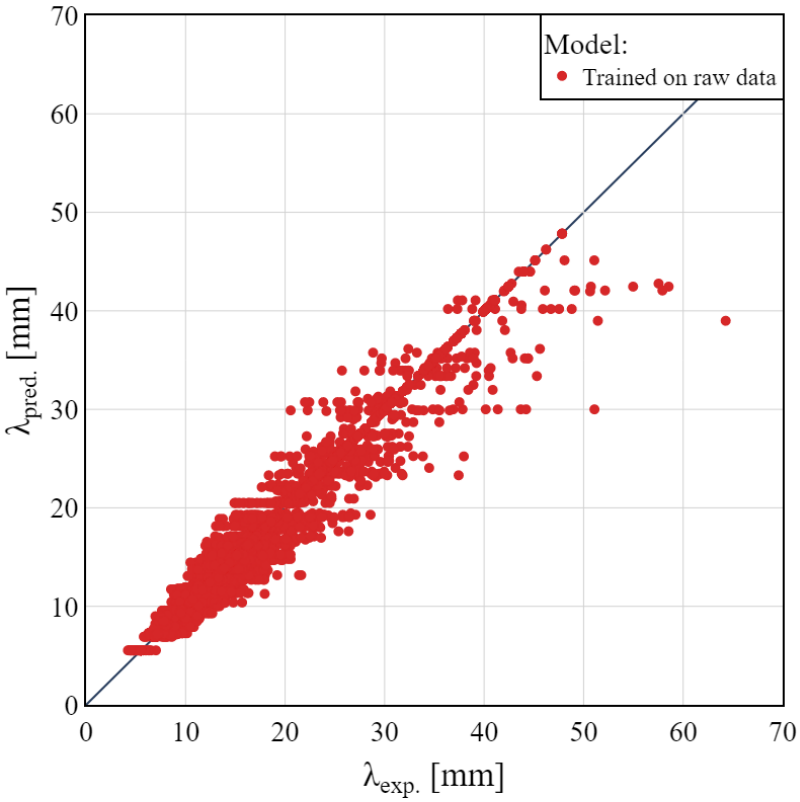


**Figure 44** Cell sizes predicted by NN model plotted against the measurements from the test set: a) – before taking into consideration the distribution of the cell sizes; b) after taking it into consideration.

very good with $R^2$ reaching 97%, MAE taking the value of 0.6 mm and MAPE 4%. Those results are comparable to the results achieved by SVR and are slightly better than those achieved by LR model.

**Table 7** The comparison of the results of the NN model trained on raw data: A – without taking into consideration cell size distribution; B – with taking into consideration cell size distribution.

| **Version \ Model \ Metric** | | **$R^2$** | **$R^2_{adj}$** | **MSE** | **MAE** | **MAPE** |
|---|---|---|---|---|---|---|
| **A** | Trained on raw data | 0.85 | 0.85 | 11.18 | 2.49 | 0.16 |
| **B** | Trained on raw data | 0.97 | 0.97 | 2.15 | 0.66 | 0.04 |

In the Figure 45 and Table 8 the results of testing the NN trained on raw data on the aggregated test set are shown. It can be seen that the results are also very good, with R2 reaching 93%, MAE being at the level of 1.85 mm and MAPE at 7%. Nevertheless, it is also visible that, similarly to the LR and SVR, the NN has some problems with correctly predicting the big cell sizes. The predictions in that area are slightly better than those of Linear Regression but worse than those of Support Vector Regression.

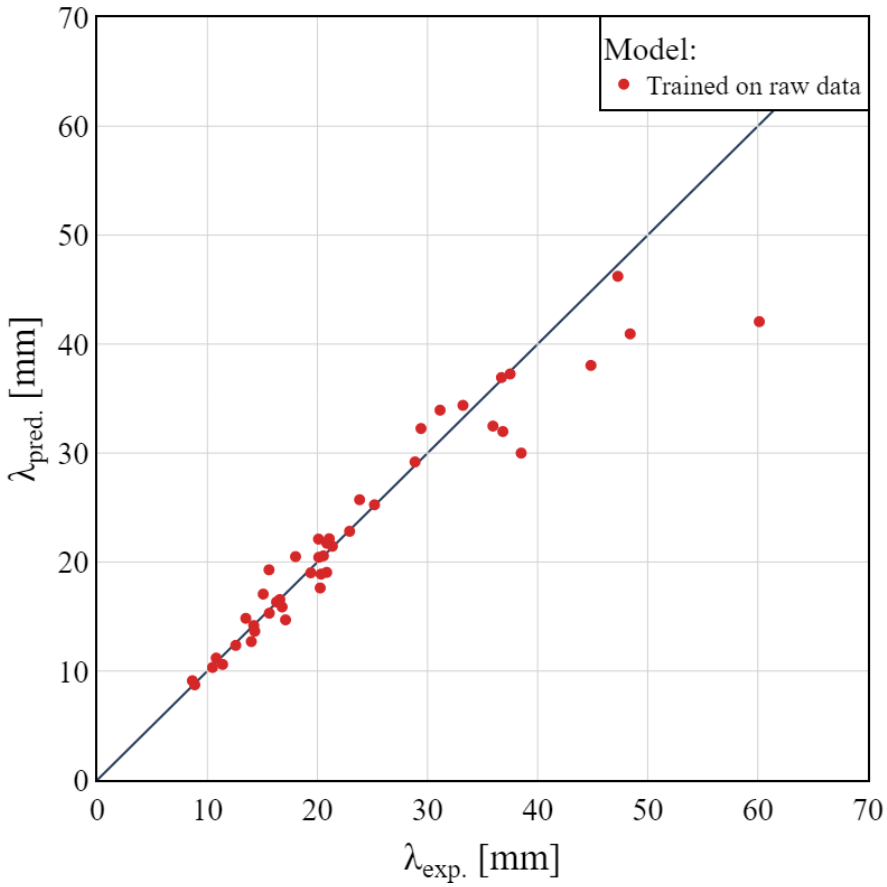


**Figure 45** The predicted cell size vs the average cell size from the aggregated test set, predictions done using the NN trained on the raw data.

**Table 8** The results of the Neural Network model, tested on the aggregated test set.

| Model \ Metric | $R^2$ | $R^2_{adj}$ | MSE | MAE | MAPE |
|---|---|---|---|---|---|
| Trained on raw data | 0.93 | 0.92 | 9.50 | 1.85 | 0.07 |

## 5.7. Examples of prediction for conditions that were not in the dataset

Figure 46 presents the comparison of the three types of models presented in the previous sections. Parts a), b) and c) present the average detonation cell size plotted against $\%CH_4$, $p_0$ and $\phi$. In case of a) and b), they present exemplary results for $\phi = 1$ and three selected values of $p_0$ or %CH4, respectively, while in case of c) the results are shown for a selected initial pressure of 1 bar and three different biogas compositions. The dots mark the experimental data while the three types of lines show the predictions of three different models: LR, SVR and NN. The predictions of the model are shown not only for the minimum-maximum values of a X-axis parameter tested in the experiments but also outside of this range. This is done, in order to shown the behavior of the models when predicting outside of the training data ranges. Lastly, it is important to note, that the axes in the Figure 46b have logarithmic scale.

It can be seen, that all three models give very similar results in terms of line shape. In some cases SVR better follows the data while in other it's LR or NN. Figure 46a gives some indications that LR and NN models were better in capturing the linear relationship between $\lambda$ and $\%\ CH_4$. On the other hand, in the same plot it is clearly visible why SVR gave better results in the upper end of the cell size spectrum – due to its high fidelity it was able to better fit the data. An open questions is, whether in this particular case it is a good thing. The data suggests that the relationship is strictly linear and the outlying point visible in the Figure 46a might just be of lower quality because the number of measurements for this case was low due to a very big cell size. Nevertheless, neither of the models results in a straight line in the Figure 46a, this is because those models do not use only one parameter but are a combination of a number of them. Another interesting observation is the behavior of the models outside of the training data range. It can be seen, LR and NN models, more or less follow the visible trend in the tested range. On the other hand, it is also clearly visible that in most cases a SVR model does not interpolate well outside the data range. This is especially well visible in the Figures 46a and 46b, in cases of higher values of $\%CH_4$ and $p_0$, respectively. The lines corresponding to the SVR model rise drastically when the model leave the training data space.

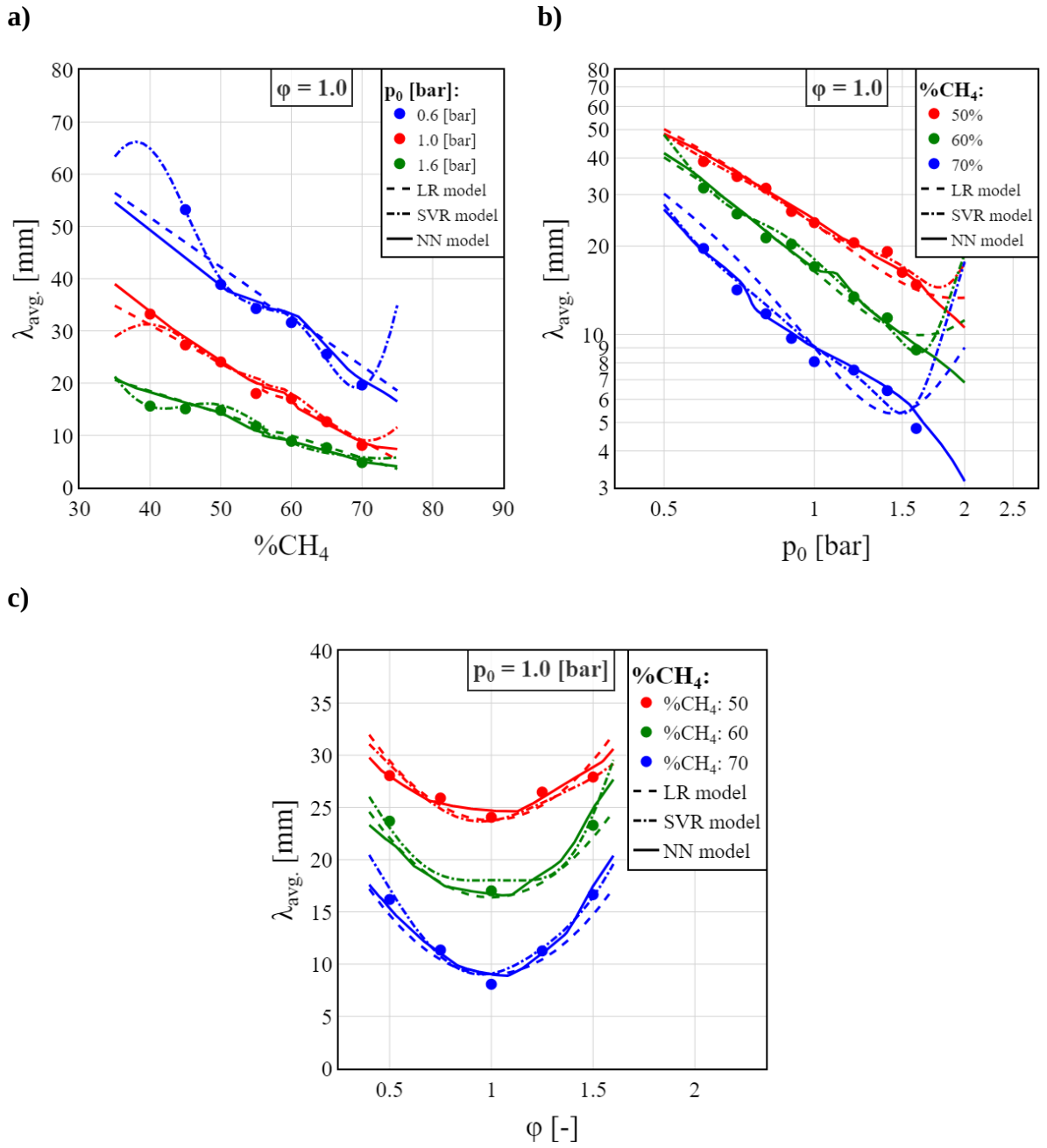


**Figure 46** Predictions of the LR, SVR and NN models for the selected ranges of the following parameters: a) methane percentage; b) initial pressure; c) equivalence ratio.

## 5.8. Limitations of the Machine Learning approach

As with everything, there are some limitations and obstacles that one must keep in mind when using a machine learning approach to predict the detonation cell size.

First of all, every model is only as good as the data it was provided during the training. Even the most complicated and sophisticated model, that is able to fit well to the provided data without overfitting, will not be able to give accurate results if the data was not correct. This is a very important point that one needs to always keep in mind when preparing and gathering the

data in order to train the model, be it from an experiment or from a literature review. Another important aspect of the model is what was shown in the subsection 5.7 – the behavior of the model outside of the data range used for training. It cannot be expected that a created model will generalize and predict well outside of that range.

What is more, a model created for a certain type of fuels/oxidizers/diluents might not generalize well for those not present in the training dataset. However, this is dependent on the parameters used to create the model. If they would be able to differentiate mixture properties on which the cell size depends, such a model might be able to generalize from mixtures used during training to others, even very different ones. However, to the author's best knowledge such models has not been created yet. Lastly, if the parameters used for model training depend on some other model/formula/assumptions, for example reaction kinetics mechanism, such a model will be bound by those assumptions. As an example, one might look at the model presented by Bakalis et al. [106]. The authors of this article note that although their model gave good results, it was created using a particular reaction kinetics mechanism and as such it might not work for every mixture.

In the presented study, the quality of the data was assured by carefully, gathering a large number of measurements from the experiments. For most of the cases the calculated average detonation cell size is of high quality, however for cases where the cell sizes were big resulting in a low number of measurement, the confidence intervals on the calculated averages are wider. In order, to avoid being dependent on reaction kinetics mechanism assumptions the model was trained using only three, very basic parameters that are easy to measure or calculate and do not depend on any assumptions. The model gives good results but is confined only to biogas-oxygen mixtures.

## 5.9. Summary of the machine learning part

In the section 5, the work done on creating a machine learning model for prediction of the detonation cell size of biogas-oxygen mixtures was presented. In the subsection 5.1 popular metrics used for assessing the quality of model fit were introduced, followed by the description of feature engineering and cross validation techniques in subsections 5.2 and 5.3, respectively. In the subsections 5.4 ÷ 5.7 the three types of models were introduced and their results were presented. The type of trained models were as follows: linear regression, support vector regression and neural network. In case of LR and SVR, they were trained and tested on both aggregated and raw datasets while NN was trained only on the raw data. This was because it

was overfitting when trained using aggregated data. It was shown that all of the models give very good and comparable results with SVR edging slightly ahead. Additionally, when models were tested on raw data it was concluded that there is a limit on model's performance due to the natural variability present in the gathered data. Another important conclusion was that it is possible to create a good quality model using average cell sizes, however it must be highlighted that a good quality of the data must be assured. Finally, in the subsection 5.8 the discussion of the limitations of the machine learning approach was provided. A description of common problems and issues encountered when training a model is given. At the end, these topics are put into perspective by relating them to the process of developing the ML biogas-oxygen models described in the previous subsections.

# 6. Summary and conclusions

Detonation cell size is one of the most important parameters describing the detonation process. It is formed by the intersection of the incident shock, Mach stem and transverse shock that form the detonation wave structure. The point where all three waves collide is called a ‘triple-point’ and its movement outlines the well-known diamond-shaped pattern known as the detonation cell. The width of that cell is used both in theoretical and practical applications. In case of the former it is because it correlates well with other length scales that are used to describe the detonation process. In case of the practical applications, detonation cell size is used both in safety analyses as well as in design process of a detonation combustion chamber. Despite many years of research there is no one, single theory or formula that would be able to explain and predict a detonation cell size for a wide range of different fuels, oxidizers and dilutants. This is why, researchers have been studying this topic, both experimentally and numerically for almost 100 years now. Recently, a third way of study emerged, thanks to the rapid development of machine learning methods that allow to find new, non-obvious relations in the data that could not be found otherwise.

In this thesis, the author presented his work focused on confirming the thesis that it is possible to create a machine learning model that allows to predict the detonation cell size of biogas-oxygen mixtures with satisfying accuracy. In order to achieve that, the following steps were required

- design and build an experimental stand for gathering the measurements of the biogas – oxygen detonation cell size;
- performing the experiments, gathering and analyzing the measurements;
- creating and validating the machine learning models for predicting the detonation cell size.

In the first part the experimental stand was designed, built and tested. Its main part was the stainless-steel detonation tube with an inner dimeter of 122.2 mm, a total length of 4718 mm and a volume of 54.7 $dm^3$. The tube was divided into 4 sections: driver, driven, test and dumping section. Additionally, the auxiliary systems were as follows: ignition system, data acquisition system, filling and evacuating system and a separate stand for mixture preparation.

In the second part, an extensive experimental campaign was conducted. During the experiments over 380 experiments were conducted, including testing the test stand. The parameters that were changed during the campaign were as follows:

- initial pressure $p_0$ [bar]: {0.6; 0.7; 0.8; 0.9; 1.0; 1.2; 1.4; 1.6};
- equivalence ratio $\phi$: {0.5; 0.75; 1.0; 1.25; 1.5}
- biogas composition: {70-30; 65-35; 60-40; 55-45; 50-50; 45-55; 40-60}

For biogas compositions between 70-30 and 50-50 all of the combinations of all three parameters were tested. In case of the compositions 45-55 and 40-60 only the experiments were conducted only for $\phi$ = 1and selected pressures because it was not possible to achieve stable detonation in all conditions, for those two biogas compositions. In total, over 200 unique cases were researched that resulted in over 35 000 cell measurements. The measurements were gathered using a well-known smoked foil technique. After the experiment the foil was carefully removed and photographed. The cells were then marked using the AUTOCAD software. This method made it possible to gather such a large amount of measurements.

During the experimental campaign the first parameter that was analyzed was the detonation velocity. In order to calculate it, the time difference of a detonation wave arrival at the position of two consecutive pressure sensor was divided by the known distance between them. It was shown that for almost all of the cases the calculated velocity was withing ± 2% difference range from the theoretical Chapman - Jouguet detonation velocity that was calculated using NASA CEA software. It was also observed that for the lower initial pressures it looked like the software tended to overpredict the detonation velocity. This was concluded because the calculated theoretical velocities were higher than the experimental ones for the lower pressures in methane content groups. In the next step, the relationships between the detonation cell size and the three researched parameters were studied. It was proved that the in the tested ranges of those parameters the relationships were as follows:

- logarithmic for $p_0$,
- quadratic for equivalence ratio $\phi$,
- linear for methane content in the biogas (which is equivalent to biogas composition).

The detonation cell size decreased when either initial pressure or methane content were increased, in logarithmic and linear fashion, respectively. In case of the equivalence ratio the minimum value of the cell size was recorded for the $\phi$ = 1. When the equivalence ratio moved

away from 1, either towards lean or reach mixture, the detonation cell size increased. It is important to note that those relationships for each of the parameters were seen when the other two were kept constant. Overall in the entire campaign, the average detonation cell size ranged from around 5 to over 50 mm with the coefficient of variation (standard deviation divided by sample's mean) oscillating around 17%.

What is more, the relationships between the ZND induction length and stability parameter $\chi$ (using Ng's definition), and the three parameters were studied. It was shown that there is a linear correlation between the calculated ZND induction length and the detonation cell. Additionally, the induction length increases with decreasing initial pressure and methane percentage. In case of the equivalence the dependency is similar to that of the detonation cell size, it is minimal for $\phi = 1$ and increases when the value of $\phi$ moves away from 1. As mentioned earlier, aside from the ZND induction length, a stability parameter $\chi$, using Ng's definition was also calculated. It was shown that it decreases when the initial pressure or the methane content is increased but in case of equivalence ratio it takes the maximum value for $\phi = 0.75$ and decreases when moving away from it. Despite the name, the higher the value of $\chi$ the more unstable the detonation cellular structure is. The most important observation was that for all cases the value of the stability parameter was well above the stability curve plotted by Ng which means that structure was highly unstable. This was confirmed during the process of measuring the cell sizes as it was clearly visible on soot foils used to record the detonation cells.

Finally, an extensive statistical analysis of the measured detonation cell size distribution was provided. It was shown that a number of measurements per case varied significantly, starting from around 10 and ending at 1001, for one of the cases. However, 75% of the data fell between 0 and around 225 data points with median and mean being 122 and 168, respectively. This of course had an effect on the standard error of the mean (SEM) and coefficient of variation (CV). Nevertheless, the gathered data was of a very good quality in almost of cases with the SEM below 0.5 for 75% of the cases and below 1 for over 90% of the cases. There were some outliers with SEM reaching up to 3. Those very only singular cases in which the number of measurements was very limited due to very irregular structure and huge cells. They were observed for mixtures with a very low initial pressure and low methane content. It is important to note that for those cases the quality of the data was not that good. In order to increase it a detonation tube with higher diameter would be needed as only repeating the experiment multiple times would not be sufficient. This is because, due to the cell size the tube diameter starts to interact with the structure of the detonation. It is also important to note, that another

source of the cell size measurement was the human factor. A human judgement when selecting the cell corners and precision when marking them also play an important part that influence the quality of the data gathered from the experiments. It is, however, very hard to quantify the error introduced by the human factor and it was not done in the presented work. Nevertheless, the steps were taken to minimize the influence of that source of an error. The measurements were double-checked and only the well visible cells were marked. One last, but not least, observation that should be mentioned, was the fact that a presumed limit value of the CV was discovered. It was noted, that when the number of measurement per case increased, the values of CV seemed to tend towards a constant value of around 17%. However, as this was not the topic of this thesis it was not researched in details. Nevertheless, it might be an interesting direction for a future study.

The experimental part of the work, presented above, provided a valuable view on the detonation cell size distribution of biogas-oxygen mixture and laid the foundations for the next part.

In the final section, machine learning methods were utilized to train and verify models for predicting the size of detonation cells using the three parameters examined in the previous section (p0, $\phi$, and %CH4). First, in addition to techniques such as feature engineering and cross-validation, the customary metrics for assessing model quality were presented. Following this, the training and validation outcomes for three distinct model types were presented in subsequent subsections. Starting with the simple Linear Regression model, progressing to the more complex Support Vector Regression, and finishing with the widely used Neural Network model. Two versions of each model were developed. One version was trained on the raw cell measurements, while the other was trained on the so-called 'aggregated data'. The aggregated data refers to the calculation of the average cell size for each unique case. A 'case' is defined as a unique combination of the three parameters. This average cell size was then used to train the model. It is important to note that, prior to model training, the dataset was divided into a training and testing set. The training set was then used to train the model while the testing set was reserved exclusively for evaluation purposes. This was carried out to prevent overfitting and to effectively assess the model's accuracy.

The created models were then tested on the corresponding test set consisting of either raw or aggregated data. Additionally, they were also cross-tested on the other test set, meaning that the model trained on raw data was also tested on aggregated data, and vice versa. This was

done in order to check if they can be used to predict using the other type of data. What is more, when the models were tested on the raw data, the results were showed with and without taking into consideration the distributions of the cell sizes.

The most important observation was that all of the models gave very good results with the $R^2$ parameter well above 90% and 84% in case of the aggregated and raw test set, respectively . The best results were given by the SVR, however, the results did not vary significantly, and the differences in, for example, $R^2$ metric were on the level of 1-3%. What is more, the LR model outputted easy to interpret equations that showed an approximated influence of each of the parameters used in the model on the detonation cell size when all the other parameters are kept constant. It is worth noting, that because the differences between the models were not big, the relationships between parameters and cell size shown by the LR model, can be assumed to be close to the truth.

It was also shown that, a model trained on the aggregated data was able to predict well both in case of the aggregated and raw test set. This is an important observation as usually researchers might not have access to the raw data from the experiments other than their own. If they want to expand their dataset using the literature they are typically forced to use the average data cell that is the most common metric reported in the articles. The conclusion is that they can safely do this and the model should still behave well even if trained on the aggregated data, provided that the data is of a good quality.

An interesting observation was made when the results of testing the models on the raw data test set were compared. It turned out, that there is a limit of a model's performance that, in terms of $R^2$ is around 84%. This limit is the result of the fact that a cell size follows some kind of a distribution, while the model predicts only a single value. This implies, that a discrepancy between the prediction and an actual value is to be expected as there is always a variability in the measured cell size. However, it was also shown, that when that distribution was taken into account the $R^2$ rose significantly from around 84% to around 97%. This was done by treating the measurements that fall within ±17% from the predicted value as predicted perfectly. This meant that the predictions were transformed from being a single value for a single set of parameter into a range of values.

In the next subsection, curves showing the continuous predictions of the model when one of the parameters is varied, were presented. It was shown that when the values of the parameters, used as model input for prediction, stayed within the ranges of those parameters used during

training, the prediction were good and stable. However, when the value of a predictor fell outside of the training data range, the models became unstable and the predictions could not be trusted. In this section it also became clear why the SVR model gave the best results. The biggest difference between the models was in the predictions of the very big cell sizes, the upper end of the cell size spectrum. When the model curves were plotted, it turned out that, as expected, the SVR thanks to its flexibility was able to fit closely to the training data points. However, this does not mean that those are the correct results because, as mentioned earlier, it was known that that data might not be of the highest quality. Nevertheless, it is important to highlight that it was not the problem with the model itself, it was trained properly and did not show signs of overfitting when tested. The issue was with the data and the fact the an algorithm does not check or 'think' if the data is of good or bad quality, it simply uses it learn. This observations leads to the last part of the presented thesis – the discussion of the limitations of a machine learning approach.

As mentioned, the limitations of the machine learning approach were discussed and the created models were put in that context. There author identified four main limitations of the ML techniques, those are as follows:

- data quality,
- training data range,
- dependency on additional assumptions,
- generalization of the model to other fuels/oxidizers/dilutants.

In case of the data quality, a model cannot and will not be better than the quality of the data it was provided during training. If the training data is poor it will use it to learn and it will predict accordingly.

As to the second bullet, a properly trained model should yield good results if the new data for which it is supposed to predict is withing the range that the model encountered during training. Outside of it, it cannot be trusted. If the data is only slightly outside the range then the model might extrapolate correctly, however it is not guaranteed. The further the new data is from the training data range, the worse the prediction will be. It is especially important limitation to keep in mind, because it is hard to assess and check. This is because a model is usually used to predict for unknown cases so it is not possible to compare to known data. Even if a behavior of a given type of model would on the data outside of the training range would be tested, there is no guarantee that it will hold when the model is trained using different data.

Another important thing to highlight is that if the model is created using parameters that rely on some additionally, outside assumptions those assumptions and errors introduced by them carry over to the model. An example is to use parameters calculated using a chemical reaction kinetics model as a ML model input. There is a large number of different chemical reaction kinetics models that vary from one to another and that are validated for some subset of mixtures and initial conditions. A value of a given parameter, for example activation energy, usually differs between different models. As such, a ML model created using this parameter, automatically becomes limited only to those mixture for which the chemical kinetics model was validated. Additionally, the ML model also inherits the errors coming from the assumptions of that model. In the presented thesis, this problem was avoided by using only the parameters that do not depend on any assumptions and that are easy to either measure or calculate. In that case, the only source of error is the precision of measurement or calculation.

Last but not least, there is the limitation concerning an ability of a model to generalize well to other types of fuels/oxidizers/dilutants than those used for training. To the author's best knowledge a general model that would be able to predict the detonation cell size for any mixture in any initial conditions was not created yet. The main problem that author sees in this area is to find the right set of parameters that would allow to properly differentiate and accommodate different kinds of mixtures. The model created in this thesis uses only basic parameters that are sufficient to predict the detonation cell size for biogas-oxygen mixtures but do not allow generalize for others.

To sum up, the presented work was done in order to either confirm or discard the thesis that it is possible to create a machine learning model for predicting the detonation cell size of biogas-oxygen mixtures with satisfying accuracy. It was shown, that in fact it is possible and with a very good accuracy. What is more, the created models used only the three parameters that are easy to measure or calculate and that do not depend on any assumptions: initial pressure $p_0$, equivalence ratio $\phi$ and methane percentage in the biogas. However, it is important to note that it is also a limitation of the model. This is because those parameters are not sufficient to generalize for other types of fuels, oxidizers and dilutants. Such a general model, provided it would be created properly, and would work well, would be immensely useful for the community of researchers working on the detonation. The author is convinced that the presented work lays a concrete foundation for it and it represents another step in that direction by showing that it is possible to create a model that does not depend on any assumptions. The author strongly believes that it is the correct direction of development. Nevertheless, the question of a correct

set of parameters for such a general model is still open and makes for an interesting topic for further work.

# 7. Bibliography


1. Intergovernmental Panel on Climate Change (IPCC). Ref. Rev. 26, 41–42 (2012). https://doi.org/10.1108/09504121211205250

2. Net Zero Coalition | United Nations, https://www.un.org/en/climatechange/net-zero-coalition

3. Brack, D., Grubb, M., Vrolijk, C.: Kyoto Protocol: a guide and assessment . Royal Institute of International Affairs Energy and Environmental Programme, London, UK (1997)

4. The Paris Agreement | UNFCCC, https://unfccc.int/process-and-meetings/the-paris-agreement/the-paris-agreement

5. Katowice climate package | UNFCCC, https://unfccc.int/process-and-meetings/the-paris-agreement/paris-agreement-work-programme/katowice-climate-package

6. Balta, M.O., Eke, F.: Spatial Reflection of Urban Planning in Metropolitan Areas and Urban Rent; a Case Study of Cayyolu, Ankara. Eur. Plan. Stud. 19, 1817–1838 (2011). https://doi.org/10.1080/09654313.2011.614396

7. REN21: Renewables 2020 Global Status Report. (2020)

8. REN21. 2022: Renewables 2022 Global Status Report. , Paris (2022)

9. Abe, J.O., Popoola, A.P.I., Ajenifuja, E., Popoola, O.M.: Hydrogen energy, economy and storage: Review and recommendation. Int. J. Hydrogen Energy. 44, 15072–15086 (2019). https://doi.org/10.1016/j.ijhydene.2019.04.068

10. Lee, S., Saw, S.H.: Nuclear fusion energy-mankind's giant step forward. J. Fusion Energy. 30, 398–403 (2011). https://doi.org/10.1007/S10894-011-9390-7/FIGURES/5

11. EC Grants: Renewable Energy, https://ec.europa.eu/info/funding-tenders/opportunities/portal/screen/opportunities/topic-search;callCode=null;freeTextSearchKeyword=biogas;matchWholeText=true;typeCodes=1,0;statusCodes=31094501,31094502,31094503;programmePeriod=null;programCcm2Id=null;pr

12. European Technology and Innovation Platform: Biogas, https://www.etipbioenergy.eu/value-chains/products-end-use/products/biogas

13. European Biogas Association: European Biogas Association, https://www.europeanbiogas.eu/about-biogas-and-biomethane/, (2021)

14. IEA – International Energy Agency, https://www.iea.org/

15. American Biogas Council: American Biogas Council, https://americanbiogascouncil.org/

16. Sarker, S.A., Wang, S., Adnan, K.M.M., Sattar, M.N.: Economic feasibility and determinants of biogas technology adoption: Evidence from Bangladesh. Renew. Sustain. Energy Rev. 123, 109766 (2020). https://doi.org/10.1016/J.RSER.2020.109766

17. Khalil, M., Berawi, M.A., Heryanto, R., Rizalie, A.: Waste to energy technology: The potential of sustainable biogas production from animal waste in Indonesia. Renew. Sustain. Energy Rev. 105, 323–331 (2019). https://doi.org/10.1016/J.RSER.2019.02.011

18. Toklu, E.: Biomass energy potential and utilization in Turkey. Renew. Energy. 107, 235–244 (2017). https://doi.org/10.1016/J.RENENE.2017.02.008

19. AKYÜREK, Z.: Potential of biogas energy from animal waste in the Mediterranean Region of Turkey. J. Energy Syst. 2, 160–167 (2018). https://doi.org/10.30521/JES.455325

20. Benato, A., Macor, A.: Italian biogas plants: Trend, subsidies, cost, biogas composition and engine emissions. Energies. 12, (2019). https://doi.org/10.3390/en12060979

21. Hosseini, S.E., Wahid, M.A.: Feasibility study of biogas production and utilization as a source of renewable energy in Malaysia, (2013)

22. Mahmudul, H.M., Rasul, M.G., Akbar, D., Mofijur, M.: Opportunities for solar assisted biogas plant in subtropical climate in Australia: A review. Energy Procedia. 160, 683–690 (2019). https://doi.org/10.1016/J.EGYPRO.2019.02.192

23. Koryś, K.A., Latawiec, A.E., Grotkiewicz, K., Kuboń, M.: The Review of Biomass Potential for Agricultural Biogas Production in Poland. Multidisciplinary Digital Publishing Institute (2019)

24. Mao, G., Huang, N., Chen, L., Wang, H.: Research on biomass energy and environment from the past to the future: A bibliometric analysis. Sci. Total Environ. 635, 1081–1090 (2018). https://doi.org/10.1016/J.SCITOTENV.2018.04.173

25. Baccioli, A., Antonelli, M., Frigo, S., Desideri, U., Pasini, G.: Small scale bio-LNG plant: Comparison of different biogas upgrading techniques. Appl. Energy. 217, 328–335 (2018). https://doi.org/10.1016/j.apenergy.2018.02.149

26. International Energy Agency: Outlook for biogas and biomethane. Prospects for organic growth. IEA Publ. 1–93 (2020)

27. Abbasi, T., Tauseef, S.M., Abbasi, S.A.: Biogas Energy. Springer New York, New York, NY (2012)

28. Sun, Q., Li, H., Yan, J., Liu, L., Yu, Z., Yu, X.: Selection of appropriate biogas upgrading technology-a review of biogas cleaning, upgrading and utilisation, (2015)

29. Rodrigues, M., Walter, A., Faaij, A.: Co-firing of natural gas and biomass gas in biomass integrated gasification/combined cycle systems. Energy. 28, 1115–1131 (2003). https://doi.org/10.1016/S0360-5442(03)00087-2

30. Chapman, D.L.: VI.On the rate of exlosion in gases. Philos. Mag. Ser. 5. 47, 90–104 (1899)

31. Jouguet, E.: Sur la propagation des reactions chimiques dans les gaz [On the propagation of chemical reactions in gases]. J. Math. Pures Appl. 6, 347–425 (1905)

32. Kuo, K.K.: Princeples of Combustion. John Wiley & Sons, Inc., New Jersey (2005)

33. Zel'dovich, Y.B.: The Theory of the Propagation of Detonation in Gaseous Systems. Theor.Phys. SSSR. 10, (1940)

34. von Neumann, J.: Theory of Detonation Waves. Inst. Adv. Study Princet. NJ. (1942)

35. Döring, W.: Über den Detonationivorgang in Gasen. Ann. Phys. Lpz. 43, 421–436 (1943)

36. Shepherd, J.E.E.: Detonation in gases. Proc. Combust. Inst. 32, 83–98 (2009). https://doi.org/10.1016/J.PROCI.2008.08.006

37. Lee, J.H.S., Radulescu, M.I.: On the hydrodynamic thickness of cellular detonations, https://link.springer.com/article/10.1007/s10573-005-0084-1, (2005)

38. Teodorczyk, A., Lee, J.H.S.: Detonation attenuation by foams and wire meshes lining the walls. Shock Waves. 4, 225–236 (1995). https://doi.org/10.1007/BF01414988

39. Radulescu, M.I., Lee, J.H.S.: The failure mechanism of gaseous detonations: experiments in porous wall tubes. Combust. Flame. 131, 29–46 (2002). https://doi.org/10.1016/S0010-2180(02)00390-5

40. Zhang, B.: The influence of wall roughness on detonation limits in hydrogen–oxygen mixture. Combust. Flame. 169, 333–339 (2016). https://doi.org/10.1016/J.COMBUSTFLAME.2016.05.003

41. Wolanski, P.: Detonative propulsion. Proc. Combust. Inst. 34, 125–158 (2013). https://doi.org/10.1016/J.PROCI.2012.10.005

42. O., M.I.: Detonation Length Scales for Fuel-Air Explosives. Prog. Astro. Aero. 94, 55–79 (1984)

43. Lee, J.H.S.: Dynamic Parameters of Gaseous Detonations. http://dx.doi.org/10.1146/annurev.fl.16.010184.001523. 16, 311–336 (2003). https://doi.org/10.1146/ANNUREV.FL.16.010184.001523

44. Dorofeev, S.B., Sidorov, V.P., Kuznetsov, M.S., Matsukov, I.D., Alekseev, V.I.: Effect of scale on the onset of detonations. Shock Waves. 10, 137–149 (2000). https://doi.org/10.1007/S001930050187/METRICS

45. Benedick, W.B., Guirao, C.M., Knystautas, R., Lee, J.H.: Critical charge for the direct initiation of detonation in gaseous fuel-air mixtures. Prog. Astronaut. Aeronaut. 106, 181–202 (1986)

46. R., K.: Measurement of Cell Size in Hydrocarbon-air Mixtures and Predictions of Critical Tube Diameter, Critical Initiation Energy and Detonability Limits. Prog. Astronaut. Aeronaut. 94, 23–37 (1984). https://doi.org/10.20619/JCOMBSJ.50.152_152

47. Westbrook, C.K., Urtiew, P.A.: Chemical kinetic prediction of critical parameters in gaseous detonations. Symp. Combust. 19, 615–623 (1982). https://doi.org/10.1016/S0082-0784(82)80236-1

48. Kindracki, J., Wolanski, P., Gut, Z.: Experimental research on the rotating detonation in gaseous fuels-oxygen mixtures. Shock Waves. 21, 75–84 (2011). https://doi.org/10.1007/s00193-011-0298-y

49. Kindracki, J.: Badania eksperymentalne i symulacje numeryczne procesu wirującej detonacji gazowej [Experimental research and numerical calculation of the rotating

detonatino] (in polish), (2008)

50. Xie, Q., Wen, H., Li, W., Ji, Z., Wang, B., Wolanski, P.: Analysis of operating diagram for H2/Air rotating detonation combustors under lean fuel condition. Energy. 151, 408–419 (2018). https://doi.org/10.1016/j.energy.2018.03.062

51. Bykovskii, F.A., Zhdan, S.A., Vedernikov, E.F.: Continuous spin detonation of synthesis gas-air mixtures. Combust. Explos. Shock Waves. 49, 435–441 (2013). https://doi.org/10.1134/S0010508213040060

52. Bykovskii, F.A., Zhdan, S.A., Vedernikov, E.F., Samsonov, A.N.: Effect of combustor geometry on continuous spin detonation in syngas–air mixtures. Combust. Explos. Shock Waves. 51, 688–699 (2015). https://doi.org/10.1134/S0010508215060106

53. Bykovskii, F.A., Zhdan, S.A., Vedernikov, E.F., Samsonov, A.N.: Scaling factor in continuous spin detonation of syngas–air mixtures. Combust. Explos. Shock Waves. 53, 187–198 (2017). https://doi.org/10.1134/S0010508217020095

54. Wang, L., Ma, H., Shen, Z., Xue, B., Cheng, Y., Fan, Z.: Experimental investigation of methane-oxygen detonation propagation in tubes. Appl. Therm. Eng. 123, 1300–1307 (2017). https://doi.org/10.1016/j.applthermaleng.2017.05.045

55. Lefebvre, A.H.: Gas Turbine Combustion. 1–400 (1999)

56. Schwer, D.A., Kailasanath, K.: Characterizing NOx emissions for air-breathing rotating detonation engines. 52nd AIAA/SAE/ASEE Jt. Propuls. Conf. 2016. 1–13 (2016). https://doi.org/10.2514/6.2016-4779

57. Prisacariu, V., Rotaru, C., Cîrciu, I., Niculescu, M.: Numerical simulation and performances evaluation of the pulse detonation engine. MATEC Web Conf. 234, 01001 (2018). https://doi.org/10.1051/matecconf/201823401001

58. Debnath, P., Pandey, K.M.: Computational Study of Deflagration to Detonation Transition in Pulse Detonation Engine Using Shchelkin Spiral. Appl. Mech. Mater. 772, 136–140 (2015). https://doi.org/10.4028/www.scientific.net/AMM.772.136

59. Heiser, W.H., Pratt, D.T.: Thermodynamic Cycle Analysis of Pulse Detonation Engines. J. Propuls. Power. 18, 68–76 (2002). https://doi.org/10.2514/2.5899

60. Eidelman, S., Grossmann, W., Lottati, I.: Review of propulsion applications and

numerical simulations of the pulsed detonation engine concept. J. Propuls. Power. 7, 857–865 (1991). https://doi.org/10.2514/3.23402

61. Matsuoka, K., Esumi, M., Ikeguchi, K.B., Kasahara, J., Matsuo, A., Funaki, I.: Optical and thrust measurement of a pulse detonation combustor with a coaxial rotary valve. Combust. Flame. 159, 1321–1338 (2012). https://doi.org/10.1016/j.combustflame.2011.10.001

62. Kasahara, J., Arai, T., Matsuo, A.: Experimental analysis of Pulse Detonation Engine performance by pressure and momentum measurements. In: 41st Aerospace Sciences Meeting and Exhibit (2003)

63. Larine Barr: Pulsed detonation engine flies into history , https://www.af.mil/News/Article-Display/Article/123534/pulsed-detonation-engine-flies-into-history/

64. Nejaamtheen, M.N., Kim, J.-M., Choi, J.-Y.: Review on the Research Progresses in Rotating Detonation Engine. In: Jiun-Ming, L., Chiang, J.T., Boo, C.K., Jian-Ping, W., and Cheng, W. (eds.) Detonation Control for Propulsion. pp. 109–159. Springer, Cham (2018)

65. Zhang, S., Zhang, L., Yao, S., Wang, J.: Numerical Investigation on Continuous Detonation Engine with Varying Equivalence Ratios. In: 53rd AIAA/SAE/ASEE Joint Propulsion Conference. American Institute of Aeronautics and Astronautics, Reston, Virginia (2017)

66. Schwer, D., Kailasanath, K.: Numerical Study of the Effects of Engine Size n Rotating Detonation Engines. In: 49th AIAA Aerospace Sciences Meeting including the New Horizons Forum and Aerospace Exposition. American Institute of Aeronautics and Astronautics, Reston, Virigina (2011)

67. Meng, Q., Zhao, N., Zheng, H., Yang, J., Li, Z., Deng, F.: A numerical study of rotating detonation wave with different numbers of fuel holes. Aerosp. Sci. Technol. 93, (2019). https://doi.org/10.1016/j.ast.2019.105301

68. Bykovskii, F.A., Zhdan, S.A., Vedernikov, E.F.: Continuous Spin Detonation in Annular Combustors. Combust. Explos. Shock Waves. 41, 449–459 (2005). https://doi.org/10.1007/s10573-005-0055-6

69. Kindracki, J.: Badania eksperymentalne i symulacje numeryczne procesu inicjacji wirują cej detonacji gazowej., (2008)

70. Okninski, A., Kindracki, J., Wolanski, P.: Rocket rotating detonation engine flight demonstrator. Aircr. Eng. Aerosp. Technol. 88, 480–491 (2016). https://doi.org/10.1108/AEAT-07-2014-0106

71. Kindracki, J.: Experimental research on rotating detonation in liquid fuel–gaseous air mixtures. Aerosp. Sci. Technol. 43, 445–453 (2015). https://doi.org/10.1016/j.ast.2015.04.006

72. Kindracki, J., Siatkowski, S., Lukasik, B.: Influence of Inlet Flow Parameters on Rotating Detonation. AIAA J. 58, 5046–5051 (2020). https://doi.org/10.2514/1.J058152

73. Kawalec, M., Perkowski, W., Łukasik, B., Bilar, A., Wolański, P.: Applications of the continuously rotating detonation to combustion engines at the Łukasiewicz - Institute of Aviation. Combust. Engines. R. 61, nr 4, (2022). https://doi.org/10.19206/CE-145409

74. Redhal, S.C., Burr, J.R., Yu, K.H.: Injector flowfield-detonation wave interaction in unwrapped RDE channel. AIAA Propuls. Energy Forum Expo. 2019. (2019). https://doi.org/10.2514/6.2019-4216

75. Redhal, S., Burr, J., Yu, K.H.: Fuel injection dynamics and detonation wave interaction in rectangular channel. AIAA Scitech 2019 Forum. (2019). https://doi.org/10.2514/6.2019-2251

76. Kubat, M.: An Introduction to Machine Learning. Springer International Publishing, Cham (2017)

77. Graham, S.A., Lee, E.E., Jeste, D. V., Van Patten, R., Twamley, E.W., Nebeker, C., Yamada, Y., Kim, H.C., Depp, C.A.: Artificial intelligence approaches to predicting and detecting cognitive decline in older adults: A conceptual review. Psychiatry Res. 284, 112732 (2020). https://doi.org/10.1016/J.PSYCHRES.2019.112732

78. Graham, S., Depp, C., Lee, E.E., Nebeker, C., Tu, X., Kim, H.-C., Jeste, D. V.: Artificial Intelligence for Mental Health and Mental Illnesses: an Overview. Curr. Psychiatry Rep. 21, 116 (2019). https://doi.org/10.1007/s11920-019-1094-0

79. Çallı, E., Sogancioglu, E., van Ginneken, B., van Leeuwen, K.G., Murphy, K.: Deep learning for chest X-ray analysis: A survey. Med. Image Anal. 72, 102125 (2021).

https://doi.org/10.1016/J.MEDIA.2021.102125

80. Xie, Y., Li, X., Ngai, E.W.T., Ying, W.: Customer churn prediction using improved balanced random forests. Expert Syst. Appl. 36, 5445–5449 (2009). https://doi.org/10.1016/J.ESWA.2008.06.121

81. Spanoudes, P., Nguyen, T.: Deep Learning in Customer Churn Prediction: Unsupervised Feature Learning on Abstract Company Independent Feature Vectors. (2017). https://doi.org/10.48550/arxiv.1703.03869

82. Aslam, U., Aziz, H.I.T., Sohail, A., Batcha, N.K.: An empirical study on loan default prediction models. J. Comput. Theor. Nanosci. 16, 3483–3488 (2019). https://doi.org/10.1166/JCTN.2019.8312

83. Stein, R.M.: Benchmarking default prediction models: pitfalls and remedies in model validation. J. Risk Model Valid. 1, 77–113 (2007)

84. Wu, H., Liu, X., An, W., Chen, S., Lyu, H.: A deep learning approach for efficiently and accurately evaluating the flow field of supercritical airfoils. Comput. Fluids. 198, 104393 (2020). https://doi.org/10.1016/J.COMPFLUID.2019.104393

85. Sekar, V., Khoo, B.C.: Fast flow field prediction over airfoils using deep learning approach. Phys. Fluids. 31, 057103 (2019). https://doi.org/10.1063/1.5094943

86. Fan, C., Sun, Y., Zhao, Y., Song, M., Wang, J.: Deep learning-based feature engineering methods for improved building energy prediction. Appl. Energy. 240, 35–45 (2019). https://doi.org/10.1016/J.APENERGY.2019.02.052

87. James, G., Witten, D., Hastie, T., Tibshirani, R.: An Introduction to Statistical Learning with Applications in R. Springer Science+Business Media, New York, NY (2017)

88. Dairobi, A.G., Wahid, M.A., Inuwa, I.M.: Feasibility Study of Pulse Detonation Engine Fueled by Biogas. Appl. Mech. Mater. 388, 257–261 (2013). https://doi.org/10.4028/www.scientific.net/AMM.388.257

89. Saqr, K.M., Kassem, H.I., Sies, M.M., Wahid, M.A.: Ideal detonation characteristics of biogas-hydrogen and -hydrogen peroxide mixtures. Int. Conf. Theor. Appl. Mech. Int. Conf. Fluid Mech. Heat Mass Transf. - Proc. 69–72 (2010)

90. Wahid, M.A., Ujir, H.: Reacting shock waves characteristics for biogas compared to

other gaseous fuel. In: AIP Conference Proceedings. pp. 90–99 (2012)

91. Rahman, M.N., Ujir, M.H., Wahid, M.A., Yasin, M.F.M.: A single-step chemistry mechanism for biogas supersonic combustion velocity with nitrogen dilution. J. Therm. Anal. Calorim. 1–15 (2022). https://doi.org/10.1007/s10973-022-11356-x

92. Elhawary, S., Saat, A., Wahid, M.A., Ghazali, A.D.: Experimental study of using biogas in Pulse Detonation Engine with hydrogen enrichment. Int. J. Hydrogen Energy. 45, 15414–15424 (2020). https://doi.org/10.1016/j.ijhydene.2020.03.246

93. Wahid, M.A., Ujir, H., Saqr, K.M., Sies, M.M.: Experimental Study of Confined Biogas Pulse Detonation Combustion. In: The 2nd International Meeting on Advances in Thermo-Fluids. pp. 71–77 (2009)

94. Siatkowski, S., Wacko, K., Kindracki, J.: Experimental research on detonation cell size of a purified biogas-oxygen mixture. Energies. 14, (2021). https://doi.org/10.3390/en14206605

95. Siatkowski, S., Wacko, K., Kindracki, J.: Extensive study on the detonation cell size of biogas-oxygen mixtures. Fuel. 344, 128016 (2023). https://doi.org/10.1016/J.FUEL.2023.128016

96. Chemical Equilibrium with Applications - Glenn Research Center | NASA, https://www1.grc.nasa.gov/research-and-engineering/ceaweb/

97. Zheng, Z.-H., Lin, X.-D., Yang, M., He, Z.-M., Bao, E., Zhang, H., Tian, Z.-Y.: Progress in the Application of Machine Learning in Combustion Studies. ES Energy Environ. 9, 1–15 (2020). https://doi.org/10.30919/esee8c795

98. Zhou, L., Song, Y., Ji, W., Wei, H.: Machine learning for combustion. Energy AI. 7, 100128 (2022). https://doi.org/10.1016/j.egyai.2021.100128

99. Gavrikov, A.. I., Efimenko, A.. A., Dorofeev, S.. B.: A model for detonation cell size prediction from chemical kinetics. Combust. Flame. 120, 19–33 (2000). https://doi.org/10.1016/S0010-2180(99)00076-0

100. Schelkin, K.I., Troshin, Y.K.: Gasdynamics of Combustion. Mono Book Corp., Baltimore (1965)

101. Kee, R.J., Miller, J.A., Jefferson, T.H.: CHEMKIN: a general-purpose, problem-

independent, transportable, FORTRAN chemical kinetics code package, http://inis.iaea.org/Search/search.aspx?orig_q=RN:11548068, (1980)

102. Kaneshige, M., Shepherd, J.E.: Detonation Database. Technical Report FM97-8, GALCIT, July 1997, https://shepherd.caltech.edu/detn_db/html/db.html

103. Malik, K., Żbikowski, M., Teodorczyk, A.: Detonation cell size model based on deep neural network for hydrogen, methane and propane mixtures with air and oxygen. Nucl. Eng. Technol. 51, 424–431 (2019). https://doi.org/10.1016/j.net.2018.11.004

104. Goodwin, D.G., Moffat, H.K., Schoegl, I., Speth, R.L., Weber, B.W.: Cantera: An Object-Oriented Software Toolkit for Chemical Kinetics, Thermodynamics, and Transport Processes, https://www.cantera.org, (2022)

105. Yu, J., Hou, B., Lelyakin, A., Xu, Z., Jordan, T.: Gas detonation cell width prediction model based on support vector regression. Nucl. Eng. Technol. 49, 1423–1430 (2017). https://doi.org/10.1016/j.net.2017.06.014

106. Bakalis, G., Valipour, M., Bentahar, J., Kadem, L., Teng, H., Ng, H.D.: Detonation cell size prediction based on artificial neural networks with chemical kinetics and thermodynamic parameters. Fuel Commun. 14, 100084 (2023). https://doi.org/10.1016/j.jfueco.2022.100084

107. Ng, H.D., Radulescu, M.I., Higgins, A.J., Nikiforakis, N., Lee, J.H.S.: Numerical investigation of the instability for one-dimensional Chapman-Jouguet detonations with chain-branching kinetics. Combust. Theory Model. 9, 385–401 (2005). https://doi.org/10.1080/13647830500307758

108. Ng, H.D.: The effect of chemical reaction kinetics on the structure of gaseous detonations, (2005)

109. NG, H., JU, Y., LEE, J.: Assessment of detonation hazards in high-pressure hydrogen storage from chemical sensitivity analysis. Int. J. Hydrogen Energy. 32, 93–99 (2007). https://doi.org/10.1016/j.ijhydene.2006.03.012

110. A., K.A.: Detailed reaction mechanism for small hydrocarbons combustion. http://homepages.vub.ac.be/〜akonnov/. (1998). https://doi.org/10.20619/JCOMBSJ.50.152_152

111. Zhang, Y., Zhou, L., Meng, H., Teng, H.: Reconstructing cellular surface of gaseous

detonation based on artificial neural network and proper orthogonal decomposition. Combust. Flame. 212, 156–164 (2020). https://doi.org/10.1016/J.COMBUSTFLAME.2019.10.031

112. Zhou, L., Teng, H., Ng, H.D., Yang, P., Jiang, Z.: Reconstructing shock front of unstable detonations based on multi-layer perceptron. Acta Mech. Sin. 37, 1610–1623 (2021). https://doi.org/10.1007/s10409-021-01130-x

113. Zhang, Y., Zhou, L., Gong, J., Ng, H.D., Teng, H.: Effects of activation energy on the instability of oblique detonation surfaces with a one-step chemistry model. Phys. Fluids. 30, 106110 (2018). https://doi.org/10.1063/1.5054063/991223

114. Bian, J., Zhou, L., Yang, P., Teng, H., Ng, H.D.: A reconstruction method of detonation wave surface based on convolutional neural network. Fuel. 315, 123068 (2022). https://doi.org/10.1016/j.fuel.2021.123068

115. Johnson, K.B., Ferguson, D.H., Tempke, R.S., Nix, A.C.: Application of a Convolutional Neural Network for Wave Mode Identification in a Rotating Detonation Combustor Using High-Speed Imaging. In: Volume 4B: Combustion, Fuels, and Emissions. American Society of Mechanical Engineers (2020)

116. Johnson, K., Ferguson, D.H., Nix, A.C.: Individual Wave Detection and Tracking within a Rotating Detonation Engine through Computer Vision Object Detection applied to High-Speed Images. In: AIAA Scitech 2021 Forum. pp. 1–15. American Institute of Aeronautics and Astronautics, Reston, Virginia (2021)

117. Johnson, K.B., Ferguson, D.H., Tempke, R.S., Nix, A.C.: Application of a Convolutional Neural Network for Wave Mode Identification in a Rotating Detonation Combustor Using High-Speed Imaging. J. Therm. Sci. Eng. Appl. 13, (2021). https://doi.org/10.1115/1.4049868

118. Johnson, K., Ferguson, D.H., Nix, A.C.: Time Series Classification within a Rotating Detonation Engine through Deep Convolutional Neural Networks applied to High-Speed Pressure Data. In: AIAA SCITECH 2022 Forum. American Institute of Aeronautics and Astronautics, Reston, Virginia (2022)

119. Johnson, K., Ferguson, D.H., Nix, A.C.: Survey of Machine Learning Based RDE Diagnostics: Evaluation and Comparison for Broad Application in Experimental Facilities. In: AIAA SCITECH 2023 Forum. American Institute of Aeronautics and

Astronautics, Reston, Virginia (2023)

120. Wolff, S., Schäpel, J.-S., King, R.: Application of Artificial Neural Networks for Misfiring Detection in an Annular Pulsed Detonation Combustor Mockup. In: Volume 6: Ceramics; Controls, Diagnostics and Instrumentation; Education; Manufacturing Materials and Metallurgy. American Society of Mechanical Engineers (2016)

121. Barwey, S., Prakash, S., Hassanaly, M., Raman, V.: Data-driven Classification and Modeling of Combustion Regimes in Detonation Waves. Flow, Turbul. Combust. 106, 1065–1089 (2021). https://doi.org/10.1007/s10494-020-00176-4

122. Ryu, J.I.: Applying machine learning techniques to predict detonation initiation from hot spots. Energy AI. 9, 100163 (2022). https://doi.org/10.1016/J.EGYAI.2022.100163

123. Zeldovich, Y.B.: Regime classification of an exothermic reaction with nonuniform initial conditions. Combust. Flame. 39, 211–214 (1980). https://doi.org/10.1016/0010-2180(80)90017-6

124. Zel'dovich, Y.B., Librovich, V.B., Makhviladze, G.M., Sivashinsky, G.I.: On the development of detonation in a non-uniformly preheated gas. Astronaut. Acta. 15, 313–321 (1970)

125. Tieszen, S.R., Stamps, D.W., Westbrook, C.K., Pitz, W.J.: Gaseous Hydrocarbon-Air Detonations. Combust. Flame. 84, 376–390 (1991). https://doi.org/10.1016/0010-2180(91)90013-2

126. Schumaker, S.A., Knisely, A.M., Hoke, J.L., Rein, K.D.: Methane-oxygen detonation characteristics at elevated pre-detonation pressures. In: Proceedings of the Combustion Institute. pp. 3623–3632. Elsevier Ltd (2021)

127. Diakow, P., Cross, M., Ciccarelli, G.: Detonation characteristics of dimethyl ether and ethanol–air mixtures. Shock Waves. 25, 231–238 (2015). https://doi.org/10.1007/s00193-015-0554-7

128. Pintgen, F., Austin, J.M., Shepherd, J.E.: Detonation Front Structure: Variety and Characterization. In: Roy, G.D., Frolov, S.M., Santoro, R.J., and Tsyganov, S.A. (eds.) Confined Detonations and Pulse Detonation Engines. pp. 105–116. TORUS PRESS Ltd., Moscow, Russia (2003)

129. "Chemical-Kinetic Mechanisms for Combustion Applications", San Diego Mechanism

web page, Mechanical and Aerospace Engineering (Combustion Research), University of California at San Diego, http://combustion.ucsd.edu

130. Explosion Dynamics Laboratory, https://shepherd.caltech.edu/EDL/PublicResources/sdt/

131. Westbrook, C.K., Urtiew, P.A.: Use of chemical kinetics to predict critical parameters of gaseous detonations. Combust. Explos. Shock Waves. 19, 753–766 (1983). https://doi.org/10.1007/BF00750785

132. Radulescu, M.I., Sharpe, G.J., Bradley, D.: A Universal Parameter Quantifying Explosion Hazards, Detonability and Hot Spot Formation: The $\chi$ Number. In: researchgate.net. pp. 617–626 (2013)

133. Wassertheil-Smoller, S.: Biostatistics and Epidemiology: A Primer for Health Professionals. Springer New York (2013)

134. MATLAB - MathWorks, https://www.mathworks.com/products/matlab.html

135. Python Programming Language, https://www.python.org/

136. R: The R Project for Statistical Computing, https://www.r-project.org/

137. Pedregosa, F., Varoquaux, G., Gramfort, A., Michel, V., Thirion, B., Grisel, O., Blondel, M., Prettenhofer, P., Weiss, R., Dubourg, V., Vanderplas, J., Passos, A., Cournapeau, D., Brucher, M., Perrot, M., Duchesnay, E.: Scikit-learn: Machine Learning in {P}ython. J. Mach. Learn. Res. 12, 2825–2830 (2011)

138. Smola, A.J., Schölkopf, B.: A tutorial on support vector regression. Stat. Comput. 14, 199–222 (2004). https://doi.org/10.1023/B:STCO.0000035301.49549.88

139. Scholkopf, B., Smola, A.J.: Learning with Kernels: Support Vector Machines, Regularization, Optimization, and Beyond. MIT Press (2018)

140. Brown, T.B., Mann, B., Ryder, N., Subbiah, M., Kaplan, J., Dhariwal, P., Neelakantan, A., Shyam, P., Sastry, G., Askell, A., Agarwal, S., Herbert-Voss, A., Krueger, G., Henighan, T., Child, R., Ramesh, A., Ziegler, D.M., Wu, J., Winter, C., Hesse, C., Chen, M., Sigler, E., Litwin, M., Gray, S., Chess, B., Clark, J., Berner, C., McCandlish, S., Radford, A., Sutskever, I., Amodei, D.: Language Models are Few-Shot Learners, (2020)

141. Rothman, D.: Artificial intelligence by example: develop machine intelligence from

scratch using real artificial intelligence use cases. Packt Publishing Ltd (2018)

# Appendix A – The coefficients of $\ln(\lambda) \sim \ln(p_0)$ models

This appendix presents the coefficients A and B, as well as the coefficient of determination $R^2$ of the fitted models shown in the Figure 26 in the subsection 4.5.2. The models are described using the following equation:

$$\ln(\lambda) = A * \ln(p_0) + B$$

**Table 9** The coefficients A, B and R2 for the fitted models presented in the Figure 26, in the subsection 4.5.2.

| $\phi$ | $\%CH_4$ | A | B | $R^2$ |
|---|---|---|---|---|
| 0.5 | 50 | -0.925 | 3.314 | 0.975 |
| 0.5 | 55 | -1.203 | 3.226 | 0.975 |
| 0.5 | 60 | -1.16 | 3.115 | 0.959 |
| 0.5 | 65 | -1.112 | 2.994 | 0.931 |
| 0.5 | 70 | -1.053 | 2.835 | 0.976 |
| 0.75 | 50 | -0.991 | 3.229 | 0.98 |
| 0.75 | 55 | -1.055 | 3.027 | 0.967 |
| 0.75 | 60 | -1.357 | 2.915 | 0.992 |
| 0.75 | 65 | -1.028 | 2.658 | 0.936 |
| 0.75 | 70 | -1.101 | 2.517 | 0.946 |
| 1.0 | 40 | -1.496 | 3.565 | 0.949 |
| 1.0 | 45 | -1.223 | 3.381 | 0.971 |
| 1.0 | 50 | -0.958 | 3.195 | 0.986 |
| 1.0 | 55 | -1.093 | 2.974 | 0.989 |
| 1.0 | 60 | -1.251 | 2.82 | 0.993 |
| 1.0 | 70 | -1.311 | 2.203 | 0.969 |
| 1.25 | 50 | -0.927 | 3.27 | 0.987 |
| 1.25 | 55 | -0.925 | 3.049 | 0.965 |
| 1.25 | 60 | -1.356 | 2.935 | 0.995 |
| 1.25 | 65 | -1.234 | 2.609 | 0.977 |
| 1.25 | 70 | -1.141 | 2.499 | 0.973 |
| 1.5 | 50 | -0.981 | 3.356 | 0.983 |
| 1.5 | 55 | -0.944 | 3.226 | 0.969 |
| 1.5 | 60 | -1.141 | 3.192 | 0.996 |
| 1.5 | 65 | -1.219 | 2.937 | 0.962 |
| 1.5 | 70 | -1.046 | 2.815 | 0.95 |

# Appendix B – The coefficients of $\lambda \sim \phi^2 + \phi$ models

This appendix presents the coefficients A, B and C, as well as the coefficient of determination $R^2$ of the fitted models shown in the Figure 27 in the subsection 4.5.3. The models are described using the following equation:

$$\lambda = A * \phi^2 + B * \phi + C$$

**Table 10** The coefficients A, B, C and $R^2$ for the fitted models presented in the Figure 27, in the subsection 4.5.3.

| $p_0$ | $\%CH_4$ | A | B | C | $R^2$ |
|---|---|---|---|---|---|
| 0.6 | 50 | 29.337 | -59.495 | 70.448 | 0.908 |
| 0.6 | 55 | 43.688 | -89.293 | 80.267 | 0.995 |
| 0.6 | 60 | 38.383 | -73.363 | 69.186 | 0.864 |
| 0.6 | 65 | 52.203 | -103.394 | 75.800 | 0.987 |
| 0.6 | 70 | 41.872 | -85.366 | 63.826 | 0.987 |
| 0.7 | 50 | 17.706 | -28.583 | 46.311 | 0.936 |
| 0.7 | 55 | 35.655 | -72.548 | 63.687 | 0.894 |
| 0.7 | 60 | 30.750 | -56.044 | 51.704 | 0.986 |
| 0.7 | 65 | 38.505 | -78.019 | 58.069 | 0.938 |
| 0.7 | 70 | 32.967 | -67.473 | 50.014 | 0.915 |
| 0.8 | 50 | 12.979 | -23.716 | 41.223 | 0.855 |
| 0.8 | 55 | 21.399 | -44.383 | 47.250 | 0.942 |
| 0.8 | 60 | 27.703 | -53.565 | 48.674 | 0.845 |
| 0.8 | 65 | 40.807 | -81.767 | 56.538 | 0.931 |
| 0.8 | 70 | 31.017 | -60.957 | 43.089 | 0.922 |
| 0.9 | 50 | 14.753 | -27.266 | 39.110 | 0.933 |
| 0.9 | 55 | 31.024 | -66.370 | 57.060 | 0.891 |
| 0.9 | 60 | 26.401 | -52.460 | 46.372 | 0.987 |
| 0.9 | 65 | 31.030 | -64.259 | 46.861 | 0.807 |
| 0.9 | 70 | 34.658 | -70.920 | 46.558 | 0.984 |
| 1.0 | 50 | 13.077 | -26.036 | 37.800 | 0.872 |
| 1.0 | 55 | 24.050 | -50.388 | 44.930 | 0.978 |
| 1.0 | 65 | 13.316 | -26.736 | 26.300 | 0.802 |
| 1.0 | 70 | 30.771 | -61.201 | 39.288 | 0.976 |
| 1.2 | 50 | 10.603 | -21.580 | 31.211 | 0.816 |
| 1.2 | 55 | 14.016 | -26.979 | 31.207 | 0.971 |
| 1.2 | 60 | 28.562 | -58.224 | 42.546 | 0.981 |
| 1.2 | 65 | 27.513 | -56.449 | 39.540 | 0.976 |
| 1.2 | 70 | 22.478 | -44.256 | 29.879 | 0.979 |
| 1.4 | 50 | 7.337 | -14.678 | 26.763 | 0.809 |
| 1.4 | 55 | 14.935 | -27.019 | 25.800 | 0.980 |
| 1.4 | 60 | 21.320 | -41.879 | 31.380 | 0.966 |
| 1.4 | 65 | 17.070 | -36.116 | 27.751 | 0.982 |
| 1.4 | 70 | 25.794 | -50.143 | 31.040 | 0.996 |

| | | | | | |
|---|---|---|---|---|---|
| 1.6 | 50 | 11.941 | -21.934 | 25.143 | 0.974 |
| 1.6 | 55 | 12.439 | -22.370 | 22.009 | 0.978 |
| 1.6 | 60 | 16.428 | -30.516 | 22.992 | 0.999 |
| 1.6 | 65 | 16.372 | -33.966 | 24.996 | 0.992 |
| 1.6 | 70 | 16.509 | -35.065 | 24.556 | 0.848 |

# Appendix C – The coefficients of $\lambda \sim \%CH_4$ models

This appendix presents the coefficients A and B as well as the coefficient of determination $R^2$ of the fitted models shown in the Figure 28 in the subsection 4.5.4. The models are described using the following equation:

$$\lambda = A * CH_4 + B$$

**Table 11** The coefficients A, B and $R^2$ for the fitted models presented in the Figure 28, in the subsection 4.5.4.

| ϕ | $p_0$ | A | B | $R^2$ |
|---|---|---|---|---|
| 0.5 | 0.6 | -0.823 | 90.34 | 0.958 |
| 0.5 | 0.7 | -0.638 | 69.558 | 0.909 |
| 0.5 | 0.8 | -0.571 | 61.921 | 0.926 |
| 0.5 | 0.9 | -0.565 | 60.221 | 0.811 |
| 0.5 | 1 | -0.675 | 62.373 | 0.9 |
| 0.5 | 1.2 | -0.469 | 47.48 | 0.903 |
| 0.5 | 1.4 | -0.411 | 40.561 | 0.885 |
| 0.5 | 1.6 | -0.287 | 30.326 | 0.835 |
| 0.75 | 0.6 | -1.026 | 95.474 | 0.951 |
| 0.75 | 0.7 | -0.813 | 75.129 | 0.899 |
| 0.75 | 0.8 | -0.776 | 69.256 | 0.881 |
| 0.75 | 0.9 | -0.727 | 63.22 | 0.906 |
| 0.75 | 1 | -0.701 | 60.33 | 0.99 |
| 0.75 | 1.2 | -0.541 | 47.653 | 0.962 |
| 0.75 | 1.4 | -0.52 | 43.885 | 0.904 |
| 0.75 | 1.6 | -0.358 | 32.46 | 0.857 |
| 1.0 | 0.6 | -1.203 | 103.037 | 0.936 |
| 1.0 | 0.7 | -0.988 | 84.009 | 0.991 |
| 1.0 | 0.8 | -1.189 | 92.946 | 0.977 |
| 1.0 | 0.9 | -0.941 | 76.017 | 0.96 |
| 1.0 | 1 | -0.799 | 63.997 | 0.984 |
| 1.0 | 1.2 | -0.714 | 57.036 | 0.988 |
| 1.0 | 1.4 | -0.599 | 47.897 | 0.985 |
| 1.0 | 1.6 | -0.38 | 32.128 | 0.948 |
| 1.25 | 0.6 | -0.962 | 91.718 | 0.85 |
| 1.25 | 0.7 | -0.991 | 85.897 | 0.878 |
| 1.25 | 0.8 | -0.671 | 63.599 | 0.936 |
| 1.25 | 0.9 | -0.813 | 68.892 | 0.954 |
| 1.25 | 1 | -0.752 | 62.822 | 0.962 |
| 1.25 | 1.2 | -0.609 | 51.755 | 0.966 |
| 1.25 | 1.4 | -0.603 | 49.257 | 0.909 |
| 1.25 | 1.6 | -0.499 | 41.071 | 0.967 |
| 1.5 | 0.6 | -0.822 | 90.24 | 0.844 |
| 1.5 | 0.7 | -0.961 | 91.057 | 0.917 |
| 1.5 | 0.8 | -0.646 | 66.954 | 0.875 |
| 1.5 | 0.9 | -0.661 | 64.345 | 0.92 |
| 1.5 | 1 | -0.584 | 56.569 | 0.896 |
| 1.5 | 1.2 | -0.443 | 45.636 | 0.941 |
| 1.5 | 1.4 | -0.418 | 41.542 | 0.855 |
| 1.5 | 1.6 | -0.509 | 44.478 | 0.995 |

# Appendix D – The coefficients of $\lambda \sim \Delta_i$ models

This appendix presents the coefficients A and B as well as the coefficient of determination $R^2$ of the fitted models shown in the Figure 29 in the subsection 4.5.5. The models are described using the following equation:

$$\lambda = A * \Delta_i + B$$

**Table 12** The coefficients A, B and $R^2$ for the fitted models presented in the Figure 29, in the subsection 4.5.5.

| ϕ | %$CH_4$ | A | B | $R^2$ |
|---|---|---|---|---|
| 0.5 | 50 | 6301.98 | 2.636 | 0.97 |
| 0.5 | 55 | 9215.84 | -2.94 | 0.971 |
| 0.5 | 60 | 9640.52 | -1.246 | 0.965 |
| 0.5 | 65 | 10501 | -1.829 | 0.949 |
| 0.5 | 70 | 10058.2 | -0.856 | 0.971 |
| 0.75 | 50 | 7163.91 | 1.182 | 0.984 |
| 0.75 | 55 | 8278.34 | -0.033 | 0.963 |
| 0.75 | 60 | 12303.7 | -4.87 | 0.987 |
| 0.75 | 65 | 9568.51 | -0.498 | 0.926 |
| 0.75 | 70 | 11054 | -1.505 | 0.961 |
| 1.0 | 40 | 5697.41 | -9.869 | 0.972 |
| 1.0 | 45 | 6378.41 | -3.153 | 0.982 |
| 1.0 | 50 | 5985.55 | 3.272 | 0.986 |
| 1.0 | 55 | 7984.69 | -0.537 | 0.989 |
| 1.0 | 60 | 10433.2 | -2.573 | 0.994 |
| 1.0 | 65 | 10694.3 | -1.986 | 0.977 |
| 1.0 | 70 | 10794.4 | -3.03 | 0.958 |
| 1.25 | 50 | 5381.35 | 3.433 | 0.989 |
| 1.25 | 55 | 6592.6 | 1.811 | 0.952 |
| 1.25 | 60 | 12344.4 | -6.437 | 0.986 |
| 1.25 | 65 | 10854.8 | -3.016 | 0.963 |
| 1.25 | 70 | 11751.1 | -1.609 | 0.965 |
| 1.5 | 50 | 4698.26 | 0.733 | 0.985 |
| 1.5 | 55 | 6213.85 | 0.869 | 0.968 |
| 1.5 | 60 | 10507.8 | -3.728 | 0.995 |
| 1.5 | 65 | 12560.5 | -4.973 | 0.956 |
| 1.5 | 70 | 12021.4 | -0.29 | 0.97 |

# Appendix E – The coefficients of ln(χ) ~ ln($p_0$) models

This appendix presents the coefficients A and B, as well as the coefficient of determination $R^2$ of the fitted models shown in the Figure 31 in the subsection 4.5.6. The models are described using the following equation:

$$\ln\left(\chi\right) = A \ast \ln\left(p_0\right) + B$$

**Table 13** The coefficients A, B and R2 for the fitted models presented in the Figure 26, in the subsection 4.5.6.

| ϕ | %CH4 | A | B | $R^2$ |
|---|---|---|---|---|
| 0.5 | 50 | -0.216 | 5.34 | 0.999 |
| 0.5 | 55 | -0.201 | 5.237 | 0.996 |
| 0.5 | 60 | -0.197 | 5.15 | 0.985 |
| 0.5 | 65 | -0.185 | 5.066 | 0.996 |
| 0.5 | 70 | -0.181 | 4.992 | 0.998 |
| 0.75 | 50 | -0.222 | 5.428 | 0.997 |
| 0.75 | 55 | -0.209 | 5.306 | 0.997 |
| 0.75 | 60 | -0.199 | 5.192 | 0.998 |
| 0.75 | 65 | -0.189 | 5.089 | 0.998 |
| 0.75 | 70 | -0.184 | 4.994 | 0.999 |
| 1.0 | 40 | -0.307 | 5.683 | 0.998 |
| 1.0 | 45 | -0.263 | 5.538 | 0.996 |
| 1.0 | 50 | -0.247 | 5.398 | 0.998 |
| 1.0 | 55 | -0.231 | 5.267 | 0.998 |
| 1.0 | 60 | -0.216 | 5.145 | 0.998 |
| 1.0 | 65 | -0.203 | 5.028 | 0.998 |
| 1.0 | 70 | -0.191 | 4.92 | 0.998 |
| 1.25 | 50 | -0.278 | 5.278 | 0.998 |
| 1.25 | 55 | -0.254 | 5.153 | 0.998 |
| 1.25 | 60 | -0.233 | 5.031 | 0.997 |
| 1.25 | 65 | -0.217 | 4.915 | 0.998 |
| 1.25 | 70 | -0.204 | 4.801 | 0.998 |
| 1.5 | 50 | -0.306 | 5.083 | 0.999 |
| 1.5 | 55 | -0.279 | 4.981 | 0.999 |
| 1.5 | 60 | -0.256 | 4.874 | 0.999 |
| 1.5 | 65 | -0.232 | 4.766 | 0.997 |
| 1.5 | 70 | -0.215 | 4.659 | 0.996 |

# Appendix F – Statistical description of the measurements

| %$CH_4$ | $\phi$ | $p_0$ | Count | Min | Max | Mean | Median | Std | Var | SEM | CV |
|---|---|---|---|---|---|---|---|---|---|---|---|
| 40 | 1 | 0.8 | 10 | 34.93 | 62.68 | 48.41 | 46.77 | 10.02 | 100.50 | 3.17 | 0.21 |
| 40 | 1 | 1 | 39 | 28.75 | 38.49 | 33.22 | 32.86 | 2.63 | 6.92 | 0.42 | 0.08 |
| 40 | 1 | 1.2 | 33 | 21.95 | 35.69 | 29.84 | 30.47 | 2.81 | 7.89 | 0.49 | 0.09 |
| 40 | 1 | 1.4 | 21 | 20.33 | 28.72 | 23.39 | 23.14 | 2.56 | 6.56 | 0.56 | 0.11 |
| 40 | 1 | 1.6 | 113 | 11.63 | 22.92 | 15.60 | 15.17 | 2.41 | 5.82 | 0.23 | 0.15 |
| 45 | 1 | 0.6 | 13 | 43.52 | 61.32 | 53.21 | 53.46 | 5.54 | 30.71 | 1.54 | 0.10 |
| 45 | 1 | 0.8 | 17 | 30.35 | 46.89 | 38.92 | 38.80 | 4.95 | 24.49 | 1.20 | 0.13 |
| 45 | 1 | 0.9 | 36 | 26.66 | 44.45 | 35.94 | 35.79 | 4.50 | 20.26 | 0.75 | 0.13 |
| 45 | 1 | 1 | 45 | 23.73 | 31.93 | 27.31 | 27.13 | 2.19 | 4.79 | 0.33 | 0.08 |
| 45 | 1 | 1.2 | 125 | 18.03 | 29.02 | 24.09 | 24.17 | 2.63 | 6.90 | 0.23 | 0.11 |
| 45 | 1 | 1.4 | 60 | 17.06 | 26.39 | 21.48 | 21.55 | 2.59 | 6.72 | 0.33 | 0.12 |
| 45 | 1 | 1.6 | 103 | 11.05 | 20.07 | 15.07 | 14.89 | 2.28 | 5.19 | 0.22 | 0.15 |
| 50 | 0.5 | 0.6 | 31 | 38.10 | 60.02 | 47.49 | 47.10 | 5.98 | 35.72 | 1.07 | 0.13 |
| 50 | 0.5 | 0.7 | 68 | 29.36 | 44.69 | 35.89 | 35.46 | 4.15 | 17.19 | 0.50 | 0.12 |
| 50 | 0.5 | 0.8 | 53 | 0.39 | 48.75 | 32.75 | 33.64 | 8.97 | 80.42 | 1.23 | 0.27 |
| 50 | 0.5 | 0.9 | 42 | 20.71 | 37.45 | 29.41 | 30.80 | 4.92 | 24.18 | 0.76 | 0.17 |
| 50 | 0.5 | 1 | 46 | 22.05 | 35.58 | 28.05 | 28.12 | 3.22 | 10.39 | 0.48 | 0.11 |
| 50 | 0.5 | 1.2 | 104 | 16.60 | 30.00 | 23.47 | 23.71 | 3.31 | 10.98 | 0.32 | 0.14 |
| 50 | 0.5 | 1.4 | 135 | 12.21 | 32.63 | 21.45 | 21.25 | 4.64 | 21.54 | 0.40 | 0.22 |
| 50 | 0.5 | 1.6 | 189 | 9.38 | 26.96 | 17.12 | 16.25 | 4.50 | 20.27 | 0.33 | 0.26 |
| 50 | 0.75 | 0.6 | 27 | 36.02 | 57.79 | 43.88 | 45.10 | 5.46 | 29.81 | 1.05 | 0.12 |
| 50 | 0.75 | 0.7 | 59 | 28.17 | 45.71 | 36.23 | 36.28 | 4.00 | 16.04 | 0.52 | 0.11 |
| 50 | 0.75 | 0.8 | 84 | 23.84 | 38.08 | 30.11 | 29.95 | 3.73 | 13.94 | 0.41 | 0.12 |
| 50 | 0.75 | 0.9 | 63 | 20.99 | 31.61 | 26.59 | 26.47 | 3.15 | 9.92 | 0.40 | 0.12 |
| 50 | 0.75 | 1 | 109 | 18.28 | 32.40 | 25.90 | 26.44 | 3.44 | 11.81 | 0.33 | 0.13 |
| 50 | 0.75 | 1.2 | 113 | 15.28 | 24.61 | 20.09 | 20.31 | 2.27 | 5.15 | 0.21 | 0.11 |
| 50 | 0.75 | 1.4 | 146 | 14.04 | 25.05 | 19.58 | 19.07 | 2.94 | 8.62 | 0.24 | 0.15 |
| 50 | 0.75 | 1.6 | 262 | 10.81 | 20.78 | 15.62 | 15.51 | 2.51 | 6.32 | 0.16 | 0.16 |
| 50 | 1 | 0.6 | 35 | 30.45 | 46.27 | 38.88 | 39.16 | 4.03 | 16.27 | 0.68 | 0.10 |
| 50 | 1 | 0.7 | 33 | 29.46 | 41.05 | 34.57 | 34.07 | 2.83 | 8.00 | 0.49 | 0.08 |
| 50 | 1 | 0.8 | 50 | 26.55 | 35.51 | 31.52 | 31.79 | 2.40 | 5.77 | 0.34 | 0.08 |
| 50 | 1 | 0.9 | 62 | 21.12 | 31.99 | 26.27 | 26.27 | 2.50 | 6.25 | 0.32 | 0.10 |
| 50 | 1 | 1 | 36 | 18.90 | 31.13 | 24.05 | 23.35 | 3.54 | 12.52 | 0.59 | 0.15 |
| 50 | 1 | 1.2 | 81 | 16.15 | 26.00 | 20.54 | 20.27 | 2.55 | 6.49 | 0.28 | 0.12 |
| 50 | 1 | 1.4 | 161 | 13.53 | 23.94 | 19.16 | 19.32 | 2.63 | 6.90 | 0.21 | 0.14 |
| 50 | 1 | 1.5 | 33 | 13.17 | 19.44 | 16.28 | 16.04 | 1.75 | 3.07 | 0.31 | 0.11 |
| 50 | 1 | 1.6 | 208 | 10.55 | 18.32 | 14.78 | 14.79 | 1.80 | 3.24 | 0.12 | 0.12 |
| 50 | 1.25 | 0.6 | 25 | 35.93 | 48.49 | 42.24 | 42.29 | 3.71 | 13.76 | 0.74 | 0.09 |
| 50 | 1.25 | 0.7 | 43 | 32.18 | 44.06 | 38.01 | 37.68 | 3.02 | 9.11 | 0.46 | 0.08 |
| 50 | 1.25 | 0.8 | 43 | 23.90 | 43.74 | 31.10 | 30.91 | 4.54 | 20.57 | 0.69 | 0.15 |

| | | | | | | | | | | | |
|---|---|---|---|---|---|---|---|---|---|---|---|
| 50 | 1.25 | 0.9 | 59 | 20.93 | 38.72 | 28.89 | 28.38 | 3.78 | 14.31 | 0.49 | 0.13 |
| 50 | 1.25 | 1 | 70 | 18.73 | 34.52 | 26.47 | 26.15 | 4.24 | 17.97 | 0.51 | 0.16 |
| 50 | 1.25 | 1.2 | 125 | 16.01 | 26.44 | 21.30 | 21.46 | 2.53 | 6.41 | 0.23 | 0.12 |
| 50 | 1.25 | 1.4 | 113 | 14.45 | 26.25 | 20.53 | 20.62 | 2.94 | 8.64 | 0.28 | 0.14 |
| 50 | 1.25 | 1.6 | 122 | 11.81 | 21.14 | 16.67 | 16.83 | 2.50 | 6.26 | 0.23 | 0.15 |
| 50 | 1.5 | 0.6 | 10 | 32.67 | 55.31 | 47.28 | 49.21 | 7.49 | 56.10 | 2.37 | 0.16 |
| 50 | 1.5 | 0.7 | 18 | 34.28 | 50.65 | 43.54 | 44.09 | 4.81 | 23.09 | 1.13 | 0.11 |
| 50 | 1.5 | 0.8 | 21 | 31.78 | 44.77 | 35.06 | 34.66 | 2.96 | 8.78 | 0.65 | 0.08 |
| 50 | 1.5 | 0.9 | 13 | 27.66 | 36.86 | 31.06 | 29.94 | 2.60 | 6.74 | 0.72 | 0.08 |
| 50 | 1.5 | 1 | 39 | 22.44 | 35.21 | 27.91 | 27.77 | 3.87 | 14.99 | 0.62 | 0.14 |
| 50 | 1.5 | 1.2 | 56 | 16.60 | 28.81 | 22.40 | 22.53 | 2.98 | 8.87 | 0.40 | 0.13 |
| 50 | 1.5 | 1.4 | 64 | 15.76 | 27.26 | 20.97 | 20.37 | 3.06 | 9.34 | 0.38 | 0.15 |
| 50 | 1.5 | 1.6 | 81 | 13.40 | 24.95 | 19.03 | 18.54 | 2.83 | 7.98 | 0.31 | 0.15 |
| 55 | 0.5 | 0.6 | 61 | 29.82 | 61.45 | 46.65 | 47.16 | 7.16 | 51.34 | 0.92 | 0.15 |
| 55 | 0.5 | 0.7 | 57 | 29.38 | 46.06 | 36.72 | 36.01 | 4.02 | 16.19 | 0.53 | 0.11 |
| 55 | 0.5 | 0.8 | 76 | 20.08 | 42.40 | 30.55 | 30.10 | 5.15 | 26.54 | 0.59 | 0.17 |
| 55 | 0.5 | 0.9 | 67 | 26.02 | 42.72 | 32.50 | 31.94 | 4.40 | 19.34 | 0.54 | 0.14 |
| 55 | 0.5 | 1 | 93 | 19.89 | 32.75 | 25.76 | 26.00 | 3.28 | 10.75 | 0.34 | 0.13 |
| 55 | 0.5 | 1.2 | 101 | 14.70 | 28.33 | 21.07 | 20.85 | 3.31 | 10.98 | 0.33 | 0.16 |
| 55 | 0.5 | 1.4 | 162 | 10.22 | 24.04 | 16.23 | 16.12 | 3.25 | 10.55 | 0.26 | 0.20 |
| 55 | 0.5 | 1.6 | 350 | 8.66 | 19.23 | 13.82 | 13.82 | 2.55 | 6.49 | 0.14 | 0.18 |
| 55 | 0.75 | 0.6 | 81 | 30.04 | 45.97 | 37.79 | 37.83 | 4.17 | 17.40 | 0.46 | 0.11 |
| 55 | 0.75 | 0.7 | 241 | 16.77 | 43.47 | 27.86 | 27.48 | 5.10 | 25.99 | 0.33 | 0.18 |
| 55 | 0.75 | 0.8 | 69 | 19.58 | 32.18 | 25.42 | 25.91 | 3.43 | 11.79 | 0.41 | 0.14 |
| 55 | 0.75 | 0.9 | 140 | 16.63 | 29.28 | 22.53 | 22.16 | 3.50 | 12.23 | 0.30 | 0.16 |
| 55 | 0.75 | 1 | 140 | 15.71 | 28.66 | 20.85 | 20.38 | 3.12 | 9.73 | 0.26 | 0.15 |
| 55 | 0.75 | 1.2 | 141 | 14.07 | 26.82 | 19.16 | 18.80 | 3.22 | 10.39 | 0.27 | 0.17 |
| 55 | 0.75 | 1.4 | 325 | 9.00 | 18.65 | 13.49 | 13.32 | 2.43 | 5.89 | 0.13 | 0.18 |
| 55 | 0.75 | 1.6 | 312 | 8.56 | 17.10 | 12.58 | 12.55 | 2.12 | 4.50 | 0.12 | 0.17 |
| 55 | 1 | 0.6 | 135 | 22.21 | 53.34 | 34.28 | 33.87 | 6.22 | 38.67 | 0.54 | 0.18 |
| 55 | 1 | 0.7 | 109 | 20.53 | 37.05 | 28.86 | 29.67 | 4.33 | 18.72 | 0.41 | 0.15 |
| 55 | 1 | 0.8 | 99 | 17.56 | 38.99 | 25.18 | 24.40 | 4.89 | 23.87 | 0.49 | 0.19 |
| 55 | 1 | 0.9 | 127 | 15.23 | 33.64 | 23.11 | 22.96 | 4.46 | 19.93 | 0.40 | 0.19 |
| 55 | 1 | 1 | 457 | 11.04 | 29.10 | 18.01 | 17.51 | 4.20 | 17.64 | 0.20 | 0.23 |
| 55 | 1 | 1.4 | 323 | 8.23 | 20.85 | 13.84 | 13.96 | 3.27 | 10.69 | 0.18 | 0.24 |
| 55 | 1 | 1.6 | 376 | 6.47 | 18.07 | 11.72 | 11.33 | 2.89 | 8.34 | 0.15 | 0.25 |
| 55 | 1.25 | 0.6 | 63 | 33.38 | 42.45 | 37.51 | 37.39 | 1.92 | 3.69 | 0.24 | 0.05 |
| 55 | 1.25 | 0.7 | 83 | 21.37 | 32.40 | 27.42 | 27.67 | 2.58 | 6.65 | 0.28 | 0.09 |
| 55 | 1.25 | 0.8 | 77 | 19.86 | 28.76 | 24.57 | 24.38 | 2.12 | 4.51 | 0.24 | 0.09 |
| 55 | 1.25 | 0.9 | 62 | 20.01 | 26.42 | 22.92 | 22.84 | 1.43 | 2.05 | 0.18 | 0.06 |
| 55 | 1.25 | 1 | 88 | 13.81 | 24.95 | 20.12 | 20.13 | 2.86 | 8.17 | 0.30 | 0.14 |
| 55 | 1.25 | 1.2 | 186 | 12.20 | 28.16 | 19.08 | 18.80 | 3.66 | 13.42 | 0.27 | 0.19 |
| 55 | 1.25 | 1.4 | 296 | 9.32 | 21.29 | 15.65 | 15.68 | 2.86 | 8.20 | 0.17 | 0.18 |

| | | | | | | | | | | | |
|---|---|---|---|---|---|---|---|---|---|---|---|
| 55 | 1.25 | 1.6 | 209 | 8.28 | 20.05 | 13.61 | 13.54 | 2.55 | 6.51 | 0.18 | 0.19 |
| 55 | 1.5 | 0.6 | 69 | 27.59 | 65.76 | 44.39 | 43.53 | 8.60 | 74.01 | 1.04 | 0.19 |
| 55 | 1.5 | 0.7 | 50 | 26.24 | 68.10 | 35.39 | 34.55 | 6.62 | 43.81 | 0.94 | 0.19 |
| 55 | 1.5 | 0.8 | 60 | 23.28 | 36.77 | 28.99 | 28.55 | 2.88 | 8.29 | 0.37 | 0.10 |
| 55 | 1.5 | 0.9 | 85 | 22.54 | 31.41 | 26.90 | 26.75 | 2.37 | 5.64 | 0.26 | 0.09 |
| 55 | 1.5 | 1 | 64 | 18.49 | 27.52 | 23.26 | 23.19 | 2.41 | 5.81 | 0.30 | 0.10 |
| 55 | 1.5 | 1.2 | 122 | 17.69 | 27.21 | 22.42 | 22.27 | 2.51 | 6.32 | 0.23 | 0.11 |
| 55 | 1.5 | 1.4 | 134 | 14.28 | 22.85 | 18.71 | 18.89 | 2.36 | 5.59 | 0.20 | 0.13 |
| 55 | 1.5 | 1.6 | 205 | 10.18 | 22.22 | 16.44 | 16.85 | 3.02 | 9.10 | 0.21 | 0.18 |
| 60 | 0.5 | 0.6 | 95 | 28.67 | 56.15 | 41.89 | 41.56 | 6.97 | 48.64 | 0.72 | 0.17 |
| 60 | 0.5 | 0.7 | 152 | 19.02 | 46.23 | 31.14 | 30.84 | 5.68 | 32.25 | 0.46 | 0.18 |
| 60 | 0.5 | 0.8 | 73 | 19.08 | 36.12 | 27.94 | 27.46 | 3.40 | 11.53 | 0.40 | 0.12 |
| 60 | 0.5 | 0.9 | 89 | 18.51 | 38.50 | 26.52 | 26.16 | 5.64 | 31.83 | 0.60 | 0.21 |
| 60 | 0.5 | 1 | 66 | 17.03 | 29.54 | 23.69 | 23.42 | 3.48 | 12.11 | 0.43 | 0.15 |
| 60 | 0.5 | 1.2 | 113 | 13.41 | 29.70 | 20.84 | 20.31 | 3.97 | 15.75 | 0.37 | 0.19 |
| 60 | 0.5 | 1.4 | 283 | 9.28 | 23.52 | 15.70 | 15.40 | 3.31 | 10.93 | 0.20 | 0.21 |
| 60 | 0.5 | 1.6 | 471 | 7.10 | 17.50 | 11.79 | 11.72 | 2.65 | 7.01 | 0.12 | 0.22 |
| 60 | 0.75 | 0.6 | 72 | 26.84 | 48.88 | 37.05 | 37.34 | 4.98 | 24.76 | 0.59 | 0.13 |
| 60 | 0.75 | 0.7 | 165 | 20.29 | 36.09 | 27.65 | 27.48 | 3.99 | 15.89 | 0.31 | 0.14 |
| 60 | 0.75 | 0.8 | 78 | 14.40 | 41.40 | 26.32 | 24.97 | 6.63 | 43.96 | 0.75 | 0.25 |
| 60 | 0.75 | 0.9 | 26 | 18.69 | 31.71 | 22.32 | 21.63 | 3.09 | 9.54 | 0.61 | 0.14 |
| 60 | 0.75 | 1.2 | 226 | 10.54 | 18.56 | 14.23 | 14.01 | 1.99 | 3.95 | 0.13 | 0.14 |
| 60 | 0.75 | 1.4 | 243 | 8.67 | 16.10 | 11.91 | 11.62 | 1.73 | 3.00 | 0.11 | 0.15 |
| 60 | 0.75 | 1.6 | 699 | 6.00 | 13.43 | 9.46 | 9.44 | 1.80 | 3.25 | 0.07 | 0.19 |
| 60 | 1 | 0.6 | 36 | 25.65 | 38.03 | 31.59 | 31.35 | 2.93 | 8.57 | 0.49 | 0.09 |
| 60 | 1 | 0.7 | 99 | 18.34 | 34.38 | 25.76 | 25.36 | 4.20 | 17.65 | 0.42 | 0.16 |
| 60 | 1 | 0.8 | 86 | 16.28 | 26.92 | 21.36 | 21.47 | 2.68 | 7.16 | 0.29 | 0.13 |
| 60 | 1 | 0.9 | 124 | 12.66 | 28.10 | 20.32 | 20.77 | 4.00 | 16.03 | 0.36 | 0.20 |
| 60 | 1 | 1 | 207 | 10.88 | 27.39 | 17.01 | 16.31 | 3.52 | 12.41 | 0.24 | 0.21 |
| 60 | 1 | 1.2 | 335 | 8.73 | 18.65 | 13.43 | 13.15 | 2.50 | 6.25 | 0.14 | 0.19 |
| 60 | 1 | 1.4 | 303 | 8.40 | 15.43 | 11.38 | 11.10 | 1.64 | 2.69 | 0.09 | 0.14 |
| 60 | 1 | 1.6 | 355 | 6.03 | 12.98 | 8.85 | 8.72 | 1.66 | 2.74 | 0.09 | 0.19 |
| 60 | 1.25 | 0.6 | 78 | 26.61 | 55.80 | 39.66 | 40.18 | 6.36 | 40.43 | 0.72 | 0.16 |
| 60 | 1.25 | 0.7 | 71 | 23.32 | 36.21 | 29.88 | 29.46 | 3.50 | 12.24 | 0.42 | 0.12 |
| 60 | 1.25 | 0.8 | 116 | 17.86 | 33.41 | 24.71 | 24.57 | 3.55 | 12.58 | 0.33 | 0.14 |
| 60 | 1.25 | 0.9 | 129 | 15.77 | 31.02 | 21.59 | 21.31 | 3.51 | 12.31 | 0.31 | 0.16 |
| 60 | 1.25 | 1.2 | 324 | 8.03 | 20.63 | 14.37 | 14.08 | 2.68 | 7.19 | 0.15 | 0.19 |
| 60 | 1.25 | 1.4 | 332 | 8.34 | 15.94 | 11.65 | 11.52 | 1.87 | 3.49 | 0.10 | 0.16 |
| 60 | 1.25 | 1.6 | 258 | 7.61 | 13.53 | 10.47 | 10.47 | 1.56 | 2.43 | 0.10 | 0.15 |
| 60 | 1.5 | 0.6 | 32 | 37.97 | 54.43 | 44.84 | 44.56 | 4.54 | 20.65 | 0.80 | 0.10 |
| 60 | 1.5 | 0.7 | 36 | 27.52 | 46.30 | 36.84 | 36.43 | 4.38 | 19.22 | 0.73 | 0.12 |
| 60 | 1.5 | 0.8 | 28 | 23.60 | 38.88 | 31.05 | 30.61 | 3.91 | 15.27 | 0.74 | 0.13 |
| 60 | 1.5 | 0.9 | 70 | 17.77 | 36.99 | 27.31 | 27.02 | 4.72 | 22.32 | 0.56 | 0.17 |

| | | | | | | | | | | | |
|---|---|---|---|---|---|---|---|---|---|---|---|
| 60 | 1.5 | 1 | 67 | 16.19 | 33.70 | 23.29 | 22.94 | 4.27 | 18.24 | 0.52 | 0.18 |
| 60 | 1.5 | 1.2 | 146 | 11.75 | 25.88 | 19.39 | 19.89 | 3.24 | 10.47 | 0.27 | 0.17 |
| 60 | 1.5 | 1.4 | 191 | 11.69 | 22.01 | 16.79 | 16.64 | 2.46 | 6.07 | 0.18 | 0.15 |
| 60 | 1.5 | 1.5 | 170 | 11.73 | 21.33 | 15.89 | 15.38 | 2.40 | 5.75 | 0.18 | 0.15 |
| 60 | 1.5 | 1.6 | 192 | 10.11 | 18.46 | 14.21 | 14.15 | 2.09 | 4.36 | 0.15 | 0.15 |
| 65 | 0.5 | 0.6 | 87 | 23.72 | 50.39 | 37.13 | 37.74 | 7.24 | 52.44 | 0.78 | 0.20 |
| 65 | 0.5 | 0.7 | 145 | 15.44 | 43.33 | 28.97 | 29.79 | 7.41 | 54.87 | 0.62 | 0.26 |
| 65 | 0.5 | 0.8 | 203 | 16.06 | 36.37 | 26.70 | 26.41 | 5.02 | 25.22 | 0.35 | 0.19 |
| 65 | 0.5 | 0.9 | 171 | 13.82 | 32.20 | 23.34 | 23.39 | 4.21 | 17.69 | 0.32 | 0.18 |
| 65 | 0.5 | 1 | 314 | 9.94 | 24.00 | 15.74 | 15.19 | 3.39 | 11.52 | 0.19 | 0.22 |
| 65 | 0.5 | 1.2 | 252 | 11.35 | 25.16 | 18.03 | 18.01 | 3.60 | 12.93 | 0.23 | 0.20 |
| 65 | 0.5 | 1.4 | 449 | 9.38 | 19.76 | 13.82 | 13.60 | 2.50 | 6.25 | 0.12 | 0.18 |
| 65 | 0.5 | 1.6 | 429 | 8.18 | 16.61 | 12.11 | 12.00 | 2.04 | 4.15 | 0.10 | 0.17 |
| 65 | 0.75 | 0.6 | 173 | 17.12 | 37.29 | 27.36 | 27.11 | 4.80 | 23.00 | 0.36 | 0.18 |
| 65 | 0.75 | 0.7 | 184 | 13.43 | 30.47 | 20.10 | 19.94 | 3.66 | 13.38 | 0.27 | 0.18 |
| 65 | 0.75 | 0.8 | 212 | 9.97 | 23.24 | 16.41 | 16.19 | 3.36 | 11.29 | 0.23 | 0.20 |
| 65 | 0.75 | 0.9 | 338 | 8.95 | 18.69 | 13.63 | 13.50 | 2.46 | 6.07 | 0.13 | 0.18 |
| 65 | 0.75 | 1 | 280 | 9.82 | 20.68 | 14.87 | 14.65 | 2.66 | 7.07 | 0.16 | 0.18 |
| 65 | 0.75 | 1.2 | 328 | 9.27 | 16.94 | 12.86 | 12.82 | 1.82 | 3.31 | 0.10 | 0.14 |
| 65 | 0.75 | 1.4 | 459 | 6.71 | 14.57 | 10.49 | 10.44 | 1.89 | 3.56 | 0.09 | 0.18 |
| 65 | 0.75 | 1.6 | 579 | 5.83 | 12.14 | 8.64 | 8.53 | 1.55 | 2.41 | 0.06 | 0.18 |
| 65 | 1 | 0.6 | 188 | 15.66 | 37.05 | 25.55 | 24.70 | 5.20 | 27.07 | 0.38 | 0.20 |
| 65 | 1 | 0.7 | 250 | 11.34 | 29.64 | 20.22 | 20.37 | 4.03 | 16.25 | 0.25 | 0.20 |
| 65 | 1 | 0.8 | 231 | 9.21 | 23.15 | 15.76 | 15.47 | 3.37 | 11.38 | 0.22 | 0.21 |
| 65 | 1 | 0.9 | 226 | 10.90 | 24.60 | 16.04 | 15.31 | 3.34 | 11.16 | 0.22 | 0.21 |
| 65 | 1 | 1 | 330 | 8.58 | 17.43 | 12.60 | 12.54 | 2.17 | 4.71 | 0.12 | 0.17 |
| 65 | 1 | 1.2 | 341 | 7.11 | 16.04 | 11.08 | 11.02 | 2.12 | 4.51 | 0.12 | 0.19 |
| 65 | 1 | 1.4 | 782 | 5.95 | 12.84 | 8.87 | 8.71 | 1.58 | 2.49 | 0.06 | 0.18 |
| 65 | 1 | 1.6 | 1001 | 5.01 | 11.42 | 7.64 | 7.50 | 1.49 | 2.23 | 0.05 | 0.20 |
| 65 | 1.25 | 0.6 | 141 | 14.69 | 42.28 | 27.13 | 26.92 | 6.00 | 36.05 | 0.51 | 0.22 |
| 65 | 1.25 | 0.7 | 139 | 10.98 | 29.44 | 19.61 | 19.92 | 4.20 | 17.67 | 0.36 | 0.21 |
| 65 | 1.25 | 0.8 | 112 | 14.54 | 28.80 | 19.60 | 18.91 | 3.28 | 10.77 | 0.31 | 0.17 |
| 65 | 1.25 | 0.9 | 198 | 8.57 | 20.76 | 14.30 | 14.06 | 2.88 | 8.29 | 0.20 | 0.20 |
| 65 | 1.25 | 1 | 220 | 9.20 | 17.55 | 12.93 | 12.95 | 2.21 | 4.88 | 0.15 | 0.17 |
| 65 | 1.25 | 1.2 | 383 | 7.34 | 16.32 | 11.15 | 10.90 | 2.13 | 4.52 | 0.11 | 0.19 |
| 65 | 1.25 | 1.4 | 500 | 5.68 | 13.44 | 8.83 | 8.82 | 1.77 | 3.12 | 0.08 | 0.20 |
| 65 | 1.25 | 1.6 | 321 | 5.29 | 11.02 | 7.90 | 7.89 | 1.43 | 2.04 | 0.08 | 0.18 |
| 65 | 1.5 | 0.6 | 92 | 18.15 | 64.64 | 38.51 | 38.77 | 10.26 | 105.32 | 1.07 | 0.27 |
| 65 | 1.5 | 0.7 | 82 | 18.58 | 42.12 | 27.95 | 27.64 | 5.42 | 29.42 | 0.60 | 0.19 |
| 65 | 1.5 | 0.8 | 28 | 16.25 | 31.96 | 24.92 | 25.56 | 4.43 | 19.63 | 0.84 | 0.18 |
| 65 | 1.5 | 0.9 | 137 | 12.95 | 29.37 | 20.25 | 20.00 | 4.07 | 16.54 | 0.35 | 0.20 |
| 65 | 1.5 | 1 | 131 | 8.46 | 24.99 | 16.58 | 16.27 | 4.14 | 17.16 | 0.36 | 0.25 |
| 65 | 1.5 | 1.2 | 216 | 11.11 | 22.94 | 17.10 | 17.07 | 3.09 | 9.52 | 0.21 | 0.18 |

| | | | | | | | | | | | |
|---|---|---|---|---|---|---|---|---|---|---|---|
| 65 | 1.5 | 1.4 | 347 | 7.88 | 17.59 | 12.18 | 12.15 | 2.60 | 6.76 | 0.14 | 0.21 |
| 65 | 1.5 | 1.6 | 492 | 7.11 | 15.12 | 10.96 | 10.89 | 1.99 | 3.97 | 0.09 | 0.18 |
| 70 | 0.5 | 0.6 | 49 | 24.99 | 38.36 | 31.68 | 31.69 | 3.54 | 12.51 | 0.51 | 0.11 |
| 70 | 0.5 | 0.7 | 64 | 15.40 | 37.36 | 23.83 | 24.07 | 5.15 | 26.53 | 0.64 | 0.22 |
| 70 | 0.5 | 0.8 | 91 | 13.38 | 26.52 | 20.40 | 20.41 | 3.48 | 12.12 | 0.36 | 0.17 |
| 70 | 0.5 | 0.9 | 167 | 12.73 | 27.85 | 19.87 | 19.90 | 4.12 | 16.95 | 0.32 | 0.21 |
| 70 | 0.5 | 1 | 70 | 11.87 | 20.02 | 16.19 | 16.29 | 2.21 | 4.91 | 0.26 | 0.14 |
| 70 | 0.5 | 1.2 | 183 | 7.90 | 19.50 | 13.27 | 13.22 | 2.99 | 8.96 | 0.22 | 0.23 |
| 70 | 0.5 | 1.4 | 209 | 8.44 | 17.26 | 12.39 | 12.31 | 2.19 | 4.80 | 0.15 | 0.18 |
| 70 | 0.5 | 1.6 | 469 | 6.76 | 16.01 | 10.80 | 10.72 | 2.24 | 5.01 | 0.10 | 0.21 |
| 70 | 0.75 | 0.6 | 85 | 14.18 | 31.74 | 23.44 | 23.03 | 4.25 | 18.08 | 0.46 | 0.18 |
| 70 | 0.75 | 0.7 | 132 | 12.72 | 26.36 | 19.78 | 19.64 | 3.42 | 11.69 | 0.30 | 0.17 |
| 70 | 0.75 | 0.8 | 204 | 9.90 | 22.71 | 15.21 | 14.83 | 3.26 | 10.62 | 0.23 | 0.21 |
| 70 | 0.75 | 0.9 | 190 | 7.98 | 18.41 | 12.86 | 12.55 | 2.95 | 8.71 | 0.21 | 0.23 |
| 70 | 0.75 | 1 | 279 | 7.39 | 17.49 | 11.35 | 10.97 | 2.52 | 6.35 | 0.15 | 0.22 |
| 70 | 0.75 | 1.2 | 350 | 6.02 | 14.53 | 9.72 | 9.57 | 1.84 | 3.40 | 0.10 | 0.19 |
| 70 | 0.75 | 1.4 | 529 | 5.45 | 11.21 | 8.09 | 8.07 | 1.44 | 2.06 | 0.06 | 0.18 |
| 70 | 0.75 | 1.6 | 409 | 5.97 | 12.18 | 8.65 | 8.51 | 1.58 | 2.49 | 0.08 | 0.18 |
| 70 | 1 | 0.6 | 47 | 15.65 | 23.81 | 19.64 | 19.62 | 1.98 | 3.93 | 0.29 | 0.10 |
| 70 | 1 | 0.7 | 68 | 10.77 | 19.53 | 14.18 | 14.25 | 1.95 | 3.79 | 0.24 | 0.14 |
| 70 | 1 | 0.8 | 242 | 7.67 | 19.87 | 11.75 | 11.56 | 2.29 | 5.26 | 0.15 | 0.20 |
| 70 | 1 | 0.9 | 134 | 6.70 | 13.72 | 9.69 | 9.72 | 1.72 | 2.96 | 0.15 | 0.18 |
| 70 | 1 | 1 | 117 | 5.63 | 10.79 | 8.07 | 8.04 | 1.29 | 1.66 | 0.12 | 0.16 |
| 70 | 1 | 1.2 | 327 | 5.19 | 10.47 | 7.55 | 7.57 | 1.31 | 1.72 | 0.07 | 0.17 |
| 70 | 1 | 1.4 | 47 | 4.82 | 8.15 | 6.42 | 6.33 | 0.89 | 0.79 | 0.13 | 0.14 |
| 70 | 1 | 1.6 | 312 | 3.14 | 8.47 | 4.77 | 4.54 | 1.06 | 1.13 | 0.06 | 0.22 |
| 70 | 1.25 | 0.5 | 39 | 18.61 | 38.57 | 27.92 | 27.54 | 5.29 | 27.98 | 0.85 | 0.19 |
| 70 | 1.25 | 0.6 | 89 | 13.17 | 33.41 | 23.38 | 23.13 | 4.95 | 24.53 | 0.53 | 0.21 |
| 70 | 1.25 | 0.7 | 170 | 11.73 | 22.96 | 17.12 | 16.99 | 2.68 | 7.16 | 0.21 | 0.16 |
| 70 | 1.25 | 0.8 | 119 | 11.43 | 21.87 | 16.82 | 17.07 | 2.45 | 6.00 | 0.22 | 0.15 |
| 70 | 1.25 | 0.9 | 89 | 8.81 | 19.31 | 12.87 | 12.44 | 2.53 | 6.39 | 0.27 | 0.20 |
| 70 | 1.25 | 1 | 160 | 7.35 | 17.10 | 11.26 | 11.19 | 2.22 | 4.91 | 0.18 | 0.20 |
| 70 | 1.25 | 1.2 | 445 | 6.30 | 14.35 | 10.03 | 9.94 | 2.02 | 4.07 | 0.10 | 0.20 |
| 70 | 1.25 | 1.4 | 321 | 6.12 | 12.08 | 8.87 | 8.77 | 1.43 | 2.03 | 0.08 | 0.16 |
| 70 | 1.25 | 1.6 | 369 | 4.63 | 10.20 | 7.05 | 6.89 | 1.40 | 1.95 | 0.07 | 0.20 |
| 70 | 1.5 | 0.6 | 19 | 25.17 | 33.80 | 29.69 | 29.71 | 2.31 | 5.31 | 0.53 | 0.08 |
| 70 | 1.5 | 0.7 | 37 | 16.86 | 31.16 | 23.23 | 22.66 | 3.68 | 13.57 | 0.61 | 0.16 |
| 70 | 1.5 | 0.8 | 54 | 12.87 | 28.08 | 20.94 | 21.25 | 4.60 | 21.19 | 0.63 | 0.22 |
| 70 | 1.5 | 0.9 | 138 | 9.14 | 25.81 | 17.85 | 18.18 | 3.66 | 13.40 | 0.31 | 0.21 |
| 70 | 1.5 | 1 | 132 | 10.62 | 22.45 | 16.65 | 16.73 | 2.54 | 6.45 | 0.22 | 0.15 |
| 70 | 1.5 | 1.2 | 289 | 9.43 | 20.08 | 13.99 | 13.63 | 2.62 | 6.85 | 0.15 | 0.19 |
| 70 | 1.5 | 1.4 | 91 | 7.47 | 20.61 | 13.80 | 14.06 | 2.74 | 7.50 | 0.29 | 0.20 |
| 70 | 1.5 | 1.6 | 234 | 5.36 | 13.88 | 9.04 | 9.10 | 1.95 | 3.82 | 0.13 | 0.22 |